博士論文

Search for the Standard Model Higgs Boson using the OPAL Detector at LEP2

『**OPAL** 検出器を用いた **LEP2** における
標準模型 **Higgs** 粒子の探索』

平成十年一月十三日

神戸大学自然科学研究科

中村 勇

Abstract

A search for the Standard Model Higgs boson has been performed for the data collected in 1996 by the OPAL detector at center-of-mass energies of 161.3, 170.3 and 172.3 GeV. The data used in the alalysis corespond to 10.0 pb^{-1} at 161.3 GeV, 1.0 pb^{-1} at 170.3 GeV and 9.4 pb^{-1} at 172.3 GeV. The search is sensitive to the main final states in which the Higgs boson is produced in association with a fermion anti-fermion pair; namely four jets, two jets with missing energy, and two jets with a pair of electron, muon, or tau leptons. Two candidate events have been observed, one at 161.3 GeV and the other at 172.3 GeV, consistent with the Standard Model background expectations. Combined with earlier searches at center-of-mass energies in the vicinity of the Z^0 resonance, a lower limit for the mass of the Standard Model Higgs boson was obtained to be 69.4 GeV at 95% confidence level.

謝辞

まず最初に六年間の長きにわたり指導を賜り、私をOPAL実験に送り出して下さった武田 廣先生と留学先のCERNでの私の引受人になって下さり、数々の助言、叱咤激励を頂いた東京大学素粒子物理国際研究センターの駒宮 幸男先生に感謝します。

素粒子センターの山下 了先生には何と言って感謝の気持ちを表せばいいのかわかりません。加速器実験に参加した経験の無かった私に一から解析の仕方をご指導下さり、解析が行き詰まったときにはいつも適切な助言を与えて下さいました。本当にありがとうございました。

数々の有意義な議論をたたかわせた川本 辰夫先生、真下 哲郎先生をはじめとするOPAL東京グループの皆さん、神戸大学の野崎 光昭先生、川越 清以先生、そして高エネルギー研究室の皆さんに感謝します。

Higgs粒子の発見を目指して共に研究をすすめたOPAL Higgs Working Groupの皆さん、素晴らしいOPAL検出器を作り、現在に至るまで検出器を保守、整備し、qualityの高いdataを供給してくれたOPAL collaborationのmember、加速器を安定に運用しbeamを供給してくれたCERN SL Divisionの皆さんありがとうございました。

最後に、本研究には直接関わることはありませんでしたが、私の数々のわがままをきいて、ここまで生活を支えてくださった両親と私の精神的支えになってくれた友人達に感謝したいと思います。

中村 勇

Contents

Chapter 1

Introduction

1.1 The Electroweak Standard Model

The so-called 'Standard Model' of the electroweak theory [1] is a quantum field theory based on the gauge group SU(2)×U(1). The SU(2) part represents the weak isospin symmetry, and the U(1) part is for the weak hyper-charge. The symmetry is spontaneously broken by the Higgs mechanism [2], which gives masses to weak gauge bosons.

The model includes three generations of spin-1/2 fermions and corresponding anti-fermions as sources of the electroweak force:

- neutral leptons (neutrinos): $\nu_{\mathrm{e}}(\overline{\nu}_{\mathrm{e}})$, $\nu_\mu(\overline{\nu}_\mu)$, $\nu_\tau(\overline{\nu}_\tau)$;
- charged leptons: $\mathrm{e}^-(\mathrm{e}^+)$, $\mu^-(\mu^+)$, $\tau^-(\tau^+)$;
- charge +2/3 quarks: $\mathrm{u}(\overline{\mathrm{u}})$, $\mathrm{c}(\overline{\mathrm{c}})$, $\mathrm{t}(\overline{\mathrm{t}})$;
- charge -1/3 quarks: $\mathrm{d}(\overline{\mathrm{d}})$, $\mathrm{s}(\overline{\mathrm{s}})$, $\mathrm{b}(\overline{\mathrm{b}})$.

They are listed above in the ascending order of their masses, whereas the neutrinos are assumed to be massless. The heaviest quark t has been recently discovered [3]. The Standard Model does not restrict the number of generations to be three; it has been experimentally confirmed for the case of light neutrinos.

The boson fields mediating the interactions can be derived by the local gauge invariance of the Lagrangian. Requiring the Lagrangian density to be invariant under local SU(2) transformations in the isospin space, the minimum interaction Lagrangian including an isospin triplet of gauge fields, $W_\mu^{1,2,3}$, is obtained. Similarly, requirement of the local U(1) invariance results in a gauge field B_μ. The four gauge fields represents massless vector bosons, which does not directly correspond to physically observed electroweak bosons. The physically observed gauge bosons correspond to linear combinations of the SU(2) and U(1) gauge bosons:

$$W_\mu^+ = \frac{1}{\sqrt{2}}(W_\mu^1 - iW_\mu^2), \tag{1.1}$$

$$W_\mu^- = \frac{1}{\sqrt{2}}(W_\mu^1 + iW_\mu^2), \tag{1.2}$$

$$Z_\mu = \cos\theta_{\mathrm{W}} W_\mu^3 - \sin\theta_{\mathrm{W}} B_\mu, \tag{1.3}$$

$$A_\mu = \sin\theta_{\mathrm{W}} W_\mu^3 + \cos\theta_{\mathrm{W}} B_\mu, \tag{1.4}$$

where θ_{W} is an adjustable parameter called the Weinberg angle or weak mixing angle.

The couplings of the fermions to the gauge fields are obtained from the gauge invariance and the known electromagnetic and weak couplings at low energies. The experimental fact that the charged current interaction takes place in left-handed forms must also be taken into account. This fact is included into the model by hand: the Standard Model doesn't explain why the charged current has a V−A form. Left-handed fermions are written as the isospin doublets

$$\begin{pmatrix} \nu_{\mathrm{eL}} \\ \mathrm{e_L} \end{pmatrix} \begin{pmatrix} \nu_{\mu\mathrm{L}} \\ \mu_{\mathrm{L}} \end{pmatrix} \begin{pmatrix} \nu_{\tau\mathrm{L}} \\ \tau_{\mathrm{L}} \end{pmatrix} \\ \begin{pmatrix} \mathrm{u_L} \\ \mathrm{d_L} \end{pmatrix} \begin{pmatrix} \mathrm{c_L} \\ \mathrm{s_L} \end{pmatrix} \begin{pmatrix} \mathrm{t_L} \\ \mathrm{b_L} \end{pmatrix}, \tag{1.5}$$

while right-handed fermions stay SU(2) singlets

$$\begin{array}{llllll} \mathrm{e_R} & \mu_{\mathrm{R}} & \tau_{\mathrm{R}} & & & \\ \mathrm{u_R} & \mathrm{c_R} & \mathrm{t_R} & \mathrm{d_R} & \mathrm{s_R} & \mathrm{b_R}. \end{array} \tag{1.6}$$

The left-handed and right-handed fields for a fermion f are defined by

$$f_{\mathrm{L}} = \frac{1}{2}(1+\gamma_5)f, \tag{1.7}$$

$$f_{\mathrm{R}} = \frac{1}{2}(1-\gamma_5)f. \tag{1.8}$$

There are no right-handed neutrinos in the minimal Standard Model.

The Lagrangian describing the interactions between fermions and gauge bosons has three terms. The first, the charged current term is

$$\mathcal{L}_{\mathrm{cc}} = \frac{g}{2\sqrt{2}}(J^{\mu}_{\mathrm{cc}} W^{-}_{\mu} + h.c.), \tag{1.9}$$

where the charged current J^{μ}_{cc} is given by

$$J^{\mu}_{\mathrm{cc}} = \begin{pmatrix} \overline{\nu}_{\mathrm{eL}} & \overline{\mathrm{e}}_{\mathrm{L}} \end{pmatrix} \gamma^{\mu} \begin{pmatrix} \nu_{\mathrm{eL}} \\ \mathrm{e_L} \end{pmatrix} \tag{1.10}$$

for electrons and other leptons, and by

$$J^{\mu}_{\mathrm{cc}} = \begin{pmatrix} \overline{\mathrm{u}}_{\mathrm{L}} & \overline{\mathrm{c}}_{\mathrm{L}} & \overline{\mathrm{t}}_{\mathrm{L}} \end{pmatrix} \gamma^{\mu} U \begin{pmatrix} \mathrm{d_L} \\ \mathrm{s_L} \\ \mathrm{b_L} \end{pmatrix}, \tag{1.11}$$

for quarks. The unitary matrix U describes the mixing of the weak couplings of quarks, and is often called as the Cabibbo-Kobayashi-Maskawa matrix. Comparing the coupling constant in equation (1.9) with the Fermi-type four point vertex Lagrangian for muon decays, a relationship

$$\frac{g^2}{8m^2_{\mathrm{W}}} = \frac{G_{\mathrm{F}}}{\sqrt{2}}, \tag{1.12}$$

is obtained, where G_{F} is the Fermi constant,

$$G_{\mathrm{F}} = 1.16637(2) \times 10^{-5}\,\mathrm{GeV}^{-2}. \tag{1.13}$$

Fermion	q	g_V	g_A
ν	0	$\frac{1}{2}$	$\frac{1}{2}$
e, μ, τ	-1	$-\frac{1}{2}+2\sin^2\theta_W$	$-\frac{1}{2}$
u, c, t	$\frac{2}{3}$	$\frac{1}{2}-\frac{4}{3}\sin^2\theta_W$	$\frac{1}{2}$
d, s, b	$-\frac{1}{3}$	$-\frac{1}{2}+\frac{2}{3}\sin^2\theta_W$	$-\frac{1}{2}$

Table 1.1: Electroweak coupling constants of fermions

The second, the electromagnetic term is

$$\mathcal{L}_{\text{em}} = g\sin\theta_W(J^\mu_{\text{em}}A_\mu + h.c.), \tag{1.14}$$

where the electromagnetic current J^μ_{em} is given by

$$J^\mu_{\text{em}} = q_f\bar{f}\gamma^\mu f \tag{1.15}$$

for any fermion f with charge q_f. Comparing equation (1.14) with the usual electromagnetic interaction Lagrangian, the relation

$$e = g\sin\theta_W = g'\cos\theta_W \tag{1.16}$$

is obtained. It follows from equations (1.12) and (1.16) that the mass of W$^\pm$ is given by

$$\begin{aligned} m_W &= \sqrt{\frac{\pi\alpha}{\sqrt{2}G_F\sin^2\theta_W}} \quad (1.17)\\ &= \frac{37.280\,\text{GeV}}{\sin\theta_W}. \quad (1.18)\end{aligned}$$

The Z^0 mass is related to m_W as

$$m_Z = \frac{m_W}{\cos\theta_W}. \tag{1.19}$$

The third, the neutral current term is

$$\mathcal{L}_{\text{nc}} = \frac{e}{\sin\theta_W\cos\theta_W}(J^\mu_{\text{nc}}Z_\mu + h.c.), \tag{1.20}$$

where the neutral current J^μ_{nc} is given by

$$J^\mu_{\text{nc}} = g^f_V\bar{f}\gamma^\mu f + g^f_A\bar{f}\gamma^\mu\gamma_5 f \tag{1.21}$$

for any fermion f. The vector and the axial-vector coupling constants g^f_V and g^f_A are given by

$$\begin{aligned} g^f_V &= I_3 - 2q_f\sin^2\theta_W, \quad (1.22)\\ g^f_A &= I_3, \quad (1.23)\end{aligned}$$

where I_3 is the third component of the weak isospin. The coupling constants q_f, g^f_V and g^f_A are summarized in Table 1.1.

1.2 The Higgs Mechanism

The Higgs mechanism gives masses to three of the four gauge bosons. A complex SU(2) doublet scalar field is introduced as

$$\phi = \begin{pmatrix} \phi^+ \\ \phi^0 \end{pmatrix} = \frac{1}{\sqrt{2}} \begin{pmatrix} \phi_1 + i\phi_2 \\ \phi_3 + i\phi_4 \end{pmatrix}, \tag{1.24}$$

with the Higgs potential, V,

$$V(\phi^\dagger\phi) = \mu^2\phi^\dagger\phi + \lambda(\phi^\dagger\phi)^2. \tag{1.25}$$

The Lagrangian is expressed as,

$$\mathcal{L} = (D_\mu\phi)^\dagger(D^\mu\phi) - \left\{\mu^2\phi^\dagger\phi + \lambda(\phi^\dagger\phi)^2\right\}. \tag{1.26}$$

The covariant derivative operation on an isodoublet field is

$$D_\mu = \partial_\mu - ig\frac{\vec{\tau}}{2}\cdot\vec{W}_\mu - ig'\frac{Y}{2}B_\mu\,. \tag{1.27}$$

In the case $\mu^2 < 0$, the ground state, called vacuum, is obtained at

$$\phi^\dagger\phi = \frac{-\mu^2}{2\lambda} = \frac{v^2}{2}, \tag{1.28}$$

where $v/\sqrt{2}$ is the vacuum expectation value. The scalar doublet ϕ can be redefined around the vacuum,

$$\phi_0 = \frac{1}{\sqrt{2}}\begin{pmatrix} 0 \\ v \end{pmatrix} \tag{1.29}$$

using the real fields $\xi_1(x)$, $\xi_2(x)$, $\xi_3(x)$ and $H(x)$ as

$$\phi(x) = \frac{1}{\sqrt{2}}e^{\vec{\xi(x)}\cdot\vec{\tau}/2}\begin{pmatrix} 0 \\ v + H(x) \end{pmatrix}. \tag{1.30}$$

Here the $\xi_1(x), \xi_2(x), \xi_3(x)$ and $H(x)$ have zero vacuum expectation values. The choice of the vacuum "spontaneously breaks" the SU(2) symmetry. Since the Lagrangian is invariant under the local gauge transformation

$$\phi(x) \to \phi'(x) = e^{\vec{\xi(x)}\cdot\vec{\tau}/2}\phi(x), \tag{1.31}$$

the phase factor can be suppressed. In this "unitary gauge". the ξ degrees of freedom seem to vanish but essentially reappear as the longitudinal components of $W^\pm$ and Z when they acquire masses. Hence the field can be expressed as,

$$\phi(x) = \frac{1}{\sqrt{2}}\begin{pmatrix} 0 \\ v + H(x) \end{pmatrix}. \tag{1.32}$$

The masses of the gauge bosons and the couplings are obtained by substituting ϕ in equation (1.26).

$$\mathcal{L} = (\partial H)^2 + \frac{1}{4}W_\mu^+W^{-\mu}(v+H)^2 + \frac{1}{8}(g^2 + g'^2)Z_\mu Z^\mu(v+H)^2 - V(\phi^\dagger\phi). \tag{1.33}$$

The v^2 terms provide W and Z^0 boson mass term

$$m_{\mathrm{W}}^2 W_\mu^+W^{-\mu} + \frac{1}{2}m_{\mathrm{Z}^0}^2 Z_\mu Z^\mu \tag{1.34}$$

with

$$m_{\mathrm{W}} = \frac{1}{2} v g, \qquad m_{\mathrm{Z}^0} = \frac{1}{2} v \sqrt{g^2 + g'^2} = \frac{m_{\mathrm{W}}}{\cos\theta_{\mathrm{W}}}, \tag{1.35}$$

while the photon remains massless. The equations (1.16) and (1.35) lead to the relation

$$v = \frac{2m_{\mathrm{W}}}{g} = (\sqrt{2} G_{\mathrm{F}})^{\frac{1}{2}} \sim 246\ \mathrm{GeV}. \tag{1.36}$$

The terms $HW_\mu^+ W^{-\mu}$ and $HZ_\mu Z^\mu$ give the couplings of the gauge bosons $\mathrm{W}^\pm$ and Z^0 to the Higgs boson,

$$g m_{\mathrm{W}} \quad \text{and} \quad \frac{g m_{\mathrm{Z}^0}}{2\cos\theta_{\mathrm{W}}}, \tag{1.37}$$

respectively.

The potential term of the equation (1.33) is

$$\mu^2 H^2 - \mu^2 \left(\frac{H^3}{v} + \frac{H^4}{4v^2} \right) + \text{constant}. \tag{1.38}$$

The first term gives the Higgs boson mass,

$$m_{\mathrm{H}^0} = \sqrt{-2\mu^2},$$

and the second term is the Higgs self couplings. Since μ is a free parameter, the Higgs boson mass cannot be constrained in the Standard model. It should be experimentally determined.

The fermion masses and the Yukawa couplings of ϕ to the leptons are given by the Lagrangian

$$\mathcal{L} = g_{\mathrm{e}} \left[\bar{\ell}_{\mathrm{L}} \phi \mathrm{e}_{\mathrm{R}} + \phi^\dagger \bar{\mathrm{e}}_{\mathrm{R}} \ell_{\mathrm{L}} \right], \tag{1.39}$$

where g_{e} is an arbitrary coupling constant and

$$\ell_{\mathrm{L}} = \begin{pmatrix} \nu_{\mathrm{e}} \\ \mathrm{e} \end{pmatrix}_{\mathrm{L}}.$$

Substituging ϕ in the same way as the previous case, the Lagrangian becomes

$$\mathcal{L} = \frac{g_{\mathrm{e}}}{\sqrt{2}} v (\bar{\mathrm{e}}_{\mathrm{L}} \mathrm{e}_{\mathrm{R}} + \bar{\mathrm{e}}_{\mathrm{R}} \mathrm{e}_{\mathrm{L}}) + \frac{g_{\mathrm{e}}}{\sqrt{2}} (\bar{\mathrm{e}}_{\mathrm{L}} \mathrm{e}_{\mathrm{R}} + \bar{\mathrm{e}}_{\mathrm{R}} \mathrm{e}_{\mathrm{L}}) H. \tag{1.40}$$

As the first term has the form expected for a fermion mass, the electron mass can be written as,

$$m_{\mathrm{e}} = \frac{g_{\mathrm{e}} v}{\sqrt{2}}. \tag{1.41}$$

The Higgs boson coupling to the electron is

$$\frac{g_{\mathrm{e}}}{\sqrt{2}} = \frac{m_{\mathrm{e}}}{v} = 2^{\frac{1}{4}} \sqrt{G_{\mathrm{F}}} m_{\mathrm{e}} = \frac{g m_{\mathrm{e}}}{2 m_{\mathrm{W}}}. \tag{1.42}$$

The same treatment can be applied to the second and third generation leptons. Quark masses are also generated by Yukawa coupling to the Higgs boson,

$$\mathcal{L} = g_{\mathrm{d}} \overline{D}_{\mathrm{L}} \phi \mathrm{d}_{\mathrm{R}} + g_{\mathrm{u}} \overline{D}_{\mathrm{L}} \phi_c \mathrm{u}_{\mathrm{R}} + h.c. \tag{1.43}$$

where g_d and g_u are the couplings to the up and down type quarks and

$$D_\mathrm{L} = \begin{pmatrix} \mathrm{u} \\ \mathrm{d} \end{pmatrix}_\mathrm{L}, \qquad \phi_c = -i\tau_2\phi^* = \begin{pmatrix} -\phi^{0*} \\ \phi^- \end{pmatrix}.$$

Substituting ϕ and ϕ_c,

$$\phi \to \frac{1}{\sqrt{2}}\begin{pmatrix} 0 \\ v + H \end{pmatrix}, \qquad \phi_c \to \frac{1}{\sqrt{2}}\begin{pmatrix} -(v + H) \\ 0 \end{pmatrix}$$

the Lagrangian becomes

$$\mathcal{L} = m_\mathrm{d}\bar{\mathrm{d}}\mathrm{d} + m_\mathrm{u}\bar{\mathrm{u}}\mathrm{u} + \frac{m_\mathrm{d}}{v}\bar{\mathrm{d}}\mathrm{d}H + \frac{m_\mathrm{u}}{v}\bar{\mathrm{u}}\mathrm{u}H. \tag{1.44}$$

1.3 Mass bounds of the Higgs Boson

In the framework of the Standard Model the mass of the Higgs boson cannot be predicted. However some mass bounds are given from (1) the strong interaction limit and the vacuum stability and (2) the precise electroweak measurements.

Since the quartic Higgs self coupling in equation (1.38) grows indefinitely with rising the mass of Higgs boson, an upper bound on m_{H^0} follows from the requirement that the theory is valid up to a cut-off scale Λ [4]. On the other hand the requirement of vacuum stability in the Standard Model imposes a lower bound on the Higgs boson mass, which depends crucially on the top quark mass and on the cut-off scale Λ [4, 5]. Figure 1.1 (A) shows these bounds on the Higgs boson mass for different cut-off scale Λ at which new physics is expected.

The mass bound is obtained also from the precision electroweak measurements at LEP, SLC, and elsewhere through the loop correction by the Higgs boson to the electroweak observables. Although the sensitivity to the Higgs boson mass is only logarithmic, the accuracy of the measurements makes it possible to derive a χ^2 curve as a function of the Higgs mass. Figure 1.1 (B) shows the result of global fit of measured observables to the Standard Model calculation reported in reference [6] including the direct measurement of the top quark mass at the TeVatron [7].

On the other hand, experimental searches for the Standard Model Higgs bosons have been extensively performed at various experiments. The highest mass limit is given by experiments at LEP1 [8]. In the energy region of LEP1, the Higgs boson is produced with a higgsstrahlung process associated with a virtual Z^0. The limit by four LEP experiments is about 60 GeV. The limit obtained by each LEP experiment is listed in Table 1.2. Figure 1.2 shows the mass limit obtaind by the OPAL experiment at LEP1 energy region.

Experiment	Lower Mass Limit
ALEPH	63.9 GeV
DELPHI	55.7 GeV
L3	60.2 GeV
OPAL	59.6 GeV

Table 1.2: *Lower mass limits obtaind by four LEP experiments at LEP1 energy.*

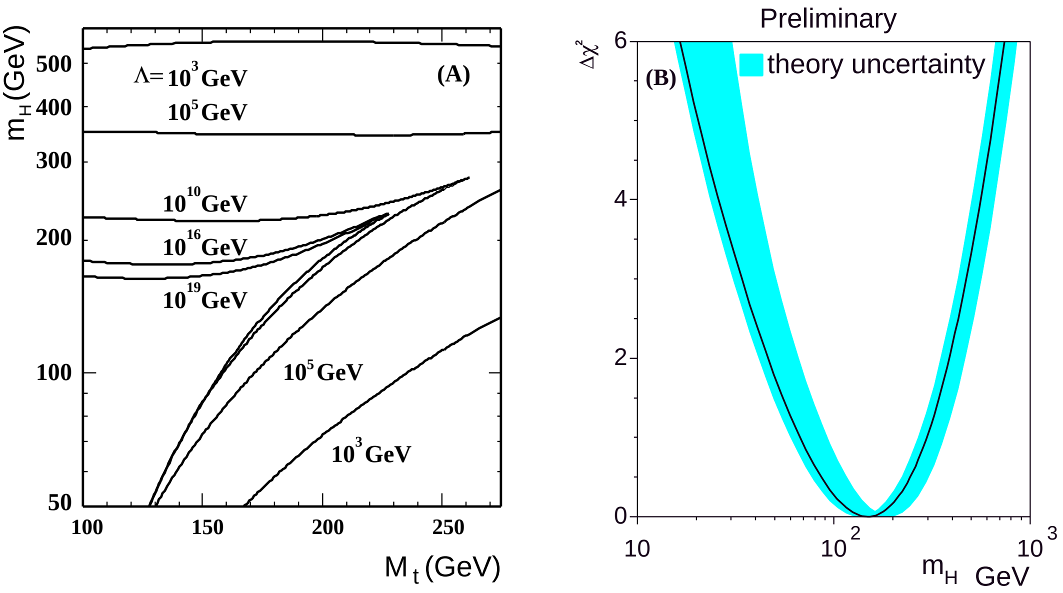

Figure 1.1: *(A): Strong interaction and vacuum stability bounds on the Higgs boson mass for different cut-off energy scale, Λ, as functions of the top quark and the Higgs boson masses. (B):* $\Delta\chi^2 = \chi^2 - \chi_{\mathrm{min}}$ *as a function of Higgs boson mass. The curve is the result of the fit using the date from the electroweak measurements [6]. The band represents an estimate of the theoretical error due to missing higher order corrections.*

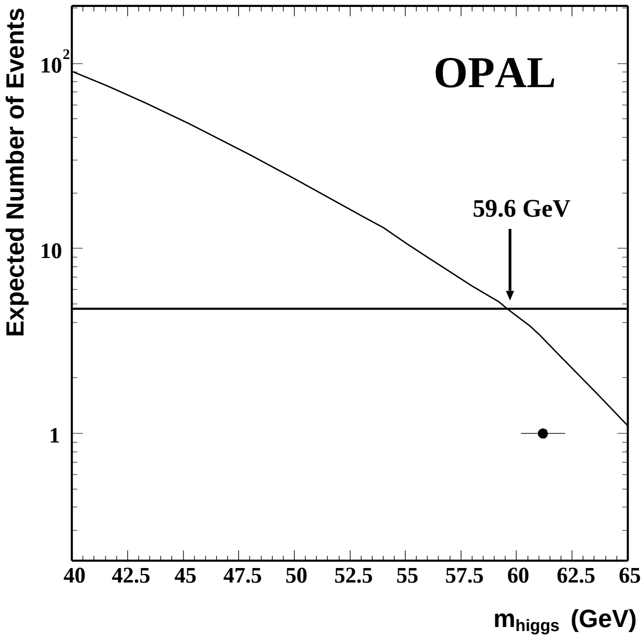

Figure 1.2: *The experimental mass limit obtaind by the OPAL experiment at LEP1 energy region. Point with error bar shows the reconstructed Higgs boson mass of the candidate event.*

1.4 Production of the Higgs Boson

At LEP2 energies the Higgs boson is produced by two processes; namely the higgsstrahlung process and the fusion process. Diagrams of those processes are shown in Figure 1.3. The cross-section of the fusion process is very small compared to that of the higgsstrahlung process at LEP2 energies, but becomes competitive under the kinematical condition where Z^0 turns virtual in the higgsstrahlung process.

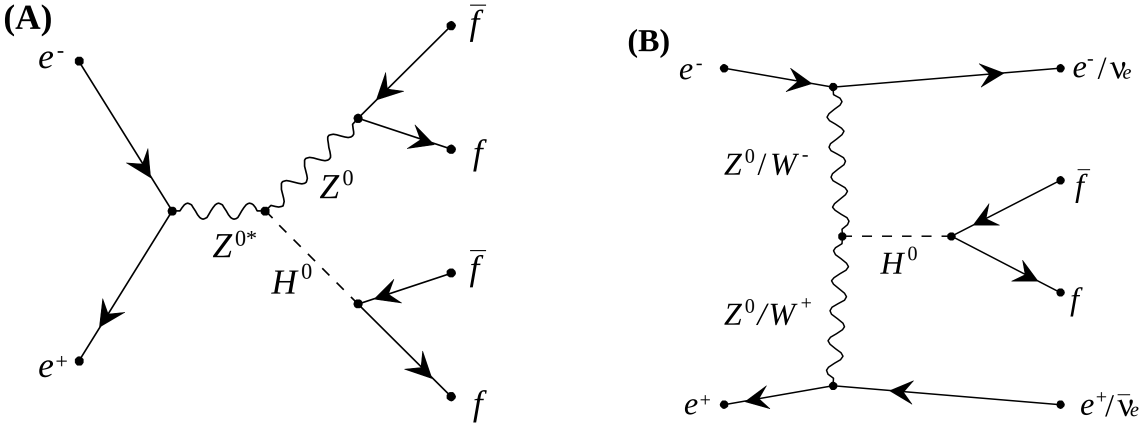

Figure 1.3: *Diagrams of the (A) higgsstrahlung, (B)* $\mathrm{W}^+\mathrm{W}^-$ *and* $\mathrm{Z}^0\mathrm{Z}^0$ *fusion processes.*

Higgsstrahlung process The production cross-section of the higgsstrahlung process is given as [9],

$$\sigma(\mathrm{e}^+\mathrm{e}^- \to \mathrm{H}^0\mathrm{Z}^0) = \frac{G_\mathrm{F}^2 m_{\mathrm{Z}^0}^4}{96\pi s}(v_\mathrm{e}^2 + a_\mathrm{e}^2)\lambda^{\frac{1}{2}} \frac{\lambda + 12 m_{\mathrm{Z}^0}^2/s}{(1 - m_{\mathrm{Z}^0}^2 s)^2} \tag{1.45}$$

where $a_\mathrm{e} = -1$, $v_\mathrm{e} = -1+4\sin^2\theta_\mathrm{W}$. $\lambda = (1 - \frac{m_{\mathrm{H}^0}^2}{s} - \frac{m_{\mathrm{Z}^0}^2}{s})^2 - \frac{4m_{\mathrm{H}^0}^2 m_{\mathrm{Z}^0}^2}{s^2}$ is the phase space function. The correction from photon radiation is taken into account by convoluting equation (1.45) with the radiator function $G(x)$,

$$\langle\sigma\rangle = \int_{x_{\mathrm{H}^0}}^1 dx G(x)\sigma(xs) \tag{1.46}$$

with $x_{\mathrm{H}^0} = m_{\mathrm{H}^0}/s$. The radiator function is given in references [10, 11].

Fusion process The production cross-sections of the fusion process are written as [9],

$$\sigma(\mathrm{e}^+\mathrm{e}^- \to \mathrm{H}^0\mathrm{VV}) = \frac{G_\mathrm{F}^3 m_\mathrm{V}^4}{64\sqrt{2}\pi}\int_{x_{\mathrm{H}^0}}^1 dx \int_x^1 \frac{dy}{[1+(y-x)/x_\mathrm{V}]^2}[(v_\mathrm{e}^2 + a_\mathrm{e}^2)^2 f(x,y) + 4v_\mathrm{e}^2 a_\mathrm{e}^2 g(x,y)] \tag{1.47}$$

$$\begin{aligned} f(x,y) &= \left(\frac{2x}{y^3} - \frac{1+2x}{y^2} + \frac{2+x}{2y} - \frac{1}{2}\right)\left[\frac{z}{1+z} - \log(1+z)\right] + \frac{x}{y^3}\frac{z^2(1-y)}{1+z} \\ g(x,y) &= \left(-\frac{x}{y^2} - \frac{2+x}{2y} - \frac{1}{2}\right)\left[\frac{z}{1+z} - \log(1+z)\right] \end{aligned}$$

where V is either the W or Z^0 boson, $x_{\mathrm{H}^0} = m_{\mathrm{H}^0}^2/s$, $x_{\mathrm{V}} = m_{\mathrm{V}}^2/s$, $z = y(x - x_{\mathrm{H}^0})/x_{\mathrm{V}}x)$ and v_{e}, a_{e} the couplings to the gauge bosons, $v_{\mathrm{e}} = 1 - \sin^2\theta_{\mathrm{W}}, a_{\mathrm{e}} = -1$ for the Z^0 and $v_{\mathrm{e}} = a_{\mathrm{e}} = \sqrt{2}$ for the the W boson. The combined production cross-sections are shown in Figure 1.4 (A) as a function of the Higgs boson mass.

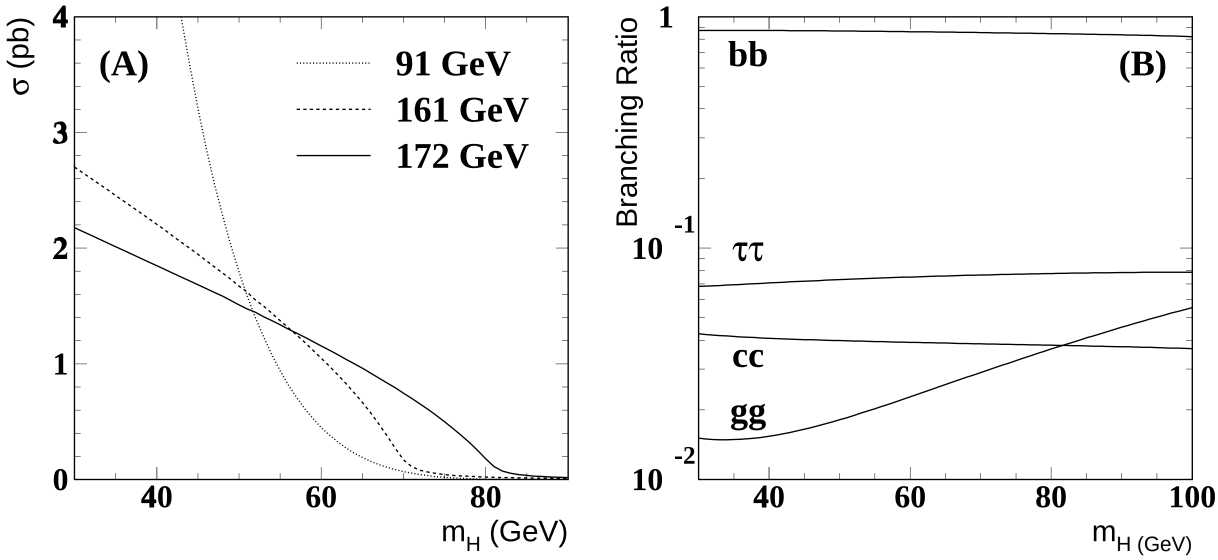

Figure 1.4: *(A) Combined production cross-sections as a function of the Higgs boson mass. The contributions from the fusion processes and the initial state radiation are included. Solid, dashed and dotted lines show cross-sections separately for center-of-mass energies of 172, 161 and 91 GeV, respectively. (B) Branching fraction of the Higgs boson as a function of the Higgs boson mass.*

1.5 Decay of the Higgs Boson

The main decay modes of the Higgs Boson relevant in the LEP2 are,

Quark Decay	:	H^0→b$\bar{\mathrm{b}}$ and c$\bar{\mathrm{c}}$,
Lepton Decay	:	H^0→$\tau^+\tau^-$, and
Gluon Decay	:	H^0→ gg.

The main decay mode is b$\bar{\mathrm{b}}$, followed by $\tau^+\tau^-$, c$\bar{\mathrm{c}}$ and gg at a level of less than 10 %.

Higgs decay into fermions The partial decay width of the Higgs boson into a lepton pair [12] is given by

$$\Gamma(\mathrm{H}^0 \to \ell^+\ell^-) = \frac{G_{\mathrm{F}} m_\ell^2}{4\sqrt{2}\pi} m_{\mathrm{H}^0}\beta^3. \tag{1.48}$$

where $\beta = (1 - 4m_\ell^2/m_{\mathrm{H}^0}^2)^{1/2}$ is the velocity of the leptons in the rest flame of the Higgs boson.

For the decay widths into quark pairs, QCD corrections [13] must be included. The corrections in the limit $m_H \gg m_q$ are known up to order α_s^2. The partial decay width can be written as,

$$\Gamma(\mathrm{H^0} \to \mathrm{q\bar{q}}) = \frac{3G_\mathrm{F}}{4\sqrt{2}\pi} m_\mathrm{q}^2 m_{\mathrm{H^0}} \left[1 + 5.67 \left(\frac{\alpha_\mathrm{s}}{\pi} \right) + (35.94 - 1.36 N_\mathrm{F}) \left(\frac{\alpha_\mathrm{s}}{\pi} \right)^2 \right]. \tag{1.49}$$

where $\alpha_s \equiv \alpha_s(m_H^2)$ and $N_F = 5$ is the number of active quark flavors.

Higgs decay into gluons In the Standard Model, the Higgs decays into gluons via top quark loops [14]. Since this decay mode is of significance only for the Higgs masses far below the top threshold, the gluonic width can be written in the approximate form [15]

$$\Gamma(\mathrm{H^0} \to \mathrm{gg}) = \frac{G_\mathrm{F} \alpha_\mathrm{s}^2(m_{\mathrm{H^0}}^2)}{36\sqrt{2}\pi^3} m_{\mathrm{H^0}}^3 \left[1 + \left(\frac{95}{4} - \frac{7}{6} N_\mathrm{F} \right) \frac{\alpha_\mathrm{s}^2(m_{\mathrm{H^0}}^2)}{\pi} \right]. \tag{1.50}$$

The branching fractions of the Higgs boson are shown in Figure 1.4 (B) as functions of the Higgs boson mass.

Since the Higgs boson is dominantly produced with the $\mathrm{Z^0}$ boson, the final state consists of four fermions. The final state of the Higgs boson production can be categorized by the decay mode of $\mathrm{Z^0}$ and Higgs boson; namely

- the four jets channel in which $\mathrm{Z^0 \to q\bar{q}}$ and $\mathrm{H^0 \to b\bar{b}}$,
- the missing energy channel in which $\mathrm{Z^0} \to \nu\bar{\nu}$,
- the tau channels in which $\mathrm{Z^0 \to q\bar{q}}$ and $\mathrm{H^0} \to \tau^+\tau^-$ or $\mathrm{Z^0} \to \tau^+\tau^-$, and
- the electron and muon channels in which $\mathrm{Z^0} \to \ell^+\ell^-$.

The branching fractions of the higgsstrahlung process falling into these final state are listed in Table 1.3. The fusion processes have the same final state topologies as the missing energy channel and the electron channel.

channel	final state	Br	$\mathrm{Z^0}\to$xx		$\mathrm{H^0}\to$xx	
Four jets	$\mathrm{q\bar{q}b\bar{b}}$	60 %	$\mathrm{q\bar{q}}$	70 %	$\mathrm{b\bar{b}}$	86 %
Missing Energy	$\nu\bar{\nu}\mathrm{H^0}$	20 %	$\nu\bar{\nu}$	20 %	all	100 %
Tau	$\mathrm{q\bar{q}}\tau^+\tau^-$	5.6 %	$\mathrm{q\bar{q}}$	70 %	$\tau^+\tau^-$	8 %
	$\tau^+\tau^-\mathrm{H^0}$	3.4 %	$\tau^+\tau^-$	3.4 %	all	100 %
Electron and Muon	$\mathrm{e^+e^-H^0}$	3.4 %	$\mathrm{e^+e^-}$	3.4 %	all	100 %
	$\mu^+\mu^-\mathrm{H^0}$	3.4 %	$\mu^+\mu^-$	3.4 %	all	100 %

Table 1.3: *List of final state topologies for* $m_{\mathrm{H^0}}$ *=65 GeV.*

Chapter 2

Experimental Apparatus

2.1 LEP Storage Ring

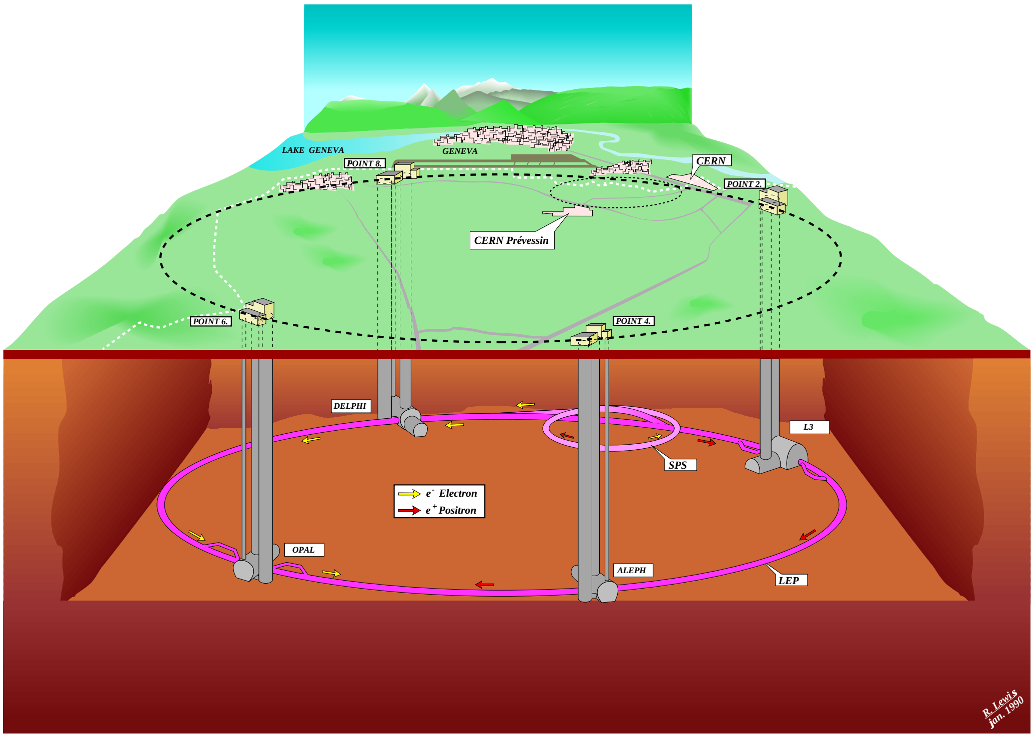

Figure 2.1: *Schematic view of LEP accelerator location.*

The CERN Large Electron-Positron collider, also known as LEP, is a storage ring designed to investigate e^+e^- collision at center-of-mass energies up to 200 GeV. Electrons and positrons are stored in a ring-shaped vacuum chamber as several counter-rotating ‘bunches’, and collide at ‘interaction points’ where experiments observe the events. A schematic view of LEP accelerator location is shown in Figure 2.1.

2.1.1 Beam Energy

The design of the LEP electron-positron collider was motivated by a very clear physics target: direct investigation of the Standard Model of the electroweak interaction at the energy scale of its symmetry breaking. The collider is operated, in its first phase (LEP1), at the energy of the $e^+e^- \to Z^0$ resonance, producing a large number of Z^0's. In the second phase (LEP2), the energy is raised above the threshold of the $e^+e^- \to W^+W^-$ process. These processes require the energy per beam being $\sim$50 GeV at phase one and $\geq$90 GeV at phase two.

The maximum energy reached by an electron storage ring is limited by the energy loss due to the synchrotron radiation. For an electron of energy E_b running in a circle of radius ρ, the radiation energy loss per turn is given by

$$U_0 = c_\gamma \frac{E_b^4}{\rho}, \tag{2.1}$$

where

$$c_\gamma = \frac{4\pi}{3} \frac{r_e}{(m_e c^2)^3} \tag{2.2}$$

with r_e being the classical electron radius and m_e the mass of the electron. To maintain beams in the orbit, this energy loss must be compensated by the radio-frequency (RF) acceleration system. The radius of LEP was decided to be $\sim$3.5 km by the optimization between the available RF power and the building cost of the ring.

2.1.2 Luminosity

The second important parameter of a colliding-type accelerator is the luminosity $\mathcal{L}$. For a physical process of cross-section σ, the event rate is given by

$$\frac{dN}{dt} = \sigma \mathcal{L}. \tag{2.3}$$

In the case of a head-on collider like LEP, the luminosity is given by

$$\mathcal{L} = \frac{N_e N_p k_b f_{rev}}{4\pi \sigma_x^* \sigma_y^*}, \tag{2.4}$$

where N_e and N_p are the numbers of electrons and positrons per bunch respectively, k_b is the number of bunches per beam, f_{rev} is the frequency of revolution, and $\sigma_x^* \sigma_y^*$ is the cross-section of the bunches at the interaction point. It is obvious from equation (2.4) that better luminosity is attained by:

- increasing N_e and N_p, i.e., increasing the current per bunch,
- increasing the number of bunches k_b, and
- decreasing $\sigma_x^* \sigma_y^*$, i.e., focusing the beam to a smaller spot at the interaction point.

The design luminosity of LEP2 with four bunches and 3 mA per beam is $1.6 \times 10^{31}\,\mathrm{cm}^{-2}\mathrm{s}^{-1}$ for each interaction point. At the Z^0 resonance, each experiment should detect Z^0 decays at a rate of 0.55 Hz with the ratio of hadronic and non-hadronic decays of about 7:1.

2.1.3 Structure and Components

The LEP storage ring consists of eight straight sections connected by the same number of curved sections. The circumference is 26.67 km. The ring is situated underground, in a tunnel of 3.8 m inner diameter, crossing the border between France and Switzerland near Geneva. There are eight major access points located in the middle of each straight sections, numbered clockwise from P1 to P8. Four even-numbered points are occupied by the experiments: L3, ALEPH, OPAL and DELPHI in this order.

Electrons and positrons are injected into LEP from a chain of five accelerators: two linacs of 200 MeV and 600 MeV, a 600 MeV Electron-Positron Accumulator (EPA), and the CERN Proton Synchrotron (PS) and the CERN Super Proton Synchrotron (SPS) operating as 3.5 GeV and 20 GeV e^+e^- synchrotrons respectively. The existing CERN proton synchrotrons, the PS and the SPS, were modified to accelerate electrons and positrons to serve as the LEP injectors. When LEP is to be filled, the PS and the SPS operate in multicycle mode, using a supercycle in which four cycles of electron and positron acceleration take place followed by one cycle of protons. By this mode of operation, filling LEP has little effect on the other experiments that run parallel with LEP using the 450 GeV proton beam from the SPS.

Electrons and positrons are constrained in the vacuum chamber along the nominal orbit by the electromagnetic guide field system. The system consists of dipole, quadrupole and sextupole magnets, dipole correctors in horizontal and vertical directions, rotated quadrupoles, and electrostatic deflectors. Each of the eight curved sections are occupied by seven sets of standard cells consisting of two groups of six bending dipoles supplemented by two quadrupoles, two sextupoles and a horizontal and a vertical orbit correctors. The beams are bent by the dipole field of about 0.1 T, which is unusually low as a circular accelerator in order to reduce the radiative energy loss. The quadrupoles produce alternating-gradient focusing, and the sextupoles are used to compensate the energy dependence of the focusing strength.

In the middle of the eight straight sections are the interaction points. Four of them are surrounded by solenoidal magnets used by the detectors of the experiments. As mentioned in the previous section, beams are focused tightly at the interaction points by the strong quadrupole field generated by a set of super-conducting magnets called 'low-β' magnets to obtain maximum luminosity. Typical transverse dimension of the beam at an interaction point is about $10\,\mu$m $\times 250\,\mu$m in the vertical and horizontal plane respectively. The longitudinal dimension is typically $\sim$2 cm. In addition, a pair of quadrupole magnets rotated by 45° about their axes are installed around each solenoid, to compensate coupling effect introduced by the solenoid between horizontal and vertical betatron oscillations.

It is very important for a storage ring to maintain high vacuum to minimize particle losses due to collisions with residual gas. The LEP vacuum chamber is also subject to severe heating coming from synchrotron radiation. In addition, it must be capable of effectively shielding the radiation to prevent damage caused to the materials of various equipments in the tunnel. The vacuum chamber is therefore made of aluminum covered with a lead cladding. The static pressure achieved without beams is 8×10^{-12} torr. It rises to $\sim 10^{-9}$ torr in the presence of beams, due to gas desorption from the inner wall provoked by the radiation. With this level of vacuum, a typical LEP fill can last $\sim$12 hours before a refilling becomes necessary.

The energy lost by synchrotron radiation is replenished by the RF acceleration system. Initially, the RF system consisted of 128 RF cavities made of copper, powered by sixteen 1 MW klystrons. During the shutdown between 1991 and 1992, eight of the cavities were removed to make room for electrostatic separators necessary for the eight-bunch 'pretzel scheme' operation. After the runs of

1994, 8 cavities made of super-conducting (SC) material are installed to increase the beam energy upto 136 GeV. After the runs of 1995, 128 SC caviteis and 36 SC cavities were installed in the winter and summer shutdown. The number of cavities and acceleration voltage are listed in Table 2.1.

Energy	Cu cavity	SC cavity	Acceleration Voltage
91	128	0	400 MV
133–140	120	8	470 MV
161	120	132	1606 MV
170–172	120	176	2028 MV

Table 2.1: *List of number of Cu and super-conducting cavities for the different LEP operations together with the acceleration voltage.*

2.2 The OPAL Detector

OPAL (**O**mni-**P**urpose **A**pparatus for **L**EP) is a multipurpose apparatus designed to reconstruct efficiently and identify all types of e^+e^- events. Full details of the OPAL detector can be found in reference [16]. The main part of the detector consists of many subdetectors which can conveniently be classified into five elements:

- A central detector which measures the positions, directions and momenta of charged tracks as well as their energy losses.
- An electromagnetic calorimeter which identifies electrons and photons by measuring their energies.
- A hadron calorimeter which measures the energies of hadrons and helps the muon identification.
- A muon detector which identifies muons by measuring their positions and directions behind the hadron calorimeter.
- A forward detector which measures the luminosity by counting low angle Bhabha scattering events.

The whole detector surrounds the beam pipe with the center of the detector at the nominal interaction point. Surrounding the central detector is a solenoidal coil which provides the detector with a 0.435 T of uniform magnetic field parallel to the beam. The iron return yoke of the magnet serves also as the absorption material of the hadron calorimeter. A schematic view of the general layout of the detector is shown in Figure 2.2. Figure 2.3 shows cross-sections of the detector by the x-y and z-x planes.

2.2.1 The Central Detector

The Central Detector consists of a Silicon Microvertex detector and three drift chamber devices, the vertex detector, jet chamber and surrounding Z-chambers situated inside a pressure vessel holding a pressure of 4 bar. These subdetectors except for the silicon microvertex detector are gas chambers and

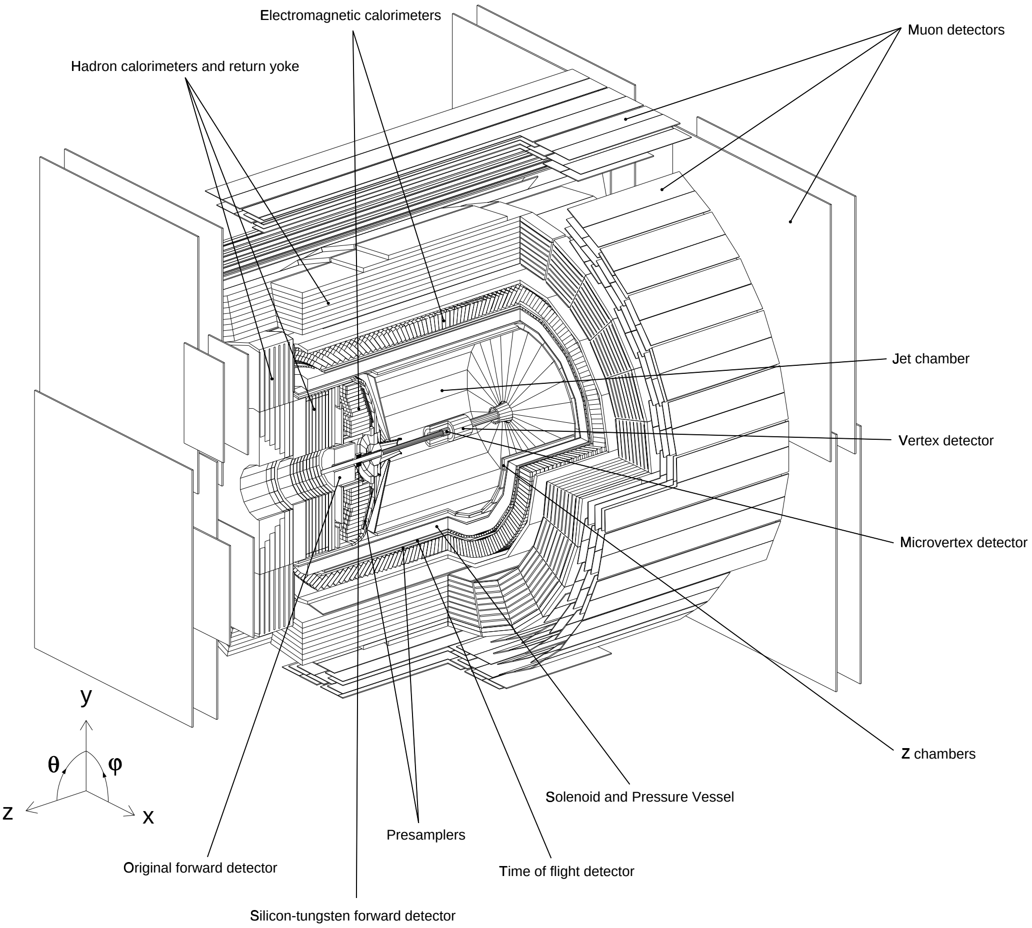

Figure 2.2: *Schematic view of the OPAL detector.*

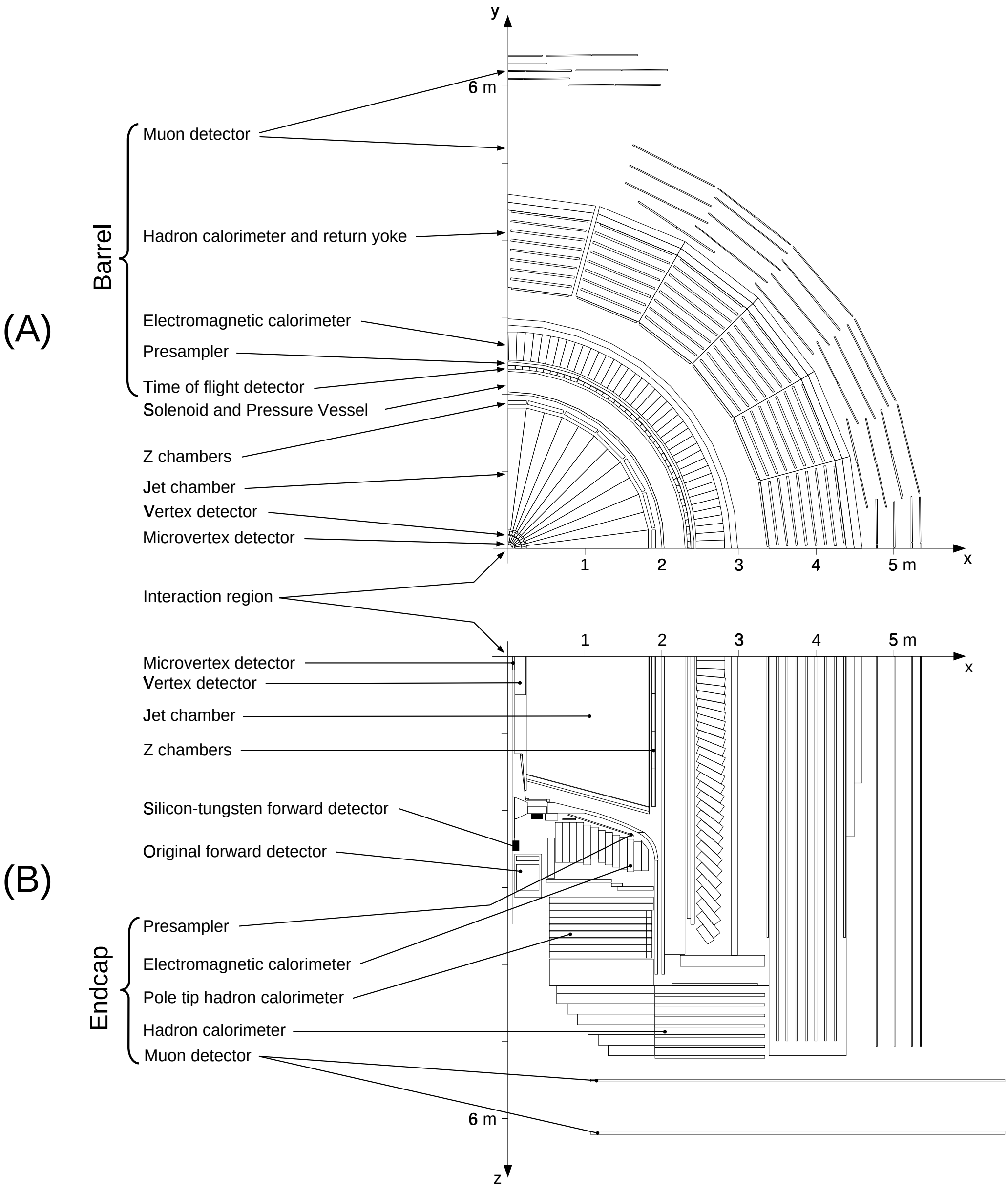

Figure 2.3: *Cross-sections of a quadrant of the OPAL detector (A) perpendicular to the beam and (B) parallel to the beam.*

use the same mixed gas, argon (88.2%), methane (9.8%) and isobutane (2.0%). The central detector is inside a solenoid supplying a uniform axial magnetic field of 0.435 T. Originally (<1991) there was no Silicon detector and the inner wall of the pressure vessel at 7.8 cm radius formed the beam pipe. This beam pipe consists of 0.13 cm thick carbon fiber with a 100μm aluminum inner lining. In 1991 a second beam pipe at a radius of 5.35 cm, consisting of 0.11 cm thick Beryllium, was added and the Silicon detector was inserted between them.

Silicon Microvertex Detector The Silicon Microvertex Detector (SI) was installed in 1991. At that time the detector had only r–ϕ readout. The detector has been upgraded several times and now is called Phase III Micro Vertex Detector (μVTX3) [17]. The detector consists of two layers of Silicon Micro Strip Detectors placed at radii of 61 mm and 75 mm. Figure 2.4 (A) shows the layout of ladders in r–ϕ plane. The angular coverage of the layers are $|\cos\theta| < 0.93$ and $|\cos\theta| < 0.90$ for inner and outer layers, respectively. The inner(outer) layer consists of 12 (15) ladders. Each ladder consists of 5 r–ϕ and 5 r–z silicon wafers glued back-to-back. 3 (2) out of 5 sets of wafers forms long (short) ladders and those wafers are daisy chained together. Figures 2.4 (B) and (C) show schematic views of a ladder and the whole Silicon Microvertex Detector layout, respectively. The strip has 25 μm pith and the signal is readout at 50 μm pitch in r–ϕ and 100 μm pitch in r–z. The intrinsic spatial resolution is $\sim$5μm in r–ϕ and $\sim$13μm in r–z. The ladders are tilted to close r–ϕ gap. The charactaristics of the Silicon Microvertex detector are listed in Table 2.2.

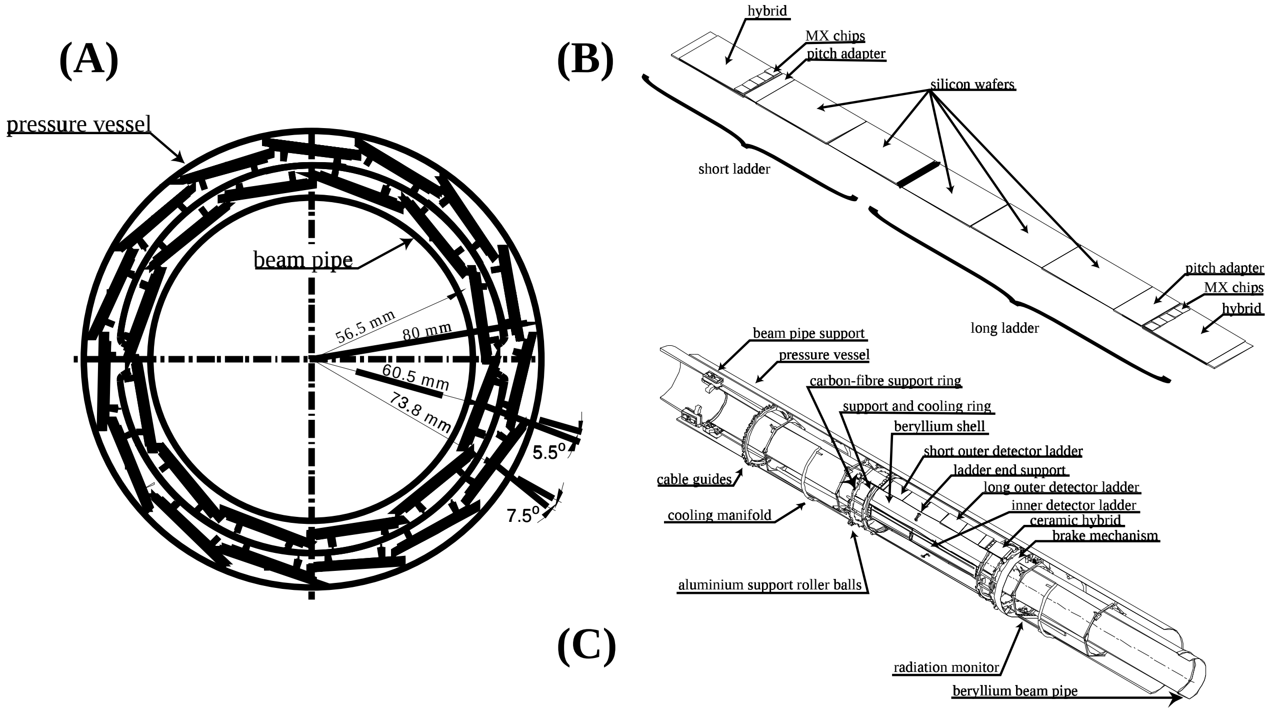

Figure 2.4: *Schematic view of Silicon Micro Vertex detector. (A) cross section view (B) a set of short and long ladders (C) Cut away view.*

	Inner	Outer	r–ϕ	r–z
Acceptance	<0.93	<0.90		
Number of ladders	11	64		
Average radius	61 mm	75 mm		
Readout strip pitch			50 μm	100 μm
Spatial resolution			∼5 μm	∼13 μm

Table 2.2: *Characteristics of the Silicon Micro Vertex Detector.*

Vertex Detector The vertex detector (CV) is a high precision cylindrical jet drift chamber. It is 100 cm long with a radius of 23.5 cm and consists of two layers of 36 sectors each. The inner layer contains the axial sectors, each containing a plane of 12 sense wires strung parallel to the beam direction. The wires range radially from 10.3 to 16.2 cm with a spacing of 0.583 cm. The outer layer contains the stereo sectors each having a plane of 6 sense wires inclined at a stereo angle of ∼4°. The stereo wires lie between the radii 18.8 and 21.3 cm with a spacing of 0.5 cm. The angular coverage of inner and outer layers are $|\cos\theta| < 0.95$ and $|\cos\theta| < 0.92$, respectively.

A precise measurement of the drift time to the axial sector sense wires allows the r-ϕ position to be calculated by an accuracy of 55 μm. Measuring the time difference between signals at either end of the sense wires allows a fast but relatively coarse z coordinate that is used by the OPAL track trigger and in pattern recognition. A more precise z measurement is then made by combining axial and stereo drift time information offline. The r-z position resolution is 700 μm Multiple hits on a wire can be recorded.

Jet Chamber The jet chamber (CJ) is a cylindrical drift chamber of length 400 cm with an outer radius of 185 cm and an inner radius of 25 cm. The chamber consists of 24 identical sectors each containing a sense wire plane of 159 wires strung parallel to the beam direction. The spacing between anode wires is 1.0 cm. The end planes are conical and can be described by $|z| = 147 + 0.268 \times R(\text{cm})$.

The coordinates of wire hits in the r-ϕ plane are determined from a measurement of drift time. The z coordinate is measured using a charge division technique. The spatial resolution for each measured point is 135 μm and 6 cm for r–ϕ and r–z directions, respectively. Summing the charges received at each end of a wire allows the energy loss, dE/dx to be calculated. The resolution of dE/dx for tracks with more than 130 measured points are 3.1 % for isolated muons and 3.8 % for minimum ionizing pions. Measurement of the curvature of the tracks provides a precise momentum measurement. The momentum resolution for 45 GeV track is 6.8%. The momentum resolution for all momenta is given by

$$\frac{\sigma_{p_t}}{p_t} = 1.4 \times 10^{-3}\, p_t\,(\text{GeV}) \oplus 0.02$$

including a term due to multiple scattering.

Z-Chambers The Z-chambers (CZ) provide a precise measurement of the z coordinate of tracks as they leave the jet chamber. They consist of a layer of 24 drift chambers 400 cm long, 50 cm wide and 5.9 cm thick covering 94% of the azimuthal angle and the polar angle range $|\cos\theta| < 0.72$. Each chamber is divided in z into 8 cells of 50 cm×50 cm, with every cell containing 6 sense wires spaced at 0.4 cm.

	Vertex Detector		Jet Chamber		Z-Chamber
	axial	+stereo	159 hits	$\geq$ 8 hits	
Acceptance	<0.95	<0.92	<0.73	<0.98	<0.72
Spatial resolution ($\Delta\phi$)	55 μm	—	135 μm		15 mm
(Δz)		700 μm	6 cm		2.5 mm
dE/dx resolution			3.8 %		

Table 2.3: *Characteristics of the tracking chambers.*

Combined Tracking Performance Tracks are reconstructed primarily only from the information of the jet chamber. Then the tracks are refitted with measured points in the other tracking chambers. The chracteristics of the tracking chambers are summurized in Table 2.3. Finally the tracks are connected to the silicon micro vertex detector hits. Table 2.4 summarizes the measured resolution for the jet chamber only, for all tracking chambers, and for all central detectors. Figure 2.5 shows the impact parameter distributions measured from $Z^0 \to \mu^+\mu^-$ events.

Detector	σ_p/p^2	σ_{d0}	σ_{z0}
Jet Chamber	1.4	113 μm	2.7 cm
All tracking chambers	1.3	40 μm	2 mm
+ Silicon Micro Vertex	1.25	18 μm	24 μm

Table 2.4: *The measured resolutions, σ_p/p^2, σ_{d0}, and σ_{z0} for the jet chamber only, for all tracking chambers and for all central detectors.*

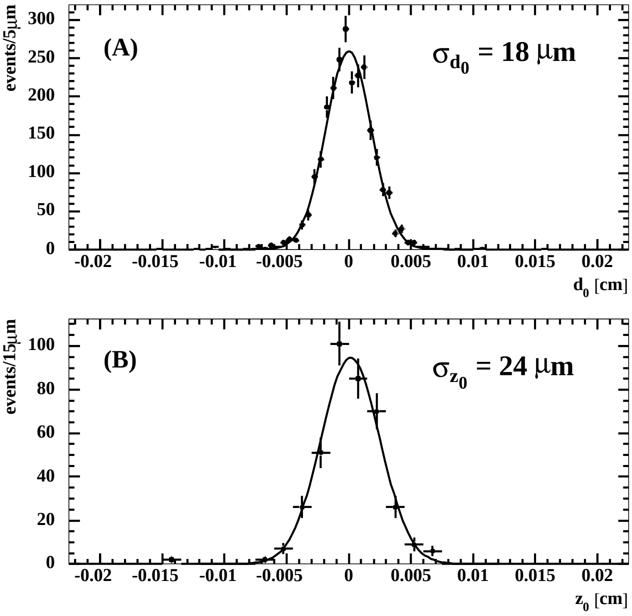

Figure 2.5: *Measured impact parameter resolution for (A) r–ϕ and (B) r–z directions obtained from the muon pair events taken at the Z^0 pole.*

2.2.2 Electromagnetic Calorimeter

The function of the electromagnetic calorimeter is to detect and identify electrons and photons. It consists of a lead glass total absorption calorimeter split into a barrel and two endcap arrays. This arrangement together with two lead-scintillator forward calorimeters and two silicon tungsten detectors in the forward detector makes the OPAL acceptance for electron and photon detection almost 99% of the solid angle.

The presence of ∼2 radiation lengths of material in front of the calorimeter (mostly due to the solenoid and the pressure vessel), results in most electromagnetic showers initiating before reaching the lead glass. Presampling devices are therefore installed in front of the lead glass in the barrel and endcap regions to improve overall spatial and energy resolution and to give additional γ/π^0 and electron/hadron discrimination. In front of the Barrel Presampler is the Time of Flight Detector.

Time-Of-Flight Counters The Barrel time-of-flight (TB) system provides charged particle identification in the range 0.6 to 2.5 GeV, fast triggering information and an effective rejection of cosmic rays. It consists of 160 scintillation counters forming a barrel layer 684 cm long at a mean radius of 236 cm, and surrounds the OPAL coil covering the polar angle range $|\cos\theta|< 0.82$. Typical time resolution is ∼460 ps.

Barrel Electromagnetic Presampler The Barrel Electromagnetic Presampler (PB) consists of 16 chambers forming a cylinder of radius 239 cm and length 662 cm covering the polar angle range $|\cos\theta|< 0.81$. Each chamber consists of two layers of drift tubes operated in the limited streamer mode with the anode wires running parallel to the beam direction. Each layer of the tubes contains 1 cm wide cathode strips on both sides at ±45°to the wire direction. Spatial positions can then be determined by reading out the strips in conjunction with a measurement of the charge collected at each end of the wires to give a z coordinate by charge division. The hit multiplicity is approximately proportional to the energy deposited in the material in front of the presampler allowing the calorimeter shower energy to be corrected with a corresponding improvement in resolution.

Barrel Lead Glass Calorimeter The barrel lead glass calorimeter (EB) consists of a cylindrical array of 9440 lead glass blocks at a radius of 246 cm covering the polar angle range $|\cos\theta| <0.82$. Each block is 24.6 radiation lengths, 37 cm in depth and $\sim 10 \times 10$ cm^2 in cross section. The longitudinal axis of each block is pointing towards the interaction region to minimize the probability of the particles traversing more than one block. The focus of this pointing geometry is slightly offset from the nominal collision point in order to reduce particle losses in the gaps between blocks.

Čerenkov light from the passage of relativistic charged particles through the lead glass is detected by a 3 inch diameter phototube at the base of each block. The energy resolution for 45 GeV electrons are measured to be 2%. The energy resolution for all energy is given by $18.0\%/\sqrt{E}$. The characteristics of the barrel electromagnetic calorimeter are listed in Table 2.5.

Endcap Electromagnetic Presampler The endcap presampler (PE) is a multiwire proportional counter located in the region between the pressure bell and the endcap lead glass detector. The device consists of 32 chambers arranged in 16 sectors covering all ϕ and the polar angle range $0.83 <|\cos\theta|< 0.95$.

Endcap Electromagnetic Calorimeter The endcap electromagnetic calorimeter (EE) consists of two dome-shaped arrays of 1132 lead glass blocks located in the region between the pressure bell and the pole tip hadron calorimeter. It has an acceptance coverage of the full azimuthal angle and $0.81 < |\cos\theta| < 0.98$.

In contrast to the barrel calorimeter, the endcap lead glass blocks follow a non-pointing geometry being mounted coaxial with the beam line. The lead glass blocks provide typically 22 radiation lengths of material and come in three lengths (38, 42 and 52 cm) to form the domed structure following the external contours of the pressure bell.

The blocks are read out by special Vacuum Photo Triodes (VPTs) operating in the full OPAL magnetic field. The energy resolution for 45 GeV electron is measured to be 3%. The energy resolution for all energy is given by $21.6\%/\sqrt{E}$. The characteristics of the endcap electromagnetic calorimeter are listed in Table 2.5.

	Barrel	Endcap
Acceptance	<0.82	0.81 – 0.95
Typical block size	$\sim 10\times \sim 10\times 37$ cm	$9.2\times 9.2\times 52$ cm
Depth	24.6 X_0	$\sim$22 X_0
Energy Resolution	$18.0\%/\sqrt{E}$	$21.6\%/\sqrt{E}$
Energy Resolution at 45 GeV	$\sim$2.2 %	$\sim$3 %
Spatial Resolution (at 6 GeV)	$\sim$11mm	$\sim$11mm
Typical material in front	$\sim$2 X_0	$\sim$2 X_0

Table 2.5: *List of parameters of electromagnetic calorimeters*

2.2.3 Hadron Calorimeter

The hadron calorimeter is built in three sections - the barrel, the endcaps and the pole-tips. By positioning detectors between the layers of the magnet return yoke a sampling calorimeter is formed covering a solid angle of 97% of 4π and offering at least 4 interaction lengths of iron absorber to particles emerging from the electromagnetic calorimeter. Essentially all hadrons are absorbed at this stage leaving only muons to pass on into the surrounding muon chambers.

To correctly measure the hadronic energy, the hadron calorimeter information must be used in combination with that from the preceding electromagnetic calorimeter. This is necessary because hadronic interactions are likely to occur in the 2.2 interaction lengths of material that exists in front of the iron yolk. The characteristics of the hadron calorimeters are listed in Table 2.6.

Hadron Endcap and Barrel Calorimeter The barrel region (HB) contains 9 layers of chambers sandwiched between 8 layers of 10 cm thick iron. The barrel ends are then closed off by toroidal endcap regions (HE) which consist of 8 layers of chambers sandwiched between 7 slabs of iron.

The chambers themselves are limited streamer tube devices strung with anode wires 1 cm apart in a gas mixture of isobutane(75%) and argon(25%) that is continually flushed through the system. The signals from the wires themselves are used only for monitoring purposes. The chamber signals result from induced charge collected on pads and strips located on the outer and inner surfaces of the chambers respectively.

The layers of pads are grouped together to form towers that divide up the detector volume into 48 bins in ϕ and 21 bins in θ. The analogue signals from the 8 or so pads in each chamber are then summed to produce an estimate of the energy in hadronic showers.

The strips consist of 0.4 cm wide aluminum that run the full length of the chamber, centered above the anode wire positions. They hence run parallel to the beam line in the barrel region and in a plane perpendicular to this in the endcaps. Strip hits thus provide muon tracking information with positional accuracy limited by the 1 cm wire spacing. Typically, the hadronic shower initialized by a normally incident 10 GeV pion produces 25 strip hits and generates a charge of 600 pc.

Hadron Pole-Tip Calorimeter Complementing the barrel and endcap regions, the pole-tip (HP) extends the coverage of hadron calorimetry from $|\cos\theta|$ of 0.91 down to 0.99. The sampling frequency in this region is increased to 10 in an effort to improve the OPAL energy resolution in the forward direction.

The detectors themselves are 0.7 cm thick multiwire proportional chambers containing a gas mixture of CO_2(55%) and n-pentane(45%), strung with anode wires at a spacing of 0.2 cm. Again, the chambers have pads on one side (of typical area 500 cm^2) and strips on the other. Corresponding pads from the 10 layers then form towers analogous to the treatment in the rest of the calorimeter.

	Barrel	Endcap	Pole Tip
Acceptance	< 0.81	0.81–0.91	0.91–0.99
Number of layers	9	8	10
Pitch of Strips	10mm	10mm	10mm
Size of towers ($\Delta\phi$)	$\sim$7.5°	$\sim$7.5°	$\sim$11°
($\Delta\theta$)	$\sim$5°	$\sim$5°	$\sim$4°
Energy resolution	$120\%/\sqrt{E}$	$120\%/\sqrt{E}$	$120\%/\sqrt{E}$

Table 2.6: *List of properties of Hadron calorimeters*

2.2.4 Muon Detector

The muon detector aims to identify muons in an unambiguous way from a potential hadron background. To make the background manageable, particles incident on the detector have traversed the equivalent of 1.3 m of iron corresponding to 7 interaction length, reducing the probability of a pion not interacting to be less than 0.001. The muon detector covers 93% of the solid angle. The characteristics of the muon detectors are listed in Table 2.7.

Barrel Muon Detector The barrel region (MB) consists of 110 drift chambers that cover the acceptance $|\cos\theta|$ <0.68 for four layers and $|\cos\theta|$ <0.72 for one or more layers. The chambers range in length between 10.4 m and 6 m in order to fit between the magnet support legs and all have the same cross sectional area of 120 cm×9 cm.

Each chamber is split into two adjoining cells each containing an anode signal wire running the full length of the cell, parallel to the beamline. The inner surfaces of the cells have 0.75 cm cathode strips etched in them to define the drift field and in the regions directly opposite the anode wires are diamond shaped cathode pads. In all, six signals are read out from each cell namely, one from each end of the anode wire and four from the cathode pads and are digitized via an 8-bit FADC.

Spatial position in the ϕ plane is derived using the drift time onto the anode and can be reconstructed to an accuracy of better than 0.15 cm. A rough estimate of the z coordinate is also achieved by using the difference in time and pulse height of the signals arriving at both ends of the anode wire. A much better measure of the z coordinate is given by using induced signals on two sets of cathode pads whose diamond shape repeats every 17.1 cm and 171 cm respectively. This results in a z coordinate accurate to 0.2 cm, modulo 17.1 cm or accurate to 3 cm modulo 171 cm.

Endcap Muon Detector Each endcap muon detector (ME) consists of two layers of four quadrant chambers (6 m×6 m) and two layers of two patch chambers (3 m×2.5 m) for an angular coverage of $0.67 < |\cos\theta| < 0.985$. Because of the magnet support material there are four uncovered regions . Each chamber is an arrangement of two layers of limited streamer tubes in the plane perpendicular to the beam line, where one layer has its wires horizontal and the other vertical.

The basic streamer tube used has a cross section of 0.9 cm×0.9 cm with the inner walls coated with a carbon-suspension cathode. Each plane of tubes is open on one side and closed on the other to rows of aluminum strips 0.8 cm wide. The strips on the open side, run perpendicular to the tube anode wires and typically have charge induced over five or so strips. By finding a weighted average using the recorded pulse heights, the streamer is located to better than 0.1 cm. The strips on the closed side run parallel to the tube wires and can only give that coordinate to the nearest wire or $0.9/\sqrt{12}$ cm.

Within each chamber therefore, with two layers of tubes each with two layers of strips, the x and y coordinates of a track can be measured once accurately and once relatively coarsely. As with the barrel region, the actual position of the strips is known to about 0.1 mm via survey information.

	Barrel	Endcap
Acceptance	<0.72	0.67–0.98
Absorption length in front	$\sim 8\ \lambda_{\rm int}$	8–14 $\lambda_{\rm int}$
Number of layers	4	4
Position Resolution	∼1.5 mm (ϕ)	∼1.0 mm (y)
	∼2.0 mm (θ)	∼3.0 mm (x)
Direction Resolution	5 mrad	5 mrad

Table 2.7: *List of properties of Muon detectors.*

2.2.5 The Forward Detector

The forward detector consists of an array of devices, listed below, whose primary objective is to detect low angle Bhabha scattering events as a way of determining the luminosity. It also complements the electromagnetic calorimeters to give a near 4π acceptance to the OPAL detector.

To achieve this, the forward detector has clean acceptance for particles between 25 and 120 mrad from the interaction point.

Calorimeter The forward calorimeter (FD) consists of 35 sampling layers of lead-scintillator sandwich divided into a presampler of 4 radiation lengths and the main calorimeter of 20 radiation lengths. The energy resolution obtained from Bhabha events is $17\%/\sqrt{E}$.

Tube Chambers There are three layers of proportional tube chambers positioned between the presampler and main sections of the calorimeter. The positioning is known to ±0.05 cm and they can give the position of a shower centroid to ±0.3 cm.

Gamma Catcher The gamma catcher (GC) is a ring of lead scintillator sandwich sections of 7 radiation lengths thickness. They plug the hole in acceptance between the inner edge of EE and the start of the forward calorimeter. Any electrons or photons with more than 2 GeV of energy can be detected, thus providing an efficient veto for radiative events.

Far Forward Monitor The far forward monitor counters are small lead-scintillator calorimeter modules, 20 radiation lengths thick, mounted either side of the beampipe 7.85 m from the intersection region. They detect electrons scattered in the range 5 to 10 mrad that are deflected outwards by the action of LEP quadrupoles.

Silicon Tungsten Detector The silicon tungsten detector (SW) is a sampling calorimeter consisting of 19 layers of silicon detectors and 18 layers of tungsten. There are 2 calorimeters at ±238.94cm in z from the interaction point with an angular acceptance of 25 mrad to 59 mrad. At the front of each calorimeter is a bare layer of silicon to detect preshowering, the next 14 silicon layers are each behind 1 radiation length (3.8mm) of tungsten and the final 4 layers are behind 2 radiation lengths (7.6 mm) of tungsten.

Each silicon layer consists of 16 wedge shaped silicon detectors. The wedges cover 22.5° in ϕ with an inner radius at 6.2 cm and an outer one at 14.2 cm. The wedges are subdivided into 64 pads (32 in r and 2 in ϕ) giving a total of 38912 channels which are read out individually. Adjacent wedges in a layer are offset by 800μm in z and positioned in such a way that there is no gap in the active area of the silicon. Consecutive layers in the detector are offset in ϕ by half a wedge (11.25°) so that any cracks between the tungsten half–rings do not line up.

2.2.6 The Trigger

Events are only recorded by the data acquisition system if they satisfy certain trigger conditions. The detail of the OPAL trigger system can be found in reference [18].

Subdetector trigger signals divide into two categories, 'stand-alone' signals such as multiplicity counts or energy sums, and lower threshold signals from a 6×24 binning in θ and ϕ respectively. The trigger processor makes its decision by forming correlations in space between subdetectors in θ/ϕ together with the stand-alone signals.

2.2.7 Online Dataflow

When a beam crossing is selected by the trigger as containing a potentially interesting event, the subdetectors are read out. Each one of the sixteen subdetectors is read out separately by its own special front-end readout electronics into its local system crate(s) ('LSC') The subevent structures from the different LSCs (eighteen of them, including the trigger and track trigger) are assembled by the event builder ('EVB'). The EVB sits in a single VME crate, and is connected to the LSCs via high-speed memory-map 'VIC' links.

When the complete events have been assembled by the EVB, they are passed in sequence to the filter via another VIC link. In the filter, the events are checked, analyzed, monitored and compressed before being written to disk. Some obvious junk events, typically 15-35 % of all triggers, are rejected. The event headers of all events reaching the filter, rejected or not, are recorded on disk to help in book-keeping. The events are written in data files with typically 20 Mbyte long.

Chapter 3

Analysis

This chapter describes the method of search for the Higgs boson in LEP2 energies. The search topologies relevant for this study and those of backgrounds are described in sections3.1 and 3.2, respectively. Section 3.3 shows the experimental and Monte Carlo data samples used in the analysis. The techniques which are important to the analysis are described in section 3.4. The event selections are described in sections 3.5, 3.6, 3.7, and 3.8.

3.1 Search Topologies

At LEP2 energies the Higgs boson is dominantly produced via the higgsstrahlung process. The contribution from the fusion processes is so small ($\sim$1%) that the selections are optimized to the higgsstrahlung process. In the higgsstrahlung process the final state of the Higgs boson production can be categorized to four channels according to the decay modes of the Z^0 and the Higgs boson; i.e., (1) final state with four jets, (2) final state with missing energy, (3) final state with tau leptons, and (4) final state with electrons and muons, as shown in Figure 3.1.

Four Jets Channel The Four Jets channel arises when both the Z^0 and the Higgs boson decay hadronically. Since hadronic branching fraction of the Higgs boson is about 92 %, this channel has the largest branching fraction. However, this channel suffers from a large background from $e^+e^- \to q\bar{q}$ with gluon emmission, and $e^+e^- \to W^+W^- \to q\bar{q}q\bar{q}$ events. In order to reduce those background events, presence of b flavour is required in the final state, which is not included in the W^+W^- production. Hence, the search in this channel is restricted to the b decay of the Higgs boson. The branching fraction of the channel is about 60 % at m_{H^0} =65 GeV. The final state of this channel consists of four energetic jets. Two of the jets should have b flavour and the invariant mass of the other two jets has to be consistent with m_{Z^0}.

Missing Energy channel The Missing Energy channel arises when the Z^0 invisiblly decays in the higgsstrahlung process. In addition to the higgsstrahlung process this channel has small contribution from the W^+W^- fusion process. The contiributions of the W^+W^- fusion process are 4.1% for m_{H^0} =65 GeV at $\sqrt{s}$ =161 GeV and 4.0% for m_{H^0} =68 GeV at $\sqrt{s}$ =172 GeV. The final state consists of two acoplaner hadronic jets with invariant mass m_{H^0}. For the dominant production process with higgsstrahlung, the missing mass is close to m_{Z^0}. The branching fraction of this channel is about 20 % at m_{H^0} =65 GeV. The main backgrounds to this channel are $e^+e^- \to q\bar{q}$ events with large undetected energy, $W^+W^- \to \ell\nu q\bar{q}$ in which lepton escapes from detection, and Z^0+ $Z^0/\gamma^* \to \nu\bar{\nu}q\bar{q}$ events.

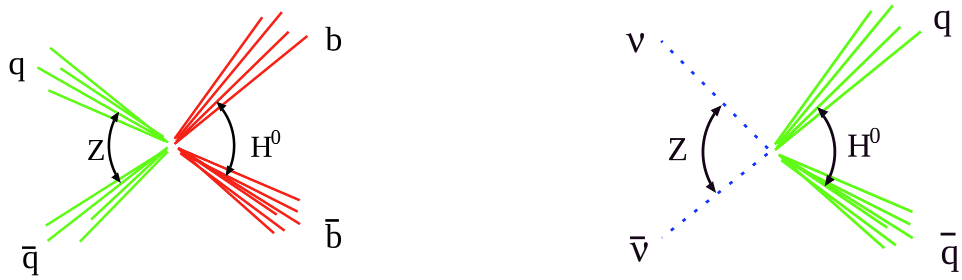

Four Jets Channel (∼60%) **Missing Energy Channel (∼20%)**

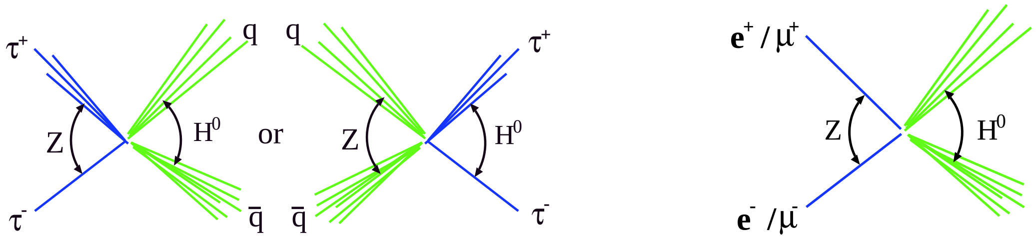

Tau Channels (∼3% + ∼6%) **Electron and Muon Channels (∼3% + ∼3%)**

Figure 3.1: *Schematic view of four final state topologies relevant to this study.*

Tau channels The Tau channels occurs when the Higgs decays hadoronically and the Z^0 decays to a tau pair (referred as $\tau\tau q\bar{q}$ channel hereafter) or when the Higgs decays to a tau pair and the Z^0 decays hadorinically ($q\bar{q}\tau\tau$ channel). These channels are characterized by a presence of two isolated energetic tau leptons and two hadronic jets. One of the invariant masses reconstructed from the tau pair and the two jets should be consistent with m_{Z^0}. These channels have branching fractions of about 3% and 6 % for the $\tau\tau q\bar{q}$ and $q\bar{q}\tau\tau$ channels, respectively.

Electron and Muon channels The Electron and Muon channels arise when the Z^0 decays into a pair of electrons or muons in the higgsstrahlung process. The electron channel contains small contribution from the Z^0Z^0 fusion process. The contribution from the Z^0Z^0 fusion process is 2.3% for m_{H^0} =65 GeV at $\sqrt{s}$ =161 GeV and 2.2% for m_{H^0} =68 GeV at $\sqrt{s}$ =172 GeV. Although these channels have the smallest branching fraction of only 6.7%, the final state is very clear. The discovery potential is expected to be high because of a low background condition. The final state contains a pair of energetic, isolated, and oppositely charged leptons with same spices. The final state is also characterized by the invariant mass of the lepton system being consistent with m_{Z^0}. The mass of the Higgs boson can be reconstructed as the recoil mass of the lepton pair system.

3.2 Background

The Standard Model backgrounds which mainly contribute to the search are categorized to three types of events; multihadronic, four-fermion and two-photon events. Cross-sections of the Standard Model processes are shown in Figure 3.2 as a function of the cernter-of-mass energy.

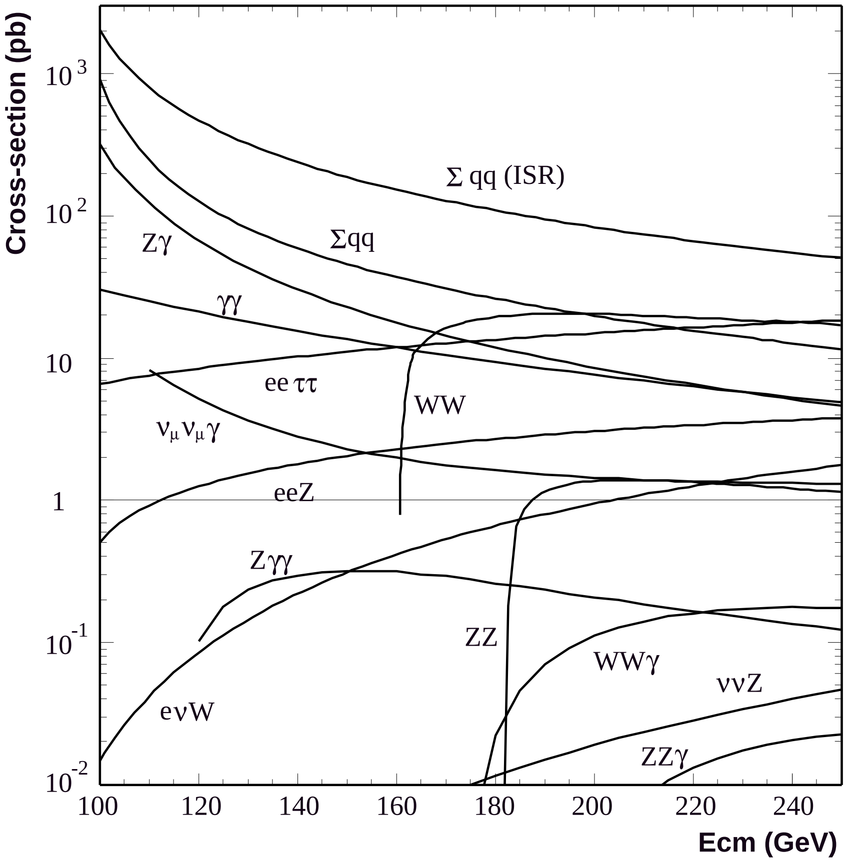

Figure 3.2: *Cross-sections of the Standard Model processes as a function of the center-of-mass energy.*

Mulithadronic events Multihadronic events are generated via the process $e^+e^- \to Z^0/\gamma^* \to q\bar{q}$. At LEP2 energies bulk of multihadronic events are produced with so-called "radiative return" process in which initial state photons are radiated to reduce the effective center-of-mass energy to the Z^0 pole, at which the cross-section is greatly enhanced. In this case the events have an energetic photon or a large missing energy in the beam direction. The Feynman diagram of the multihadronic events is shown in Figure 3.3 (A). The cross-section of the process is ~100 pb at LEP2 energies. Multihadronic events can be the main background source for all search channels because of its large cross-section comparing to the signal cross-section of ~1 pb. In the four-jets channel, in particular, multihadronic events with b flavour are the dominant background sources together with the $W^+W^- \to q\bar{q}q\bar{q}$ events.

Four-fermion events Four-fermion events consist of four fermions in the final states. At LEP2 energies the four-fermion processes include the following reactions,

- $e^+e^- \to W^+W^-$,
- $e^+e^- \to Z^0Z^{0(*)}$,
- $e^+e^- \to Z^0\gamma^*$,
- $e^+e^- \to e\nu W$, and
- $e^+e^- \to Z^0e^+e^-$.

The Feynman diagrams of these processes are shown in Figures 3.3 (B)–(E). Above the W^+W^- production threshold, the dominant process of the four-fermion events is the W-pair production. The cross-section of the W-pair production is about 3.4 pb at the center-of-mass energy of 161 GeV and 11.5 pb at 172 GeV. Hadronic decay of the W-pair production is one of the dominant background sources for the four jets channel, because the mass difference between Z^0 and W is comparable to the experimental mass resolution. The events from the processes $Z^0Z^{0(*)}$ and $Z^0\gamma^*$ have the same final state topologies as the higgsstrahlung process. These events can be the background source if the intermediate Z^{0*} or γ^* has a mass in the search region of m_{H^0}. Fortunately their cross-sections are small below the Z^0Z^0 production threshold. The cross-section of the $Z^0Z^{0(*)}$ and $Z^0\gamma^*$ production is about 0.05 pb if one requires the intermidiate Z^{0*} or γ^* to be heavier than 50 GeV.

Two-photon events Two-photon events are generated through the process $e^+e^- \to e^+e^-X$ where the system X is produced in the scattering of two quasi-real photons by $\gamma\gamma \to X$. The Feynman diagram of two-photon events is shown in Figure 3.3 (F). This type of events can be the background source of channels in which large missing energy is expected, namely the missing energy channel and the tau channels. In two-photon events most of the energy escapes to the beam pipe.

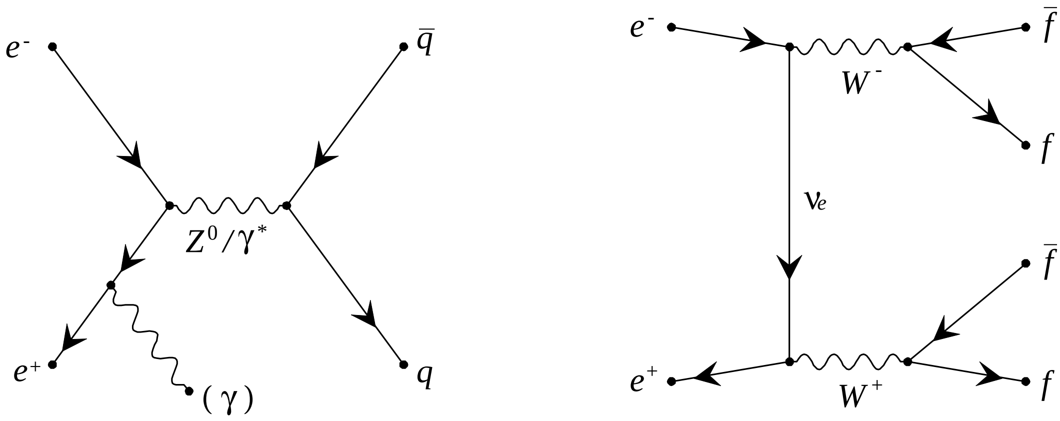

(A) multihadronic events

(B) $e^+e^-\rightarrow W^+W^-$

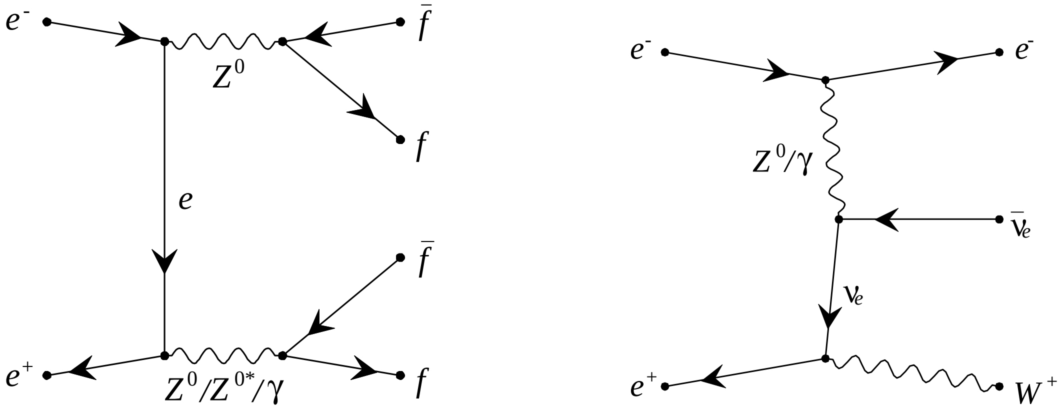

(C) $e^+e^-\rightarrow Z^0$+ $Z^0/Z^{0*}/\gamma$

(D) $e^+e^-\rightarrow e\nu_eW$

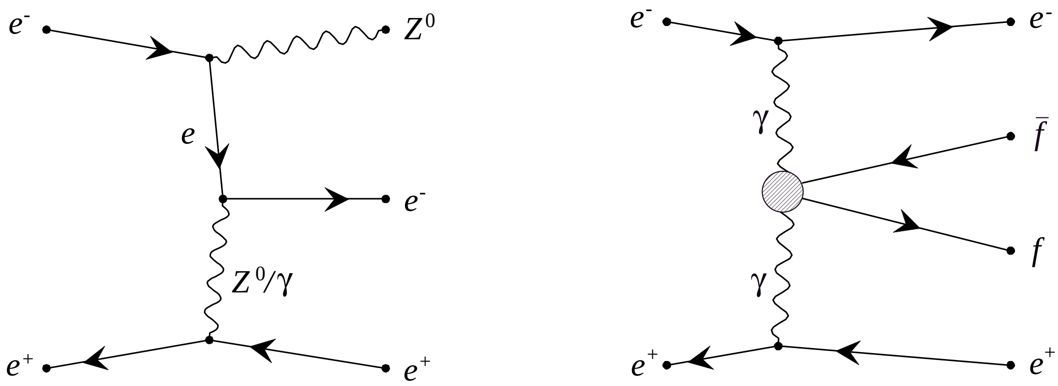

(E) $e^+e^-\rightarrow e^+e^-Z^0$

(F) Two-photon events

Figure 3.3: *Diagrams of the background processes.*

3.3 Data Sample

3.3.1 Experimental Data Sample

The data used in this study were recorded in the data-taking periods summarized in Table 3.1. In order to obtain enough well-controled data sample, calibration runs on the Z^0 pole took place before running above the Z^0 pole. Data taken at the Z^0 pole are used to calibrate the detector, to check the data quality, and to study the systematics of the event selection. For each event, detector status flags are defined in order to indicate the operating condition of the detector when the event was recorded. After requiring the relevant detector to be fully oparational, the integrated luminosities of the data collected by the OPAL detector correspond to 10.0 pb^{-1}, 1.0 pb^{-1}, and 9.4 pb^{-1} at center-of-mass energies of 161.3, 170.3 and 172.3 GeV[1]. The integrated luminosities collected in each period are listed in Table 3.1. The integrated luminosities collected in 1990–1996 are shown in Figure 3.4. As shown in the figure, the total running period in 1996 is shorter than that of other years because of installation of Super-conducting cavities. Throughout the running periods, performance of accelerator was quite well.

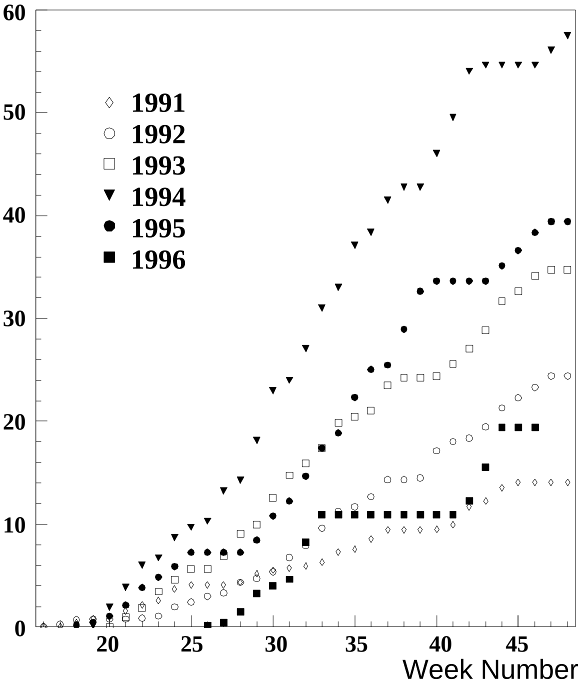

Figure 3.4: Integrated Luminosity collected in 1990–1996

3.3.2 Monte Carlo Data Sample

Data samples generated by Monte Carlo simulations are used to optimize the event selection in this study. A Monte Carlo event of a physics process is generated by an event generator as a list of four momentum vectors of the final state particles. The four vectors are then processed through a full detector simulation program to simulate the detector response. The detector simulation of the

---

[1] In this note the data collected at 161.3 GeV are referred as 161 GeV data, and the data collected at 170.3 GeV and 172.3 GeV are referred as 172 GeV data.

Period ($\sqrt{s}$)			Date			Integlated Luminosity (pb^{-1})
1996	77	(91 GeV)	Jun 13	—	Jul 8	0.55
	78	(161 GeV)	Jul 8	—	Jul 25	3.41
	79	(161 GeV)	Jul 27	—	Aug 18	6.99
	80	(91 GeV)	Oct 7	—	Oct 17	0.61
	81	(172 GeV)	Oct 19	—	Nov 3	7.85
	82	(172 GeV)	Nov 6	—	Nov 21	2.57

Table 3.1: Summary of the data-taking periods. The periods running on the Z^0 pole are the calibration runs.

OPAL detector is called GOPAL [19], which is based on GEANT 3.21 [20]. The output of GOPAL can be processed as experimental data.

The Higgs production processes are simulated by the HZHA generator [21] including the contribution from the fusion processes and the initial state radiation. The HZHA generator can generate up to two initial state photons. The generated partons are hadronized using JETSET[22], which is tuned to fit with OPAL data[23]. The signal Monte Carlo samples are generated separately for the final state topologies with fixed values of m_{H^0} between 35 GeV and 80 GeV with typically 500 events each. High statistics samples with 5,000 events are also generated with m_{H^0} around the expected mass limit to obtain higher precision for estimation of efficiencies and to study systematic uncertainty of the efficiencies.

Background Monte Carlo events are generated by a variety of event generators. The background Monte Carlo samples used to calculate the number of background events in this study are listed in Table 3.2. For the main background processes in this search, namely multihadronic four-fermion processes, other sets of Monte Carlo samples listed in Table 3.3 are generated with different event generator for estimation of the systematic uncertainties between generators.

All the Monte Carlo samples are processed in the same way as the experimental data samples.

3.4 Event Reconstruction

The events accepted by the *filter* are only the collection of *hits* at this stage. Those *hits* are reconstructed as physics quantities such as track momenta or cluster energies by an event reconstruction program. In OPAL such program is called ROPE (**R**econstruction of **O**PAL **P**hysics **E**vent). ROPE consists of a variety of *processors*. Some processors convert specific subdetector hits into physics quantities. For example, a processor performs calibration of electromagnetic energies and forms a cluster. Some processors combine data from several subdetectors and compute less detector specific quantities. Finally ROPE forms the OPAL DST (**D**ata **S**ummary **T**ape) containing a set of measured physics quantities, errors of the measurements and so on. ROPE can also read the DST or raw data and provide the environment in which more complex analysis can be made. A new DST is regenerated in order to reflect the latest calibration constants obtained from older DST. This procedure is called reROPE. In general, final physics results are obtained from the DST with the second or third generation. Part of DST components relevant in this study are listed in the followings.

Charged Track Charged tracks are reconstructed from the hits in the central tracking devices. For each charged track, the momentum, the impact parameter, dE/dx, the association to the outer

Process	Generator	Cross Section (pb)	# Events
161 GeV			
$Z^0/\gamma \to q\bar{q}(\gamma)$	PYTHIA [22]	147.4	200,000
Four-fermion	Excalibur [24]	17.1	20,000
$e^+e^-(\gamma)$	BHWIDE [25]	818.0	250,000
$\mu^+\mu^-(\gamma)$	KORALZ [26]	12.6	75,000
$\tau^+\tau^-(\gamma)$	KORALZ	12.3	100,000
$\gamma\gamma$ hadronic	PHOJET [27]	14.8 (nb)	1,000,000
	HERWIG [28]	961.0	100,000
$\gamma\gamma$ leptonic	Vermaseren [29]	4.12 (nb)	412,000
172 GeV			
$Z^0/\gamma \to q\bar{q}(\gamma)$	PYTHIA	122.7	200,000
Four-fermion	`grc4f` [30]	17.6	994,809
$e^+e^-(\gamma)$	BHWIDE	725.6	200,000
$\mu^+\mu^-(\gamma)$	KORALZ	11.1	100,000
$\tau^+\tau^-(\gamma)$	KORALZ	10.7	100,000
$\gamma\gamma$ hadronic	PHOJET	19.9 (nb)	1,000,000
	HERWIG	830.6	100,000
$\gamma\gamma$ leptonic	Vermaseren	4.23 (nb)	423,000

Table 3.2: *Background Monte Carlo samples used in this study together with the cross-sections and the generated number of events.*

Process	Generator	Cross-section (pb)	# Events Generated
161 GeV			
$Z^0/\gamma \to q\bar{q}(\gamma)$	HERWIG	150.3	100,000
Four-fermion	`grc4f`	14.0	265,400
172 GeV			
$Z^0/\gamma \to q\bar{q}(\gamma)$	HERWIG	123.5	100,000
Four-fermion	Excalibur	22.1	170,000

Table 3.3: *Background Monte Carlo samples used to study systematic errors.*

detectors, and so on, are computed.

ECAL cluster ECAL clusters are reconstructed from the barrel and the endcap electromagnetic calorimeter hits. Hits in the overlap region between the barrel and the endcaps are merged to form a cluster. The energy, the corrected cluster energy, the position, the cluster shape parameters are stored for each cluster. The energy correction includes the correction of the effect of materials in front of calorimeters.

HCAL tower cluster HCAL tower clusters are reconstructed from the hadron calorimeter towers. For each cluster, the energy and the position are stored.

HCAL strip cluster HCAL strip clusters are reconstructed from the hadron calorimeter strip hits. A HCAL strip cluster provides tracking information and helps muon identification.

Muon segment Muon segments are reconstructed from the hits in the muon detectors independently of the other tracking devices. For each Muon segment, the track direction, the track position, hit multiplicities are stored.

Forward Detector cluster Forward detector clusters are reconstructed from the hits collected in the forward detectors. The measured energy of the each forward detector element is stored.

There are several important functions to make analyses effective. In the Higgs search, particle identification and mass reconstruction play very important roles. In the higgsstrahlung process, the Higgs boson is produced recoiling against Z^0. A good Z^0 mass reconstraction gives good discrimination against the background events. To improve the resolution of mass reconstruction, a good energy flow measurement is important. Particle identification is of particular importance in the channels which are characterized by a presence of certain particles, such as electron, muon, tau and b quark.

The following sections describe the tools used in the analysis.

3.4.1 Track and Cluster Quality Condition

To remove the tracks and clusters caused by detector noise or those with bad measurement, only tracks and clusters having a good quality are used for the analysis. The requirements of a good quality track are as follows:

- The track has at least 50 % of the maximum measurable points expected in the jet chamber and at least 20 measured points.
- The track has a transverse momentum, p_{xy}, higher than 120 MeV.
- The distance of closest approach to the beam axis, $|d_0|$, should be less than 2.5 cm, and the z coordinate of the point of the closest approach to the nominal interaction point, z_0, should satisfy $|z_0| <$20 cm.
- The χ^2 of the track fit in r–ϕ and r–z direction are both smaller than 100.

The requirement of the good ECAL and HCAL clusters are the followings,

- The ECAL cluster has raw energy higher than 100 MeV for the barrel and 200 MeV for the endcaps.

- The endcap ECAL cluster is formed from at least two lead glass blocks.
- The HCAL tower cluster has energy higher than 0.6, 0.6, and 2.0 GeV for the barrel, the endcaps, and the poletips, respectively.

The requirement of the good ECAL and HCAL clusters are the followings,

3.4.2 Energy Flow Algorithm

The easiest way to determine the energy flow of an event is simply to add all ECAL and HCAL clusters. In this case *energy flow particles* of the event are all ECAL and HCAL tower clusters. However, in the OPAL detector, the momentum measurement in the central tracker has better resolution than the energy measurement in the calorimeter for the low momentum charged particles. This applies to the most of the tracks. Measurement of the direction is also important in the mass reconstruction. The angular resolution of the charged track is better than that of calorimeter cluster. However, simply adding up the charged tracks, ECAL, and HCAL clusters causes double counting of the charged particle contributions. The resolution of energy flow becomes worse. Therefore the energy algorithm starts from to set all charged tracks as energy flow particles to improve the direction measurement and try to add neutral particle contribution from calorimeter information to avoid the double counting.

The energy flow algorithm first tries to find charged track association to the ECAL and HCAL clusters. If a charged track has associated clusters, the charged track contribution is subtracted from the calorimeter energy in the following way. The calorimeter cluster is removed if the corrected energy of the cluster is smaller than the threshold energy, $E_{\mathrm{th}}(p,\theta)$. If the corrected energy of the cluster is larger then $E_{\mathrm{th}(\mathrm{p},\theta)}$, the mean expected energy, $E_{\mathrm{mean}}(p,\theta)$, is subtracted from the calorimeter cluster. The functions $E_{\mathrm{th}}(p,\theta)$ and $E_{\mathrm{mean}}(p,\theta)$ are determined from single track response evaluated by a Monte Carlo simulation. The calorimeter clusters which are not associated with any charged track are treated as neutral clusters.

The above procedure is repeated to all charged tracks and results in the revised energy flow particles (tracks and neutral clusters). Figure 3.5 (A) shows the distribution of the total energy for the well contained hadronic events taken at the Z^0 peak in 1994. The gaussian fit gives the energy resolution of σ_{E} =9.5 GeV. The angular resolutions in r–ϕ and r–z directions are obtained from the back-to-back two-jet samples at the Z^0 peak. Figure 3.5 (B) and (C) show the distributions of angles, $\Delta\phi$ and $\Delta\theta$ defined by $180^\circ - \phi_{jj}$ and $180^\circ - \theta_{jj}$, where ϕ_{jj} and θ_{jj} are the opening angle of two jets in r–ϕ and r–z plane, respectively. To see the resolution for single jet, the angles are divided by $\sqrt{2}$ in the plot. The angular resolutions are measured to be 23 mrad for both θ and ϕ.

3.4.3 Hadronic Event Selection

The hadronic event selection used in this analysis is so-called "Tokyo multihadronic event selection", one of the standard hadronic event selections used in OPAL.

The selection is based on the electromagnetic clusters and the charged track multiplicity. An electromagnetic cluster is required to satisfy the same criteria as given in section 3.4.1. Each track should have at least 20 space points measured by the central tracking detector. The distance of closest approach to the beam axis, $|d_0|$, should be less than 2 cm, and the z coordinate of the point of closes approach, z_0, should satisfy $|z_0| <40$ cm. The momentum component transverse to the beam axis, p_{xy}, must exceed 50 MeV/c.

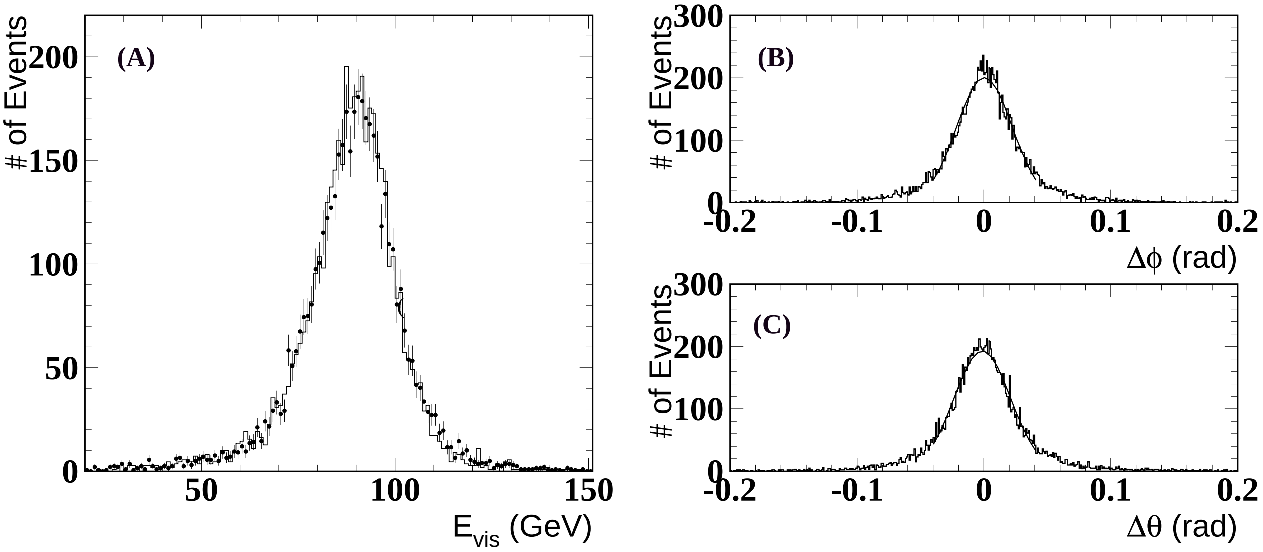

Figure 3.5: (A) Distribution of the total energy for the well contained hadronic events taken at Z^0 peak in 1994. The angular resolutions of the jet in (B) for the azimuthal angle and in (C) for the polar angle.

Events are selected if they satisfy all of the following conditions.

- The event contains at least 7 clusters.
- The event contains at least 5 charged tracks.
- The ratio of the total visible energy observed in electromagnetic calorimeter, $\sum E_{\text{clus}}$, to the center-of-mass energy, $\sqrt{s}$, satisfies

$$R_{\text{vis}}^{\text{em}} \equiv \frac{\sum E_{\text{clus}}}{\sqrt{s}} > 0.1.$$

- The energy balance along the beam direction satisfies

$$R_{\text{bal}} \equiv \frac{|\sum E_{\text{clus}} \cos\theta_{\text{clus}}|}{\sum E_{\text{clus}}} < 0.65,$$

  where θ_{clus} is the polar angle of each cluster.

3.4.4 Jet Findings

The energy flow particles are grouped into a desired number of jets according to the search topologies. There are several standard jet finding algorithms commonly used in high energy physics analyses. The algorithm mainly used in this analysis is the Durham (k_t) [31] algorithm.

For each pair of the energy flow particles, the jet resolution parameter,

$$y_{ij} = \frac{2\min(E_i^2, E_j^2)(1-\cos\theta_{ij})}{E_{\text{sum}}}, \tag{3.1}$$

is calculated, where E_i and E_j are the energies of the energy flow particles, θ_{ij} is the opening angle between i-the and j-th energy flow particles, and E_{sum} is the total energy sum.

Of all the possible combinations, the pair with the smallest jet resolution parameter is replaced by a pseudo particle with an energy

$$E_{ij} = E_i + E_j, \tag{3.2}$$

and a three momentum

$$\vec{p}_{ij} = \frac{E_{ij}}{|\vec{p}_i + \vec{p}_j|}(\vec{p}_i + \vec{p}_j), \tag{3.3}$$

where $\vec{p}_i$ and $\vec{p}_j$ are the three momenta of the particles. This procedure is repeated until all the pairs have the jet resolution parameter exceeding the threshold y_{cut}, or the desired number of jets are reconstructed.

3.4.5 Lepton Identification

Lepton identification is very important for the Higgs search and is used

- in the electron and muon channels,
- in b flavour tagging, and
- in the tau channels.

In the electron and muon channels, the leptons are expected to have a very high momentum because the leptons directly originate from the Z^0 decay. The identification optimized to high momentum leptons is therefore treated as a separate issue and described in section 3.5.

In the b flavour tagging, the electron and muon identification is used to tag leptons from the leptonic decay of b hadrons. In the tau channels, the electron and muon identifications are used to identify leptonic decay of the tau. The description of overall tau lepton identification can be found in section 3.8. The following paragraphs describe the electron [32] and muon [33] identifications used in the b flavour tagging and the tau chnnels.

Electron Identification The electron identification is usually performed using two parameters, i.e. the ionization loss dE/dx and the energy of the electromagnetic cluster (E) divided by the momentum of the track (p) associated with the cluster, E/p. For electron tracks, dE/dx is expected to be about 10 keV/cm for $p >$ 2.0 GeV/c and E/p is about unity.

In this method, electrons were identified using *artificial neural network* technique. This neural network consists of an input layer with 12 input nodes, a hidden layer with 15 nodes, and an output layer with an output node. Input parameters are as follows:

(1) the momentum of the track,

(2) the $\cos\theta$ of the track,

(3) the dE/dx of the track measured by the jet chamber,

(4) the expected error of dE/dx measurement,

(5) the ratio E/p,

(6) the number of lead-glass blocks in the electromagnetic cluster,

(7) the E_{cone}/p,

(8) the number of blocks in the electromagnetic cluster where E_{cone} is defined,

(9) the ratio $E_{\mathrm{cone}}/E_{\mathrm{cone2}}$,

(10) the distance between the electromagnetic cluster and the track in ϕ direction,

(11) the distance between the electromagnetic cluster and the track in θ direction, and

(12) the multiplicity of presampler hits in front of electromagnetic calorimeters,

where E is the electromagnetic energy associated to the charged track, and E_{cone} is the total energy within the cone with a half angle of 30 mrad around the track extrapolated to the cluster. The parameter E_{cone2} is the energy defined as $E_{\mathrm{cone2}} = E - E_{\mathrm{cone}}$. The neural network was trained by the Monte Carlo samples to output 1 for electron and 0 for other particles. Figure 3.6 (A) shows the distribution of the neural network output.

Muon Identification Muon identification is based on the penetration of a muon track through the hadron calorimeter which has a large material as an absorber for all region of the solid angle. A charged track measured in the central tracker is extrapolated to the outer detectors. The muon segment associated with this extrapolated track is looked for and the matching parameter between the track and the muon segment is examined. This matching parameter is defined as

$$\chi = \sqrt{\left(\frac{\Delta\phi}{\sigma_\phi}\right)^2 + \left(\frac{\Delta\theta}{\sigma_\theta}\right)^2},$$

where $\Delta\phi$ and $\Delta\theta$ are the differences between the extrapolated track and the muon segment in the ϕ and θ directions respectively, and σ_ϕ and σ_θ are their errors. The distribution of this variable χ is shown in Figure 3.6 (B). This variable was required to be less than 3.0 for muon candidates. If there were more than one extrapolated muon tracks associated with one muon segment, the charged track with the smallest distance to the muon segment is considered as the candidate of the muon track for this segment. On the other hand, if there are more than one muon segments associated with one extrapolated charged track, the segment with the smallest χ is considered as the candidate of the segment for this track.

3.4.6 B tagging

Since the branching fraction of the Higgs boson to the b quark pair is more than 80 % for the Higgs boson mass relevant in the LEP2 energies, an efficient and high purity b tagging provides a good signal and background seperation in the Higgs search, especially in the four jets and the missing energy channels. Because the main background events in these channels come from the W pair production which have no b flavour in the final state. Background events from the Z^0Z^0 process can also be reduced by requiring the b flavour in its final state because the branching fraction to the b quark pair is lower (~15%) than that of Higgs boson.

There are three types of methods for tagging the b flavor. The first type is based on the lifetime information. This type can be further divided into two methods, namely secondary vertex tag and impact parameter tag. The secondary vertex tag tries to reconstruct the decay vertex explicitly. An

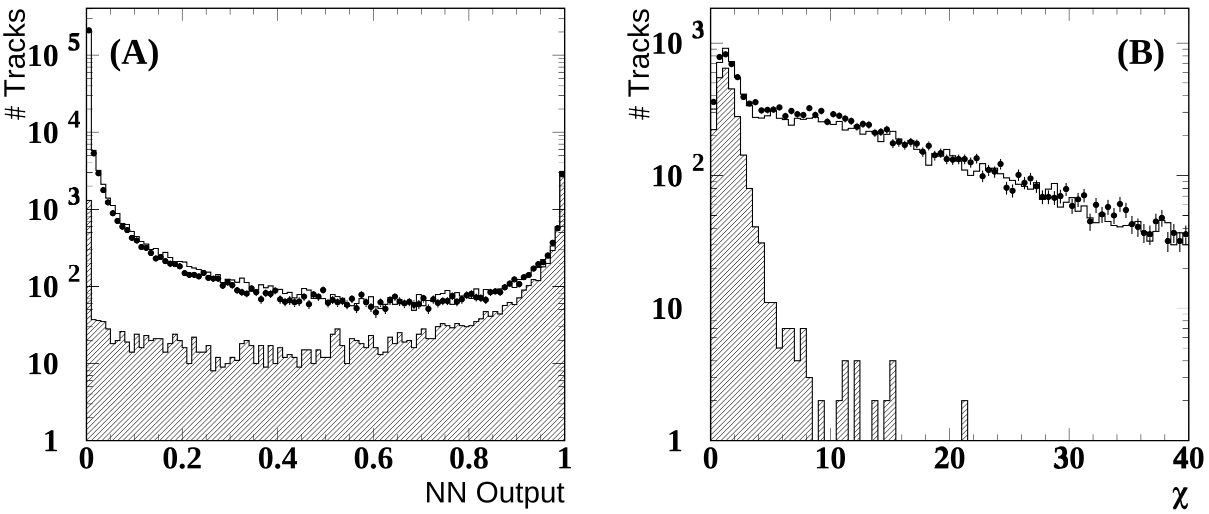

Figure 3.6: *(A) Neural network output distributions for electron identification. Points with error bars are for the hadronic events taken at the calibration runs. Hatched (Open) histogram shows the expected distribution of electron (other particles) tracks. Tracks having momentum higher than 2 GeV are plotted. (B) Distribution of the matching parameter,* χ*. Hatched histogram shows the expected distribution for the muon tracks. Tracks having momentum higher than 3 GeV are plotted.*

event, or a jet of an event, is tagged when a decay vertex is found and is significantly displaced from the primary vertex. On the other hand, the impact parameter tag uses the distribution of the impact parameters of the tracks in each event. The distribution is usually transformed to one variable which efficiently discriminates the b flavor from the other flavors. An example of such a variable is the forward multiplicity, which was first used by MARK-II in the reference [34]. A more elaborate technique, using a product of likelihoods for all tracks produced at the primary vertex, was recently used by ALEPH [35].

The second type of methods tries to tag the lepton from the semileptonic decay of the b hadron. The lepton from the b hadron tends to have a high transverse momentum with respect to the quark direction because of the heavy b quark mass.

The third type of methods uses the heaviness of the b hadron. Distributions of kinematic variables, such as boosted sphericity, or rapidity, are usually combined to emphasize the difference between flavors. An example of the usage of this type can be found in the reference [36], in which 21 kinematic variables are combined by an artificial neural network.

In this study, the secondary vertex tag, the impact parameter tag, and the lepton tag are used. The secondary vertex fiding algorithms described in the following paragraphs are the 3-dementional extension of the methods used in the references [37] and [38].

Primary Vertex Finding Before reconstructing secondary vertices or measuring impact parameters, one has to know the position of the primary vertex. The position of the primary vertex is determined event-by-event, by fitting the measured trajectory of the tracks in each event to a common point in three-dimension. The knowledge of the position and the size of the beam spot is used as an additional constraint to the fit. The primary vertex finding proceeds as follows. First, all the tracks in the event are considered to have been produced at the primary vertex. Loose quality cuts, $|d_0| < 2$ cm and $|z_0| < 200$ cm are applied to the tracks. Two imaginary tracks running through the center of the average beam spot in the x and y directions, with errors corresponding to the beam spread, are added to constrain the primary vertex in the beam spot. The tracks, including two imaginary ones, are fitted to a common vertex in three dimension. If any track contributes to the overall χ^2 by more than 4, the track with the largest χ^2 contribution is removed and the fit is repeated. The primary vertex finding succeeds if more than two real tracks remain after the iteration. Figure 3.7 shows distributions of reconstucted position of the primary vertices with respect to the nominal beam collision point.

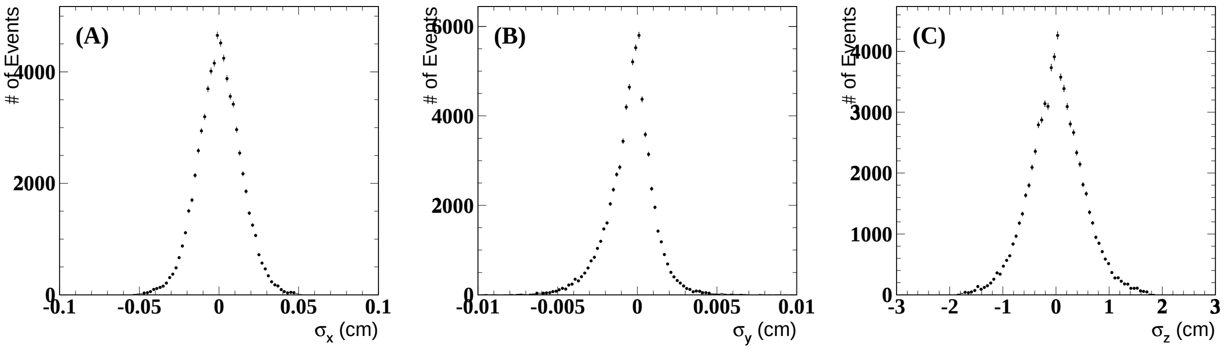

Figure 3.7: *Distributions of reconstructed primary vertex position with respect to the nominal beam collision point in (A) x, (B) y, and (C) z direction.*

Secondary Vertex Finding with Tear Down Algorithm The "tear down" algorithm [37] is in principle the same as the algorithm used in the primary vertex finding. At first, all the tracks in the jet are fitted to a common vertex point. If one or more tracks contribute to the χ^2 by more than 4, the track with the largest contribution is removed and the fit is repeated. The procedure converges when all the remaining tracks contribute less than 4 to the overall χ^2, or an insufficient number of tracks remain. Additional cuts are applied to the input tracks. The tracks must have the impact parameter error smaller than 0.1 cm, and the impact parameter should be smaller than 3 mm in r–ϕ. The former cut removes poorly measured tracks, and the latter the tracks from decays of long-lived particles such as K^0 and Λ. When the secondary vertex is successfully found, the decay length $|L|$ is defined as the distance between the primary and the secondary vertices projected onto the direction of the total momentum of the tracks assigned to the secondary vertex. The sign of the decay length is also defined using the total vertex momentum: $L > 0$ if the secondary vertex is displaced from the primary vertex in the same direction as the vertex momentum, and $L < 0$ otherwise. The significance of the decay length L/σ_L is defined as the decay length divided by the measurement error. The distributions of the decay length significance obtained by the tear down algorithm for the calibration data taken at Z^0 pole and Monte Carlo events are shown in Figure 3.8 (A).

Secondary Vertex Finding with Build Up Algorithm Contrary to the tear down vertexing, the "build up" algorithm [38] tries to reconstruct the secondary vertices from the tracks with large impact parameters. At first, three tracks with the largest impact parameter significances, defined as b/σ_b, are considered as seed tracks. The intersections of all pairs of the seed tracks in the jet are taken as seed vertices. The other tracks in the jet are then fitted, one by one, to a seed vertex. The combination with the smallest χ^2 is retained. This process of adding tracks is repeated until the χ^2 probability becomes smaller than 1 %. This procedure is applied to all the seed vertices. The decay length is calculated in the same way as the tear down vertexing. If several vertices are found in single jet, the vertex with the largest number of assigned tracks is retained. If still ambiguous, the vertex with the most significant separation from the primary vertex is chosen. The distributions of the decay length significance obtained by the build up algorithm for the calibration data taken at the Z^0 pole and the Monte Carlo events are shown in Figure 3.8 (B).

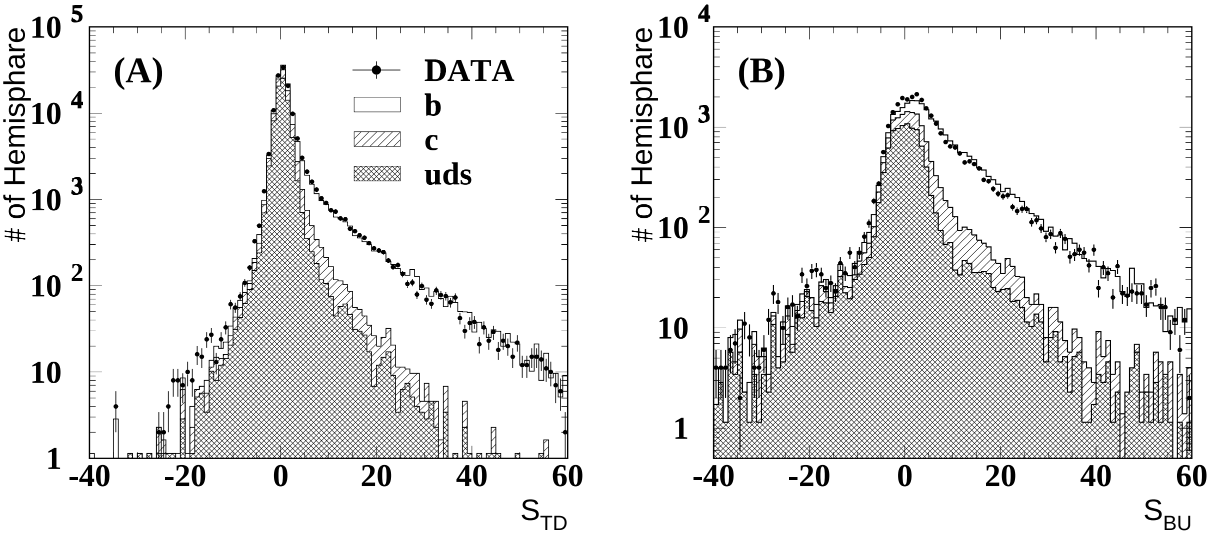

Figure 3.8: *Distribution of decay length significance obtained by (A) the tear down and (B) the build up algorithms. Points with error bars correspond to the calibration runs taken at the Z^0 pole. Histograms are distributions expected by the Monte Carlo events. Open, single hatched, and double hatched histograms are for the b, c, and uds flavour jets.*

Forward Multiplicity The forward multiplicity of the jet is determined by counting the number of tracks having impact parameter significance larger than a certain cut value $S_{\rm min}$. In this analysis $S_{\rm min}$ is set to 2.5. Supplemental track quality requirements are applied in order to reject badly measured tracks and tracks which have wrong association to the silicon micro vertex detector hits, which tend to have large impact parameter significance. Tracks are required to have their impact parameters smaller than 0.3 cm, and expected measurement error of the impact parameters less than 0.1 cm in 3-dimention. Figure 3.9 (A) shows the forward multiplicity distribution.

Lepton Tagging Electrons and muons in a jet are identified using the methods described in 3.4.5. For the tagged leptons, transverse momenta, p_t, are calculated with respect to the jet axis containing the lepton. Figure 3.9 (B) shows the distribution of momentum of the highest p_t lepton in the jet, in which at least one lepton is identified.

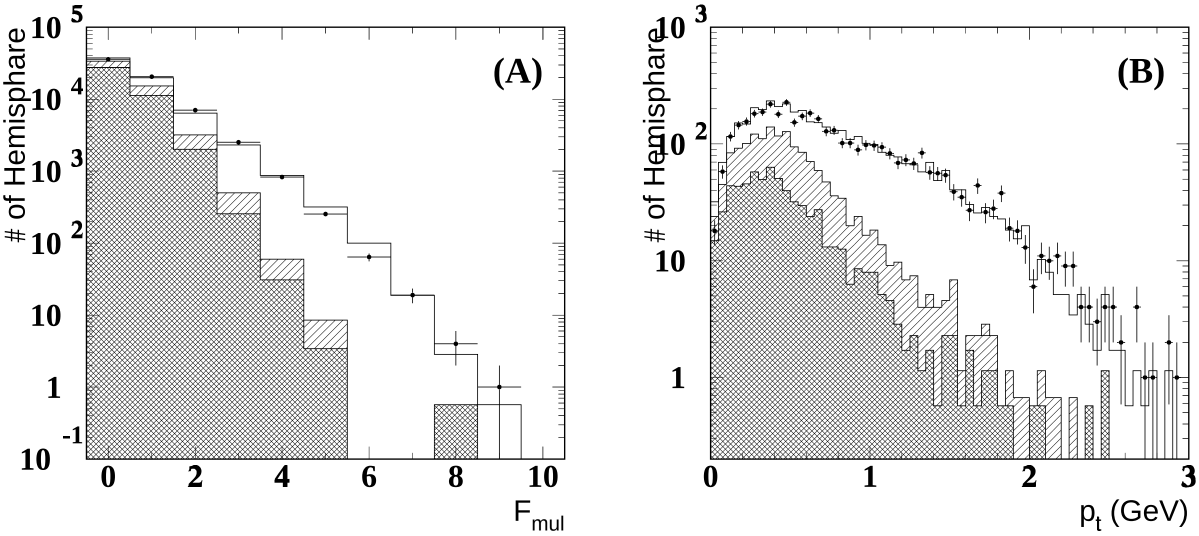

Figure 3.9: *(A): Forward multiplicity distribution. (B): Distribution of transverse momentum with respect to the nearest jet. The conventions of figures are the same as Figure 3.8 .*

3.4.7 Kinematic Fit

The simplest way to reconstruct the mass of a particle is to calculate the invariant mass of the two jets. However, the mass resolution of this naive invariant mass method is poor. The mass resolution can be improved by imposing the energy–momentum conservation in the mass reconstruction procedure. Kinematic fit is introduced to include these constraints in the mass reconstruction. The observed quantities are modified within the error of these quantities to minimize a χ^2 constructed with these variables. The minimization of the χ^2 is performed by iterative procedure imposing the constraints by Lagrange multipliers. For the jets the inputs are one scalar momentum and two directions.

Under the Z^0H^0 event hypothesis, an additional constraint can be added that one of the reconstructed mass should be the mass of Z^0. There is another constraint that the two reconstructed masses are the same in the W^+W^- hypothesis. Figure 3.10 (A) shows the reconstructed mass distributions before and after the kinematic fit for the Higgs boson Monte Carlo sample of m_{H^0} =65 GeV. Significant improvement can be seen in the figure.

3.4.8 Effective Center-of-mass Energy

Since multihadronic events are often produced as the "radiative return" to the Z^0, it is useful to know the effective center-of-mass energy, $\sqrt{s'}$, excluding the initial state photon. The effective center-of-mass energy is calculated from the measured energy of isolated photon, E_γ, by the following formula;

$$\sqrt{s'} = \sqrt{s - 2E_\gamma\sqrt{s}}.$$

If any isolated photon is not found in the event, the energy of the photon is obtained by performing a kinematic fit to a system of jets and an unmeasured photon along the beam direction, imposing constraints of the energy–momentum conservation. Figure 3.10 (B) shows the $\sqrt{s'}$ distribution of the multilihadronic events collected at $\sqrt{s}$ =161 GeV together with the Monte Carlo expectation.

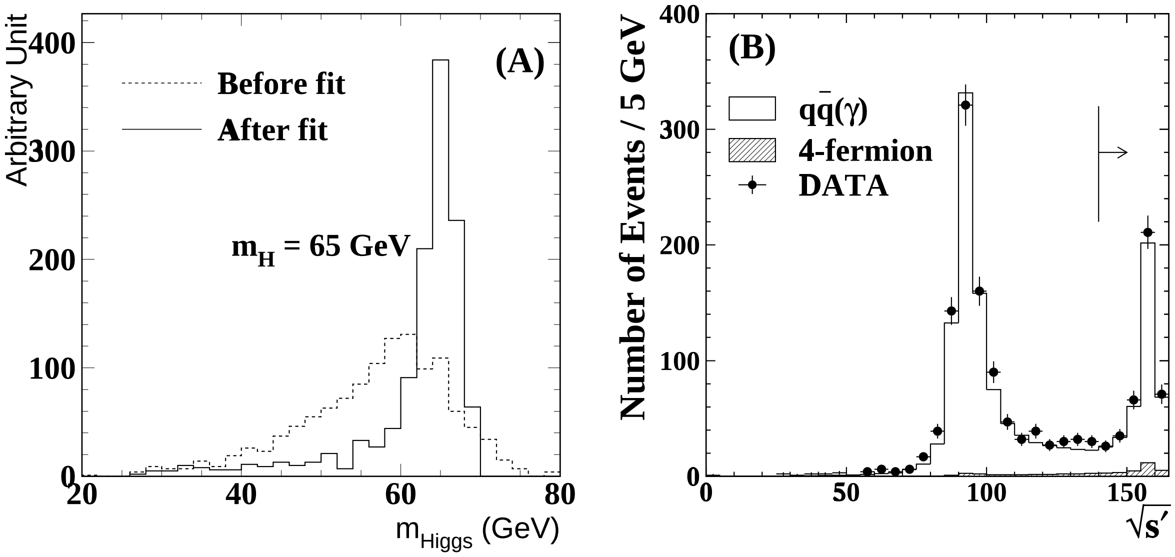

Figure 3.10: *(A): The effect of kinematic fit. Solid (dashed) histogram shows the reconstructed mass distribution of the signal Monte Carlo sample of 65 GeV Higgs mass after (before) the kinematic fit. (B): Effective center-of-mass energy distribution of hadronic events. Points with error bars show the data taken at 161 GeV. Open (hatched) histogram shows the expected distribution for multihadronic (four-fermion) events.*

3.5 The Electron and Muon Channels

The electron and muon channels arise when the Z^0 decays to a pair of electrons or muons. Although these channels together have the smallest branching fraction of about 6.7%, these channels have very clean event signatures. Hence a good background reduction is expected. The final states of these channels are characterized by:

- no missing energy,
- presence of a pair of energetic, isolated, and oppositely charged leptons with same species,
- the invariant mass of the lepton pair consistent with the Z^0 mass, and
- a clean four jet structure which consists of the two leptons and two hadronic jets.

The possible background sources of these channels are high multiplicity events without missing energy, namely multihadronic events and four-fermion events.

The multihadronic events, $e^+e^- \to q\bar{q}$, can fake the signal when the events contain two fake leptons or when the events contain heavy flavour quarks (b or c) which decays semileptonically. These events can be reduced by requiring the lepton isolation because the fake leptons tend to be close to the jet activities. The hadronic W-pair production process, $e^+e^- \to W^+W^- \to q\bar{q}q\bar{q}$, has a large cross-section. These events can be effectively suppressed by requiring two energetic leptons. Since a semileptonic W-pair events, $e^+e^- \to W^+W^- \to \ell\nu q\bar{q}$, has a real lepton in its final state, the lepton tagging is less effective to remove them. But this type of event can be suppressed by requiring high visible energy and by requiring the lepton isolation. Since leptons don't make a mass peak in the events from the above three background sources, the invariant mass distribution is expected to be flat. Requiring the lepton pair invariant mass be consistent with m_{Z^0} effectively rejects these background events. The process $e^+e^- \to Z^0 + Z^0/Z^{0*}/\gamma$ where the Z^0 decays to a lepton pair has the same event structure as the signal events. Fortunately the cross-section of this type of events is small (~ 0.05 pb) under the threshold of the pair production of the real Z^0Z^0, $\sqrt{s} < 2m_{Z^0}$ if one requires the mass of hadronic systems to be in the search region of m_{H^0}. The events from $Z^0\gamma^*$ can be removed by requiring large opening angle between the two hadronic jets. In the electron channel, the process $e^+e^- \to Z^0e^+e^-$ can also be the background. Since the electron pair of this process doesn't have mass peak and the electrons tend to escape to the beam pipe, this process is not very serious.

The event selection proceeds as follows. First the events without missing energy and having a four jet structure are selected. A pair of energetic leptons are then tagged in the selected events. Finally the invariant mass of the lepton pair is required to have a mass consistent with that of Z^0.

The criteria are optimized to select the signal events where the Higgs decays hadronically, because the contribution of the tau decay process is about 6 % to those channels. However, as the requirement to the hadronic system is very loose, some sensitivity is also expected to the tau case.

3.5.1 Preselection

A preselection is designed to select high multiplicity events with four-jet like structure and without missing energy. The preselection rejects most of the two-photon events and the lepton-pair events. The cuts for the preselection are listed in the following.

(P1) There should be at least six good charged tracks.

(P2) The total visible energy normalized by the center-of-mass energy, $R_{\rm vis}$, and the total visible momentum in z direction, $p^z_{\rm tot}$, should satisfy the following conditions.

$$|p^z_{\rm tot}| \le 100 \cdot (R_{\rm vis} - 0.4) \text{ and } R_{\rm vis} \ge 0.6 \qquad \text{at 161 GeV}$$

$$|p^z_{\rm tot}| \le E_{\rm cm} \cdot (R_{\rm vis} - 0.5) \text{ and } R_{\rm vis} \ge 0.6 \qquad \text{at 172 GeV}$$

The first cut eliminates radiative return events in which photon goes away to the beam direction. The second cut rejects most of the two-photon events and some of $W^+W^- \to \ell\nu q\bar{q}$ events. The distributions of the $p^z_{\rm tot}$ and $R_{\rm vis}$ are shown in Figures 3.11 (A)-(D).

(P3) The event is reconstructed as a four jet final state with the Durham algorithm. The jet reconstruction parameter for the four jet final state, y_{34}, is required to be larger than 0.001. This cut suppresses non-radiative $q\bar{q}$ events and radiative $q\bar{q}$ events in which photon from the initial state radiation is detected. The distribution of $\log_{10} y_{34}$ is shown in Figure 3.11 (E).

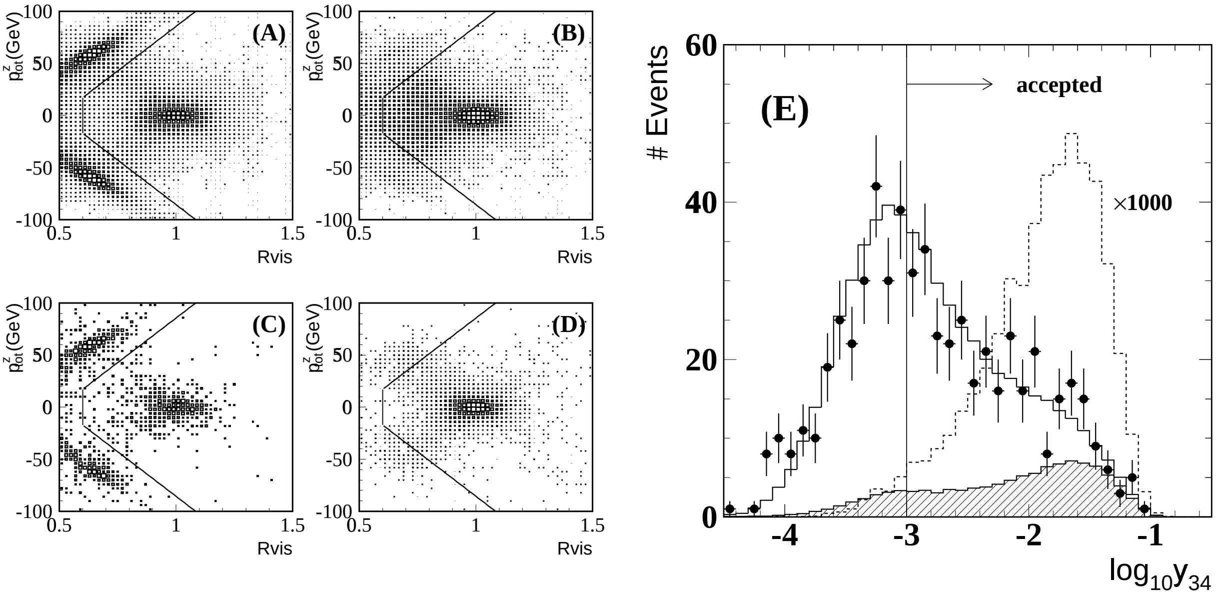

Figure 3.11: *(A)–(D): Scatter plots of $p^z_{\rm tot}$ and $R_{\rm vis}$ for (A) $q\bar{q}$ events, (B) four-fermion events, (C) real data, and (D) expected signal events after cut (P1). All plots are for 172 GeV data. (E): Jet resolution parameter, y_{34}, distributions after cut (P2). Points with error bars are for the data. Open (hatched) histogram shows the expected distribution for $q\bar{q}$ (four-fermion) background events. The expected distribution for the Higgs signal is shown with dotted histogram. The sigal distribution is scaled up by 1000 for visibility.*

The above preselection retains about 94 (88) % of the signal events in which the Higgs decays hadronically for electron (muon) channel, while most of the two-photon and the lepton pair events are eliminated. The difference of the efficiencies between the electron and muon channels comes from the difference of the detector acceptance of the calorimetry and the tracking devices. The signal events eliminated in the preselection include events with one (two) lepton(s) which is not detected or with a jet which goes to the forward region. The remaining background events are dominantly four-fermion events and $q\bar{q}(\gamma)$ events.

3.5.2 Lepton Pair Selection

The events are further required to contain at least one pair of oppositely charged leptons with same species tagged by the methods described in the following paragraphs.

Electron Pair Tagging at 161 GeV As the two electrons coming from the Z^0 decay shoul be energetic, the two highest-energy electromagnetic calorimeter clusters are considered as electron candidates. The nearest track to each cluster in θ–ϕ space is associated to the cluster.

The following criteria are applied to the events with the electron candidates.

- The two associated tracks should have opposite charges.
- The momentum of the associated track has to be greater than 5 GeV.

- One of the background sources is the conversion of high energy photons. The e^+e^- pair converted from a high energy photon is sometimes reconstructed as a single track. The dE/dx of such a track is two times higher than that of an ordinary electron track. Therefore the dE/dx of the associated track measured in the central detector is required to be at most 15 keV/cm. The distribution of the dE/dx is shown in Figure 3.12 (A). A peak around dE/dx =20 keV/cm corresponds to the conversion tracks.
- The lateral spread of cascade shower in the calorimeter is expected to be small for electrons. The number of blocks which contains 90% of the cluster energy, N_{90}, should not exceed 7.
- The cluster energy divided by the momentum of the associated track, E/p, should be within the region $0.6 < E/p < 4$. At least one electron candidate should satisfy $E/p < 1.5$. The E/p distributions are shown in Figure 3.12 (B)-(E).

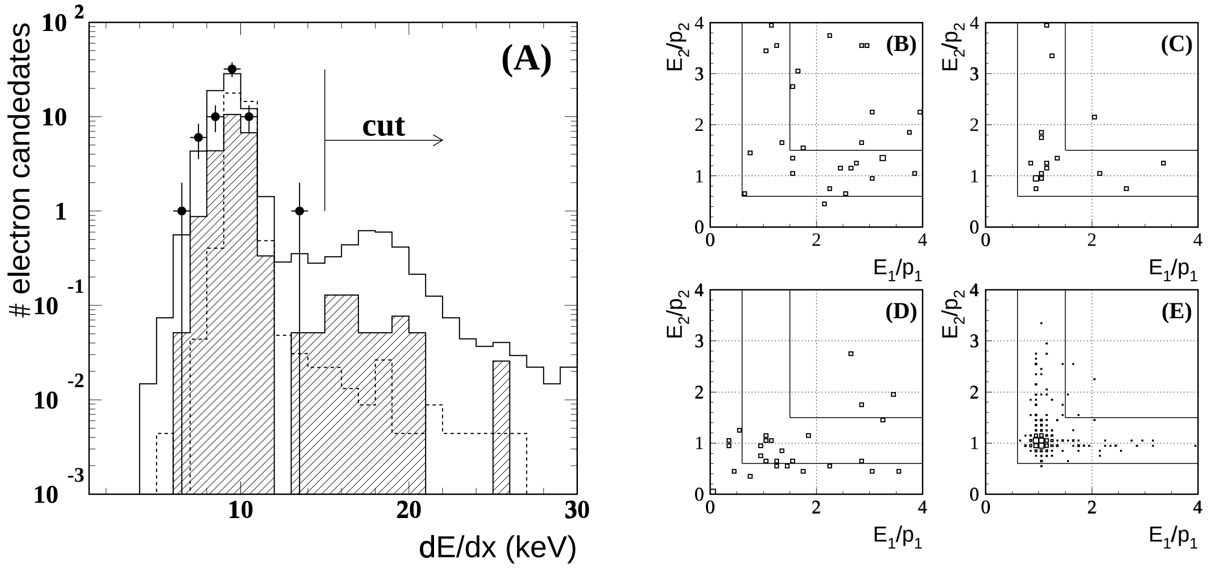

Figure 3.12: *(A): The dE/dx distributions for the data (points), Monte Carlo $q\bar{q}$ events (open histogram) and four-fermion events (hatched histogram). All simulated distributions are normalized to the luminosity of the data. Dotted lines show the distributions for the expected signal events of m_{H^0} =65 GeV scaled up by a factor of 100. (B)–(E): E/p distribtuions for (B) $q\bar{q}$, (C) four-fermion, (D) data, and (E) expected signal events. The electron candidates in the preselected events, which satisfy all the electron identification requirements except the plotted variable, are plotted.*

Electron Tagging at 172 GeV The electron tagging used for the 161 GeV analysis is modified in order to increase the efficiency at 172 GeV. At 161 GeV only the two highest clusters are considered as the electron candidate clusters. The association of the track is also limited to the nearest one even if another track has more electron-like properties. At the 172 GeV analysis, every cluster satisfying the following criteria is considered as an electron candidate cluster.

- The energy of the cluster has to be higher than 5 GeV.

- The N_{90} of the cluster should satisfy the following condition;

$$N_{90} < 5 \text{ if } |\cos\theta| < 0.75$$

$$N_{90} < 6 \text{ if } |\cos\theta| > 0.75,$$

where θ is the polar angle of the candidate cluster.

The different cut values of N_{90} reflects the different amount of material in front of the calorimeter and the fact that the barrel calorimeter has a pointing geometry while the endcaps have a coaxial geometry. Figures 3.13 (A) and (B) show the scatter plots of N_{90} versus $|\cos\theta|$ for then clusters of electrons and other particles obtained from the Monte Carlo signal and $q\bar{q}$ event samples, respectively.

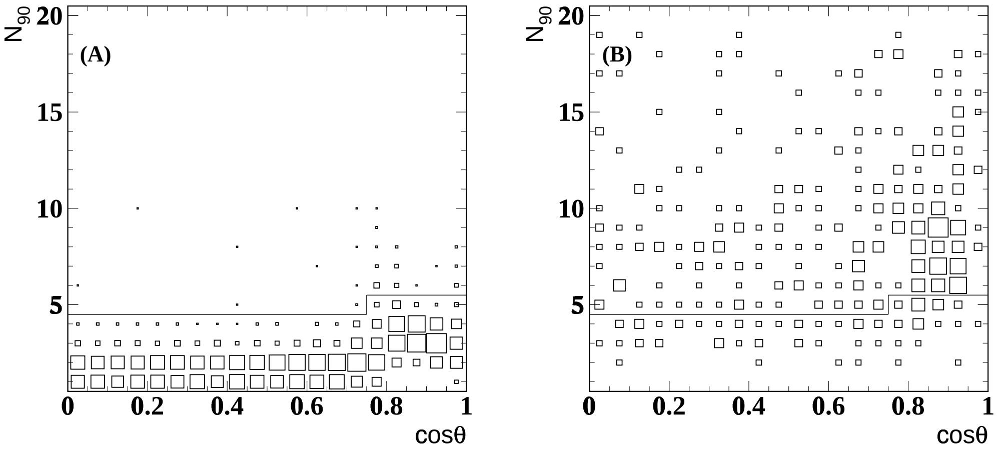

Figure 3.13: *Satter plots of N_{90} versus $|\cos\theta|$ for (A) electrons in the signal Monte Carlo samples and (B) other particles in the $q\bar{q}$ Monte Carlo sample. Lines in the plots show the cut positions.*

The tracks around the clusters are then examined to form a track-cluster pair by the following criteria.

- The distance between the cluster center and the extrapolated intersection of the track should be smaller than 100 mrad in both θ and ϕ directions.
- The momentum of the track should be higher than 2 GeV.
- The normalized E/p, E/p_{norm}, is larger than -6. The value E/p_{norm} is defined as

$$E/p_{\text{norm}} = \frac{1 - E/p}{\sigma_{E/p}},$$

where $\sigma_{E/p}$ is the expected error of E/p calculated from the expected errors of the energy and momentum measurements.

The reason why E/p_{norm} is used instead of E/p is that the ratio E/p has large measurement error in the overlap region of the barrel and the endcaps and in the forward regions. In the overlap region, the energy resolution of cluster is degraded due to a large amount of material in front of the calorimeter. The track momentum is badly measured in the forward region, where the number of measurement points in the central tracker is limited. Figures 3.14 (A)–(C) show the expected errors of the energy, momentum, and E/p measurements as a function of $|\cos\theta|$ for the Bhabha scattering events taken in the calibration runs. Figures 3.14 (D) and (E) show the distributions of the E/p_{norm} for electrons and other particles obtained from the Monte Carlo samples. The distribution for electrons has a peak at zero while the E/p_{norm} of the other particles is distributed in the higher value. Removing simply high E/p_{norm} events not only effectively reduces background tracks, but also rejects a non-negligible amount of real electrons. A tight cut of E/p_{norm} is therefore applied by a pair-wise manner as described later.

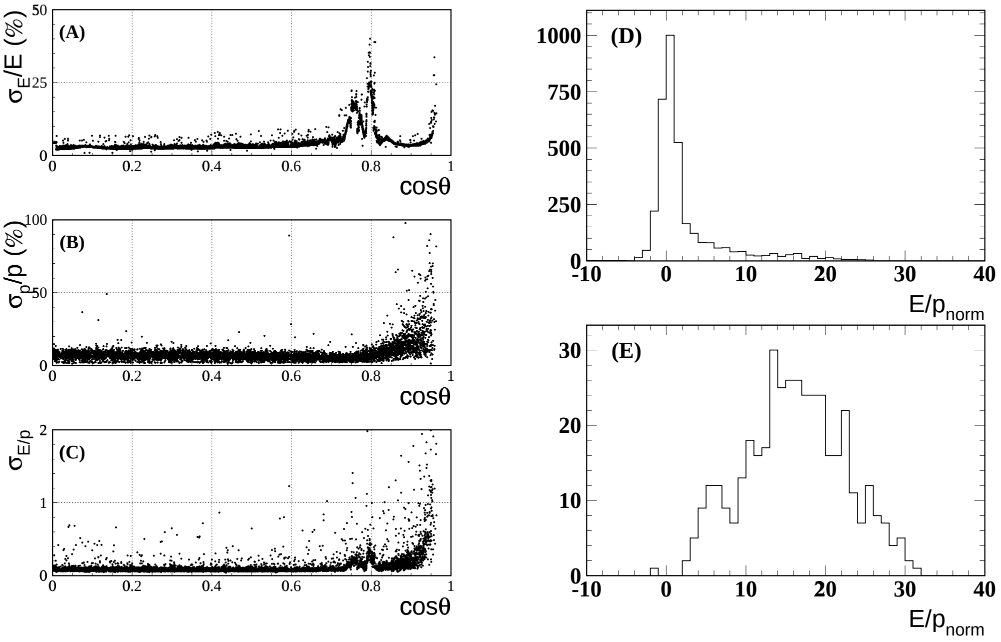

Figure 3.14: *(A)–(C): Distributions of expected error of (A) cluster energy, (B) track momentum, and (C) E/p as a function of $|\cos\theta|$. (D)–(E): Distributions of the E/p_{norm} for (D) electrons in the Higgs signal samples and for (E) other particles in the $q\bar{q}$ Monte Carlo samples.*

If there are more than one track satisfying these criteria, the track with the smallest ϕ difference is selected.

Since electrons often radiate photons and/or start to make showers in the detector material in front of the electromagnetic calorimeter, the energy of an electron is sometimes deposited in more than one cluster. This deteriorates the resolution of the electron pair invariant mass. An attempt is made to merge "satellite" clusters around the candidate cluster to the electron candidate clusters. Figures 3.15 (A) and (B) show the distribution of the opening angle between electron track and the satellite cluster and the distribution of the energy of the satellite clusters in the Bhabha events taken at 91 GeV runs. A cluster is merged to an electron candidate cluster if the cluster satisfies the following conditions.

- The angle between the cluster and the electron candidate track should be smaller than 10° in 3-dimension.
- There should be no other track within a 20° half-angle cone around the electron candidate track.
- The cluster should be in the region $|\cos\theta| \leq 0.85$ to ensure the isolation of the electron.

The effect of merging satellite clusters to the mass resolution is shown in Figures 3.15 (C) and (D).

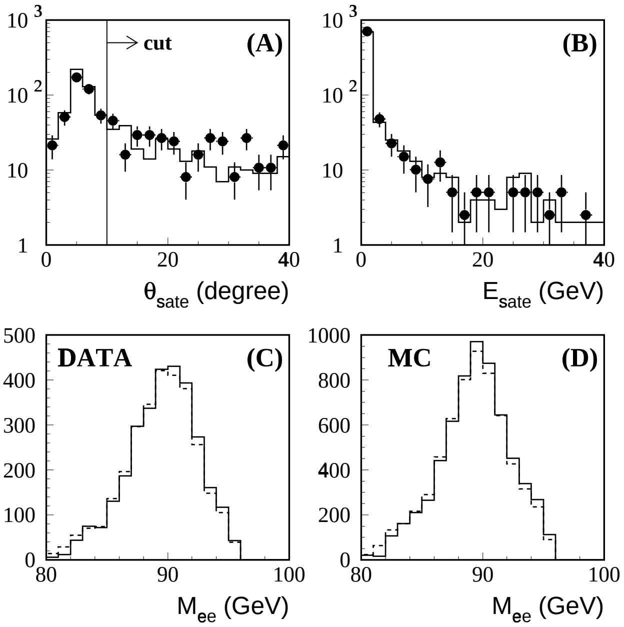

Figure 3.15: *Distributions of (A) angle between satellite cluster center and the electron track and (B) energy of satellite cluster. Histograms (points with error bars) are for Bhabha Monte Carlo events (Low multiplicity event taken at the* Z^0 *pole in 1994). Distributions of the invariant mass of the two electrons for (C) the data and (D) the Monte Carlo samples before (dashed lines) and after (solid lines) merging the satellite clusters.*

Finally two track-cluster pairs are chosen by the following criteria.

- The two tracks have opposite charges.
- The pair has an invariant mass closest to the Z^0 mass.

To further reduce misidentification of electron pairs, at least one electron candidate is required to have E/p_{norm} satisfying the condition

$$-2.5 < E/p_{\mathrm{norm}} < 5.$$

The distributions of the E/p_{norm} of two electrons together with the selected regions are shown in Figure 3.16.

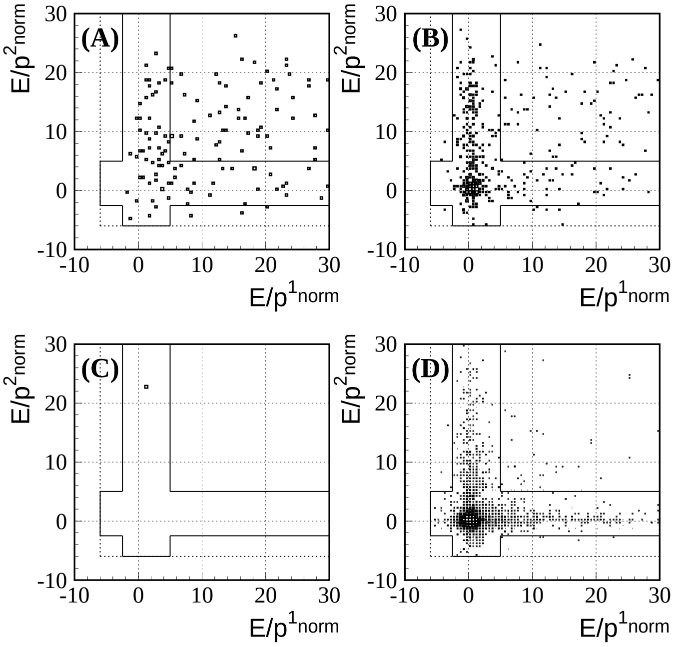

Figure 3.16: *Distributions of $E/p_{\rm norm}$ values of the two track-cluster pairs for (A) $q\bar{q}(\gamma)$, (B) four-fermion, (C) data and (D) signal events. Solid lines show the cut positions.*

Muon Pair Tagging The muon tagging method used here is based on the scheme used in the LEP1 lineshape analyses [39]. A charged track is identified as a muon if it satisfies either of the following conditions.

- At least two muon chamber hits are associated with the track within $\Delta\phi = (100 + 100/p)$ mrad, with the momentum p in GeV.
- At least four hadron calorimeter strips are associated with the track within $\Delta\phi = (20 + 100/p)$ mrad, with p in GeV. The average number of strips in layers containing hits has to be less than 2 to discriminate against hadrons. For $|\cos\theta| < 0.65$, where tracks traverse all 9 layers of strips in the barrel calorimeter, a hit in one of the last 3 layers of strips is required.
- The track has momentum $p > 15$ GeV and the electromagnetic energy associated to the track within $\Delta\phi < 70$ mrad is less than 3 GeV.

The pair of oppositely charged muon candidates with its invariant mass nearest to the Z^0 mass is selected as the muon pair candidate.

3.5.3 Main Selection

(1) Both leptons of the candidate pair must have an energy larger than 25 (20) GeV with at least one of them larger than 35 (30) GeV at 161 (172) GeV. The scatter plots of the energies of the

two lepton candidates are shown in Figure 3.17.

(2) The rest of the event excluding the candidate lepton pair is reconstructed as two jets using the Durham algorithm. Fake leptons from $q\bar{q}(\gamma)$ or $W^+W^- \to \ell\nu q\bar{q}$ events tend to be near the jet activities. Lepton isolation is ensured by requiring that each lepton has a transverse momentum, p_t, calculated with respect to the nearest jet axis, larger than 10 GeV. Figure 3.18 shows the p_t distributions after cut (1). This cut effectively eliminates the $q\bar{q}$ events and $W^+W^- \to \ell\nu q\bar{q}$ events.

(3) The selected events must have a lepton pair with an invariant mass consistent with the Z^0 boson mass. For electrons the invariant mass of the lepton pair must lie between 75 GeV and 105 GeV, while for muons it must lie between 60 GeV and 120 GeV. The different mass windows take into account the different resolutions for electrons and muons. Figures 3.19 (A) and (B) show the distributions of the lepton pair invariant mass for the electron and the muon channels, respectively.

(4) In order to suppress $e^+e^- \to Z^0Z^{0*}/\gamma^*$ background events, the opening angle of the jet pair is required to be larger than 50°. Figures 3.19 (C) and (D) show the distributions of opening angle after cut(3).

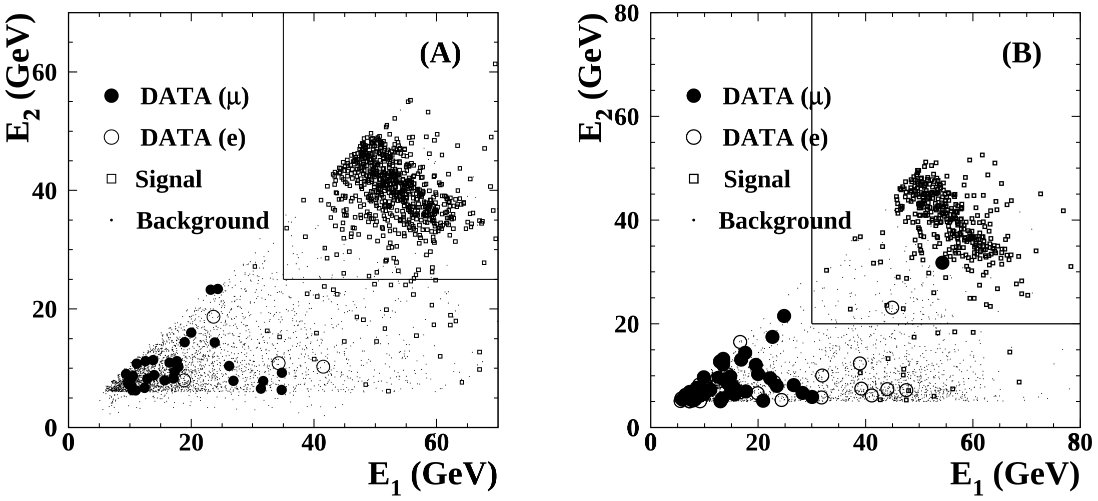

Figure 3.17: *Scatter plots of the energies of the two lepton candidates, after requiring two leptons for (A) 161 GeV and (B) 172 GeV. The solid lines indicate the positions of cut (1). Large open (filled) dots show electron (muon) candidate events, while small dots and squares are for the predicted background events and the expected Higgs boson signal.*

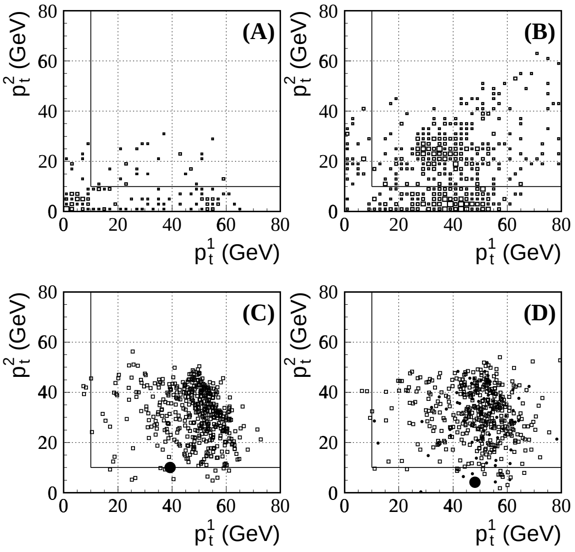

Figure 3.18: *Distributions of two lepton transverse momenta with respect to the nearest jet axis after cut (1) for (A) $q\bar{q}$ and (B) four-fermion background events. The distributions for the data (solid circles) and expected signal events (squares) are shown in (C) and (D) for electron and muon channels, respectively. All plots are for the 172 GeV data.*

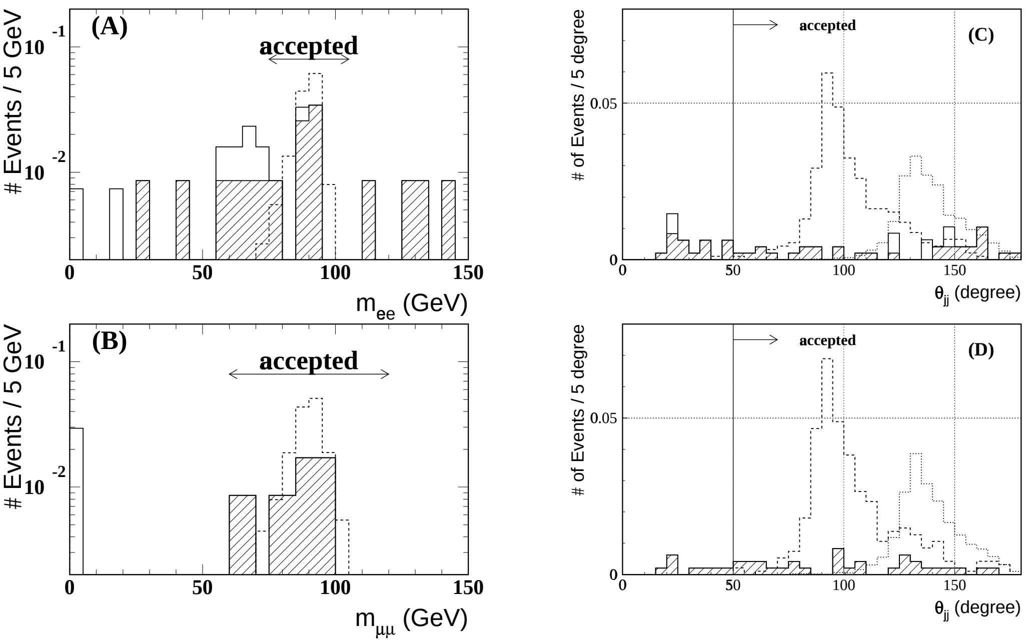

Figure 3.19: *(A)–(B): Distributions of lepton pair invariant mass after cut (2) for the (A) electron and (B) muon channels. Open (hatched) histograms show the predicted distributions for $q\bar{q}$ (four-fermion) background events. The distributions of the expected signals are shown by the dotted histograms. The horizontal arrows show the selected regions. (C)–(D): Distributions of opening angle of two jets after cut(3) for the (C) elctron and (D) muon channels in the 171 GeV analysis. The vertical lines show the cut value. Dashed (dotted) histograms show the expected signal distributions for m_{H^0} =65(68) GeV.*

3.5.4 Result

After all the cuts, **no events survive in the electron and muon channels, while 0.10±0.04 and 0.14±0.02 background events are expected in total at 161 GeV and 172 GeV, respectively**. The signal detection efficiencies for the 65 (68) GeV Higgs boson for the 161 (172) GeV analysis are 61.6 (65.3)% for the electron channel and 71.1 (70.3)% for the muon channel. The numbers of observed and expected events after each stage of the selection are given in Table 3.4. In the table the detection efficiencies for a 65 (68) GeV Higgs boson are also listed for the 161 (172) GeV data. The detection efficiencies for the Higgs boson of different masses are given in Table 3.5. Improvement in the electron channel analysis in the 172 GeV analysis can be seen with respect to that of the 161 GeV analysis.

Cut	Data	Total bkg.	$q\bar{q}(\gamma)$	4-ferm.	electron (%)	muon (%)
161 GeV					Efficiency m_{H^0}=65 GeV	
Preselection	337	330.0	299.4	30.7	89.9	82.6
Tow electron	4	6.8	5.0	1.9	68.0	—
cut (1)	0	0.4	0.2	0.2	66.5	—
cut (2)	0	0.2	0.06	0.15	64.8	—
cut (3)	0	0.06	0.01	0.05	61.6	—
cut (4)	0	0.06±0.02	0.01	0.05	61.6	—
Two muon	31	30.4	27.3	3.1	—	79.1
cut (1)	0	0.5	0.3	0.2	—	76.3
cut (2)	0	0.1	0.03	0.09	—	72.5
cut (3)	0	0.1	<0.01	0.08	—	71.1
cut (4)	0	0.04 ± 0.03	<0.01	0.04	—	71.1
172 GeV					Efficiency m_{H^0}=68 GeV	
Preselection	325	336	246	89.8	88.9	82.8
Two electron	34	30.0	19.3	10.1	74.4	—
cut (1)	1	1.2	0.5	0.7	70.5	—
cut (2)	1	0.5	0.1	0.4	68.0	—
cut (3)	0	0.1	0.02	0.09	65.3	—
cut (4)	0	0.08±0.02	0.02	0.06	65.3	—
Two muon	43	50.4	37.1	13.3	—	77.9
cut (1)	1	0.8	0.4	0.4	—	74.9
cut (2)	0	0.3	0.1	0.2	—	72.1
cut (3)	0	0.08	<0.01	0.08	—	70.3
cut (4)	0	0.06±0.01	<0.01	0.06	—	70.3

Table 3.4: *The numbers of events after each cut for the data and the expected background in the electron and muon channels. Background estimates are normalized to the integrated luminosity. The last two columns show the detection efficiencies for electron and muon channels for a 65 (68) GeV Higgs boson for 161 (172) GeV.*

		50	55	60	65	68	70	75	80
161 GeV	electron	59.0	61.9	63.4	61.3	57.7	52.6	33.1	14.6
	muon	68.1	69.6	70.4	70.5	69.4	67.8	60.1	46.1
172 GeV	electron	63.0	63.2	63.6	64.8	65.3	65.3	63.5	57.6
	muon	71.0	70.1	69.4	69.7	70.3	70.6	71.3	70.8

Table 3.5: *Signal detection efficiencies as a function of Higgs boson mass for the electron and muon channels.*

3.5.5 Systematics Errors

The signal detection efficiencies quoted in Table 3.5 are affected by various systematic uncertainties.

- Comparing the visible energy distributions of hadronic events taken at the Z^0 pole and the Monte Carlo samples, the Monte Carlo samples give relatively 8 % better energy resolution (See Figure 3.5). The R_{vis} cut is tightened by 0.03 corresponding to the visible energy of 5 GeV, which corresponds to twice the difference of the energy resolution between data and Monte Carlo. The efficiencies before and after this change are the same within the statistical accuracy. No systematic error is quoated from the modeling of visible energy.

- The systematic error from the modeling of the y_{34} value is estimated as follows. The y_{34} distributions after cut (P2) are compared between the data and the Monte Carlo. The cut value at which the data give the same effciency as the Monte Carlo is found to be 0.0009. Taking the difference of 10 % as an uncertainty, the cut value is tightned from 0.001 to 0.0011 to estimate the systematic error. This gives a systematic error of 0.35 (0.37) % for the electron (muon) channel.

- Since the resolutions of the jet direction, the track direction, the track momentum and the cluster energy measurements agree well between the data and the Monte Carlo, the systematic errors from the lepton p_t measurement, the lepton system invariant mass, and the opening angle of the hadron jets are neglected.

- Uncertainties on the lepton tagging efficiencies are estimated using the large angle Bhabha scattering event sample and the muon pair event sample taken at 91 GeV in order to get enough well-controlled samples. In such samples, if one tags one lepton with a strong requirement, the other should be a lepton of the same flavour. Applying the lepton identification to the known lepton, the efficiency can be estimated. The measured efficiencies of electron identification is shown in Figure 3.20 (A). The efficiencies obtained from the data and the Monte Carlo samples are compared. The relative difference as a function of $\cos\theta$ is then summed up according to the probability density of the lepton direction obtained from the Higgs signal Monte Carlo sample. Figures 3.20 (B), (C) and (D) show the relative difference of the electron tagging efficiency, the probability density, and the relative difference multiplied by the probability density. The difference is doubled because a signal event contains two leptons. Thus systematic shifts of the lepton-pair tagging efficiencies are obtained as 0.56±0.17 % for the electron channel and as 0.42±0.10 % for the muon channel. The correction of 0.56 % and 0.42 % are included in the efficiencies shown in the Tables 3.4 and 3.5. The errors of the corrections are treated as systematic errors.

- The effect from the fragmentation is estimated by comparing the samples in which the Higgs decays to $c\bar{c}$, gg and the normal sample excluding the events in which the Higgs decays into $\tau^+\tau^-$. The average of the efficiencies in the Higgs mass range of 50 – 75 GeV are consistent within the statistical error for both the electron and muon channels. However conservatively taking the largest difference, this systematic error is estimated as 0.23 % (0.27 %) for the electron (muon) channel.

Assuming all systematic errors to be independent, the total systematic errors on the signal detection efficiencies are calculated as 0.45 % for electron channel and 0.47 % for muon channel relative to the efficiencies quated in Tables 3.4 and 3.5.

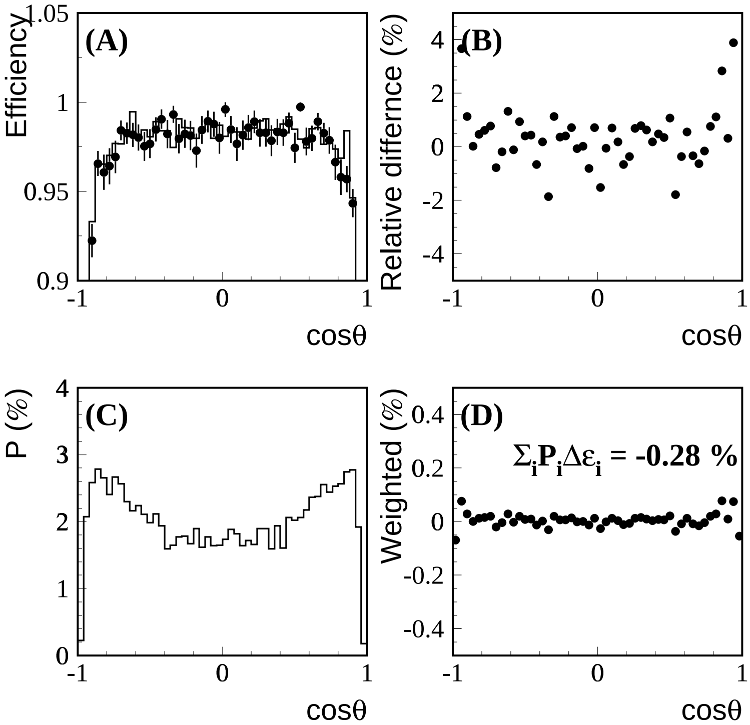

Figure 3.20: *(A): Electron tagging efficiency as a function of* $\cos\theta$ *for data (points) and Monte Carlo (histogram) events. (B): Relative difference of the electron tagging efficiency. (C): Probability density of the electron direction obtained from the Higgs Signal sample of* m_{H^0} *=68 GeV. (D): Relative difference of the efficiency multiplied by the probability.*

3.6 The Four Jets Channel

The event topology of the four jets channel is characterized by,

- four energetic hadron jets,
- no missing energy, and
- presence of b quark decay.

The backgrounds are $Z^0/\gamma^* \rightarrow q\bar{q}$ events accompanied by hard gluon emissions as well as the four-fermion processes, essentially $e^+e^- \rightarrow W^+W^-$ in this energy region.

The selection of candidate events and the suppression of background is done in two steps. A preselection is first performed in order to reduce the events which is not kinematically compatible with the signal. A tighter kinematic selection and a b tagging are then applied using a likelihood technique.

First, a large part of the $Z^0/\gamma^* \rightarrow q\bar{q}$ background is eliminated by selecting well defined four jet topologies using the cuts listed below:

(1) The events must be qualified as a hadronic final state described in section 3.4.3.

(2) The radiative process $e^+e^- \rightarrow Z^0\gamma \rightarrow q\bar{q}\gamma$ is largely eliminated by requiring that the effective center-of-mass energy, $\sqrt{s'}$, calculated as described in section 3.4.8, is at least 140 GeV (150 GeV) at $\sqrt{s} = 161$ GeV ($\sqrt{s} = 172$ GeV).

(3) The final state particles of an event are grouped into four jets using the Durham algorithm. The jet resolution parameter, y_{34}, at which the number of jets changes from 3 to 4, is required to be larger than 0.005.

(4) The $Z^0/\gamma^* \rightarrow q\bar{q}$ background is further suppressed by requiring that the event shape parameter C[40] is larger than 0.45. The C parameter is defined as,

$$C = 3(\lambda_1\lambda_2 + \lambda_1\lambda_3 + \lambda_2\lambda_3),$$

where λ_i $(i = 1, 2, 3)$ is the eigenvalue of the sphericity tensor,

$$S^{\alpha\beta} = \frac{\sum_j \frac{p_j^\alpha p_j^\beta}{|p_j|}}{\sum_j |p_j|} \quad (\alpha, \beta = 1, 2, 3),$$

where p_j is the momuntum of the j-th energy flow particle. The C parameter is large for a spherical event.

(5) Each of the four jets is required to contain at least two tracks and two electromagnetic calorimeter clusters.

(6) To discriminate against poorly reconstructed events, a kinematic fit, using energy and momentum conservation constraints (4C-fit), is required to converge with a probability larger than 0.01. The $e^+e^- \rightarrow H^0Z^0$ hypothesis is tested by a kinematic fit which, in addition to the energy and momentum conservation constraints, also forces two of the four jets to have an invariant mass equal to the Z^0 boson mass (5C-fit). This fit is applied in turn to all six possible combinations of the four jets to the Z^0 and H^0 bosons. The fit is required to converge for at least one combination with a probability of at least 0.01. The combination yielding the highest χ^2-probability is selected.

Table 3.6 shows the number of selected events in the data and the Monte Carlo at each stage of the cuts for both center-of-mass energies. After removing most of the two-photon background events (cut(1)), a good agreement between the observed data and the expected background can be seen.

Cut	Data	Total bkg.	$q\bar{q}(\gamma)$	4-ferm.	Efficiency (%)
161 GeV					m_{H^0} = 65 GeV
(1)	1572	1398.4	1345.9	52.5	99.9
(2)	395	377.5	351.1	26.4	89.5
(3)	65	54.1	38.0	16.1	81.4
(4)	51	40.6	26.2	14.4	75.6
(5)	49	33.2	21.5	11.7	70.5
(6)	26	24.2	14.0	10.2	62.3
$\mathcal{L}^{HZ} > 0.9$	0	0.75 ± 0.08	0.49	0.26	32.1
172 GeV					m_{H^0} = 68 GeV
(1)	1409	1306.7	1189.7	117.0	99.7
(2)	367	381.2	312.8	68.4	87.8
(3)	93	84.7	33.5	51.2	79.3
(4)	77	70.9	22.9	48.0	75.8
(5)	68	60.3	18.1	42.2	70.2
(6)	56	50.3	12.6	37.7	61.4
$\mathcal{L}^{HZ} > 0.925$	1	0.88 ± 0.07	0.34	0.55	28.5

Table 3.6: *The numbers of events after each cut of the selection for the data at 161 (172) GeV and the expected background in the four jets channel. The background estimates are normalized to 10.0 (10.4 pb^{-1}). The last column shows the selection efficiencies for the* $Z^0H^0 \to q\bar{q}b\bar{b}$ *final state.*

Next, a likelihood technique is employed in order to classify the remaining events as either (1) $Z^0/\gamma^* \to q\bar{q}$, (2) four-fermion process, or (3) $Z^0H^0 \to q\bar{q}b\bar{b}$. To select signal events with low background, the information from 14 quantities (described below) are combined, which provide a good separation between the three different event classes. Half of the variables are related to the kinematics of the events, and the other half are related to the b tagging. For each event the measured values x_i (i=1...14) of these variables are compared with probability density functions normalized to unity obtained from the Monte Carlo events processed through the full detector simulation. The likelihood for each event to belong to any of the three event classes is calculated as follows. For a single variable, the probability for an event to belong to a class j is given by

$$p_i^j(x_i) = \frac{f_i^j(x_i)}{\sum_{k=1}^{3} f_i^k(x_i)},$$

where $f_i^j(x_i)$ denotes the probability density for the event class j and variable i. The likelihood function for the class j is defined as the normalized product of the $p_i^j(x_i)$

$$\mathcal{L}^j(\vec{x}) = \frac{\prod_{i=1}^{n} p_i^j(x_i)}{\sum_{k=1}^{3} \prod_{i=1}^{n} p_i^k(x_i)},$$

where $n = 14$ is the number of variables. In order to select an event as a candidate, its likelihood for being a signal event is required to be larger than a certain value depending on the preferred signal/background ratio.

The first set of variables is used to select events whose kinematics are compatible with the signal.

(1) the smallest angle between any pair of jets.

(2) the smallest di-jet mass.

(3) the highest jet energy.

(4) the lowest jet energy.

(5) the di-jet mass closest to m_{Z^0}. The four-momenta of the jets obtained from the 4C-fit are used to calculate these quantities.

(6) The probability of the best kinematic fit requiring the energy–momentum conservation and equal di-jet masses.

(7) the larger $\beta = p/E$ factor of the two di-jet momenta calculated from the jet pair combination closest to the W^+W^- hypothesis. The best jet pair combination under the W^+W^- hypothesis is determined by minimizing $(p_{\text{dijet1}} - x)^2 + (p_{\text{dijet2}} - x)^2$, where x is 6 GeV (30 GeV) at $\sqrt{s}$ =161 GeV (172 GeV). This quantity vanishes for perfectly reconstructed on-shell W^+W^- events.

The second set of variables is used to tag b flavour hadrons. Secondary vertices are identified in each jet separately using the methods described in section 3.4.6. To improve the quality of the vertices, each accepted vertex is required to have at least two tracks containing 2 silicon microvertex hits in both r–ϕ and r–z strips. The variables to discriminate between the b flavour and lighter flavours are the followings.

(8) sum of the decay length significance of the vertices found in the candidate Higgs jets by the tear down algorithm.

(9) the maximum forward multiplicity among four jets.

(10) the invariant mass of the tracks in the vertex with the largest decay length significance.

(11) the smaller of the two Higgs jet masses.

(12) the sum of the momenta of the highest momentum track associated with each vertex of the two Higgs jets.

(13) the largest transverse momentum of an identified lepton (electron or muon) with respect to the corresponding jet axis.

(14) the sum of the two largest numbers of significant tracks in the four jets.

The reference distributions of the likelihood variables are shown in Figures 3.21 and 3.22 for the 161 GeV and 172 GeV analyses, respectively.

Finally the likelihood for each event is required to be larger than 0.90 at $\sqrt{s} = 161$ GeV and larger than 0.925 at $\sqrt{s} = 172$ GeV (i.e., $\mathcal{L}^3(\vec{x}) > 0.90\ (0.925)$). The likelihood requirement is tightened for the higher center-of-mass energy in order to retain the same background level for both energies.

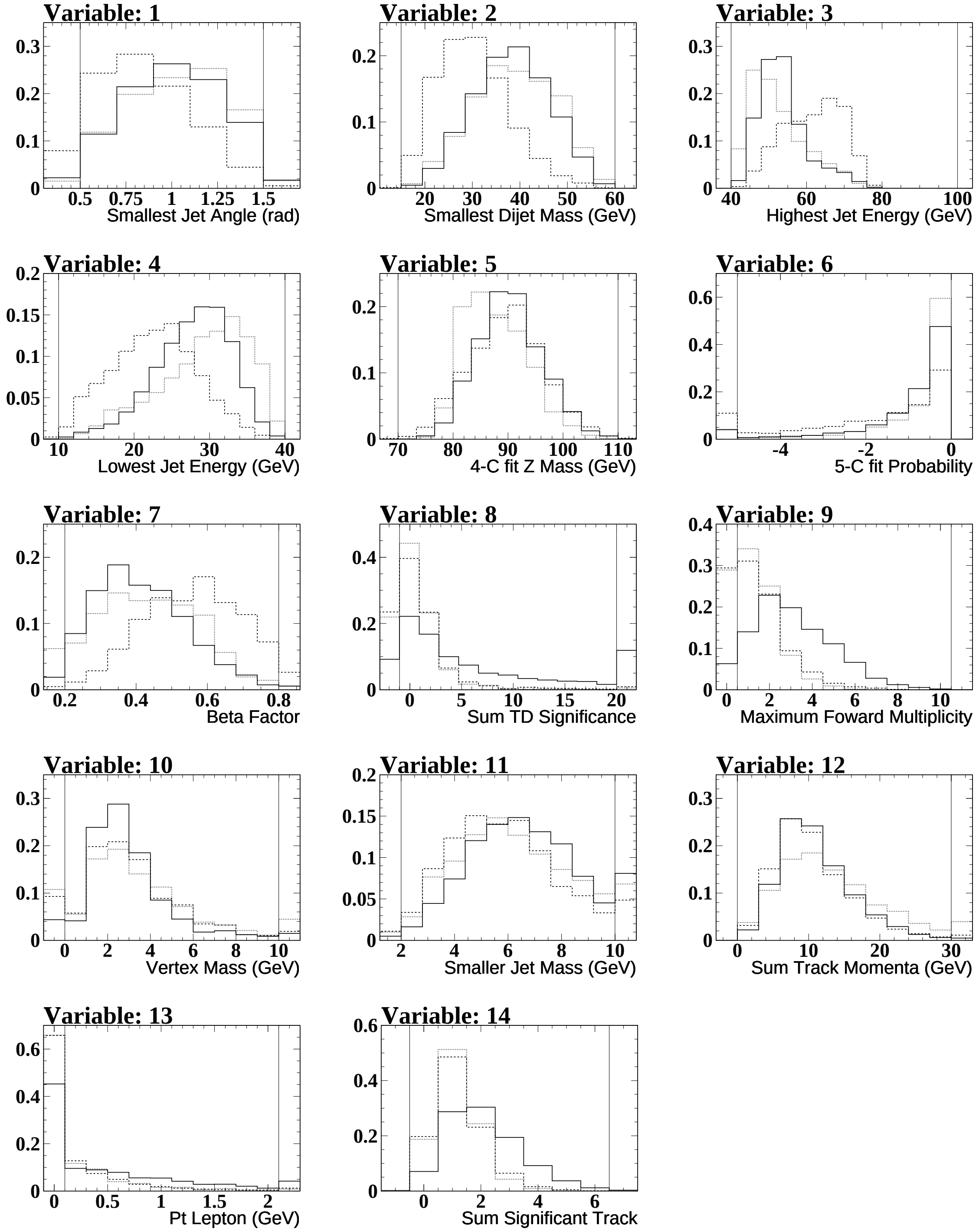

Figure 3.21: *Probability densitiy distributions for the 14 input variables used for the 161 GeV selection. Solid, dashed, and dotted histograms show the probability densities for the signal, $q\bar{q}$, and four-fermoion events. Bins outside the two vertical lines correspond to underflow and overflow events.*

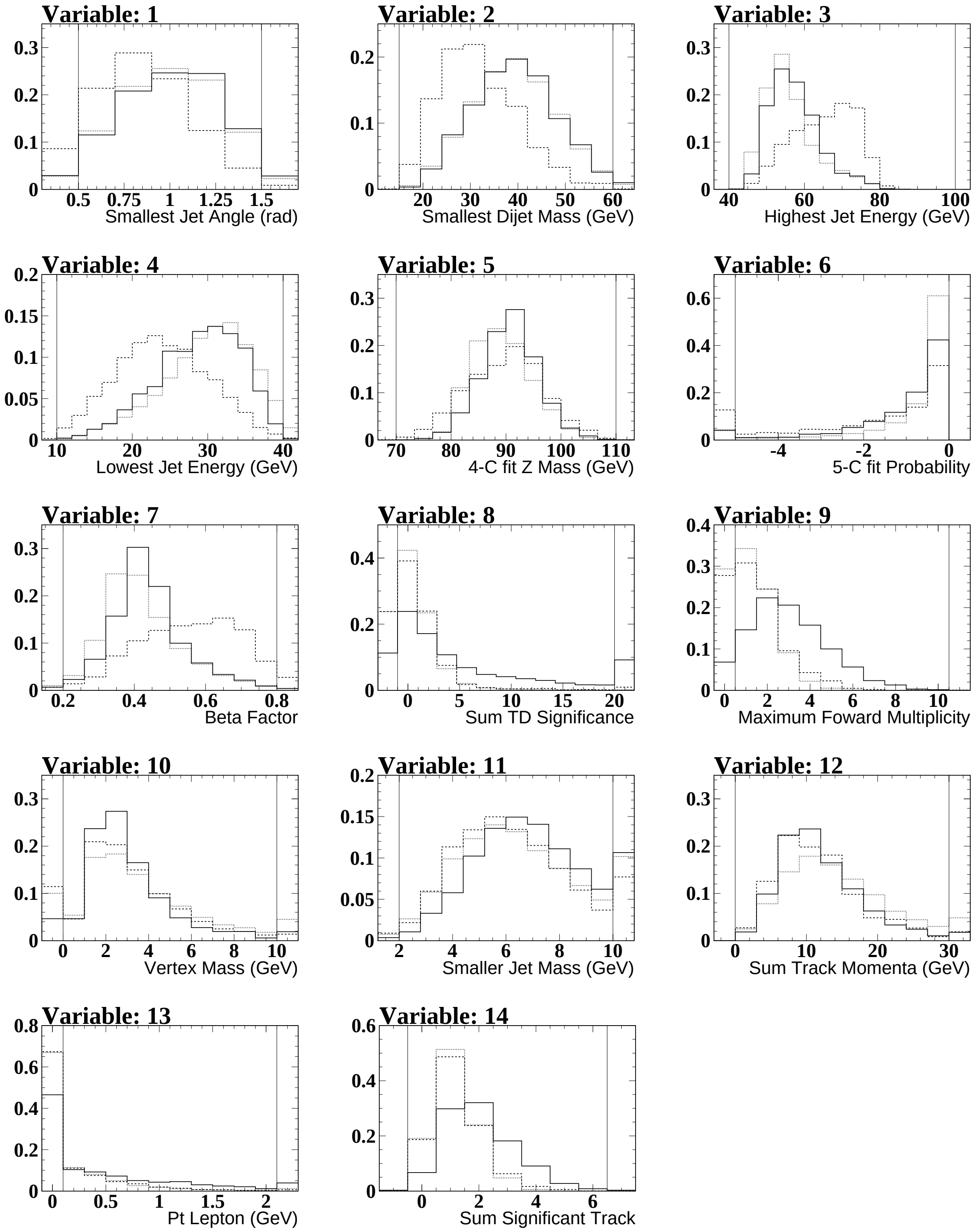

Figure 3.22: *Probability densitiy distributions for the 14 input variables used for the 172 GeV selection. Solid, dashed, and dotted histograms show the probability densities for the signal, $q\bar{q}$, and four-fermion events. Bins outside the two vertical lines correspond to underflow and overflow events.*

The analysis is tuned with a reference mass of m_{H^0} =65 GeV (68 GeV) at $\sqrt{s}$ = 161 GeV (172 GeV) with a resulting efficiency of 32.1% (28.5%). The efficiencies for different Higgs boson masses are listed in Table 3.7. The resulting expected background is 0.49 (0.34) events from Z^0/γ^* and 0.26 (0.55) events from the four-fermion processes. Other background sources are negligible. The total expected background is 0.75±0.08 (stat)±0.25 (syst) (0.88±0.07±0.18) events. The background systematics are dominated by the error in the modeling of the variables used in the likelihood.

For each of the fourteen input quantities, a good agreement between the data and the Monte Carlo is observed. This can be seen in Figures 3.23 and 3.24, where the distributions of the likelihood inputs of the data and the simulated background are shown. The agreement between the data and the Monte Carlo, in particular for b tagging related quantities, is also checked with the data taken in the calibration runs.

Figures 3.25 (A) and (B) show the distributions of the signal likelihood for the preselected events from the 161 GeV and 172 GeV data. It can be seen that the expected signal is concentrated at large values of the likelihood. The enhancement of the background at large likelihood values is due to irreducible signal like four-fermions and QCD four jets events containing the b flavour.

No events survive the likelihood cut of 0.9 at $\sqrt{s}$ = 161 GeV. With a cut at 0.925 in the likelihood variable one candidate event is selected from the data collected at $\sqrt{s}$ = 172 GeV. The likelihood of this event is 0.993. The invariant mass of the two jets associated with the Higgs boson decay is 75.6 ± 3.0 GeV. Both of the Higgs candidate jets have displaced secondary vertices with significances of 6.1 and 2.0, and charged multiplicities of 4 and 3. One of the jets assigned to the Z^0-candidate has also a displaced secondary vertex with a significance of 4.6 and multiplicity of 2.

	50	55	60	65	68	70	75	80
161	21.7	24.7	27.0	28.2	28.4	28.2	26.6	23.3
172	22.9	26.9	30.3	31.9	31.7	30.8	25.9	15.9

Table 3.7: *Signal detection efficiencies of the four jets channel for different Higgs boson masses.*

Systematic Errors The signal detection efficiencies at $\sqrt{s}$ = 161 GeV (172 GeV) are affected by the following uncertainties. Limited statistics of the Monte Carlo samples cause the systematic error of 4% (2%). The effect of modeling of the physics quantities used in the preselection is evaluated as follows. The agreement of the variables between the real data and the Monte Carlo expectations is checked with the data taken at the calibration runs. The systematic shifts of the variables are corrected. If the resolution is too optimistic, the cut values are tightened to reflect the uncertainty and see how the variation of the cut value affects to the efficiencies. Systematic uncertainty is found in $\sqrt{s'}$ resolution, y_{34}, and the C parameter. The systematic uncertainties of the description of the preselection variables give 5% (2%) systematic errors in total.

Systematics errors form the modeling of the variables used in the likelihood selection is dominated by the uncertainties of the b tagging variables. The effect of the tracking resolution is estimated by varyng the tracking resolution in the Monte Carlo samples. The modeling including the b tagging variables has been checked also by a re-weighting procedure. The distributions for the data and the Monte Carlo samples are compared, in which χ^2 is defined to quantify the agreement by the

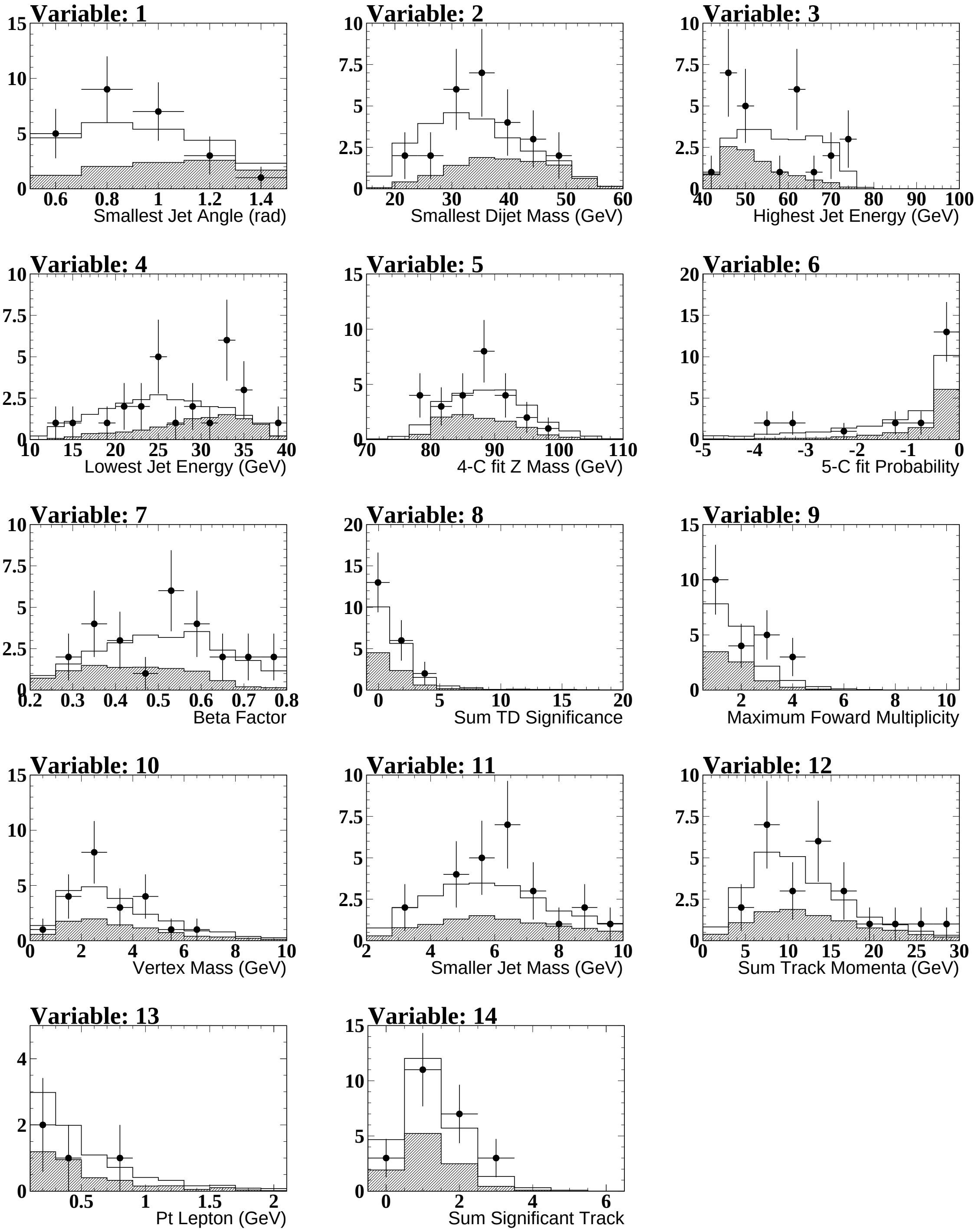

Figure 3.23: *Distributions of variables used in the 161 GeV likelihood selection for preselected data events (points with error bars). Open (hatched) histograms show the expected distributions for* $q\bar{q}$ *(four-fermion) events. All simulated distributions are normalized to the luminosity of the data.*

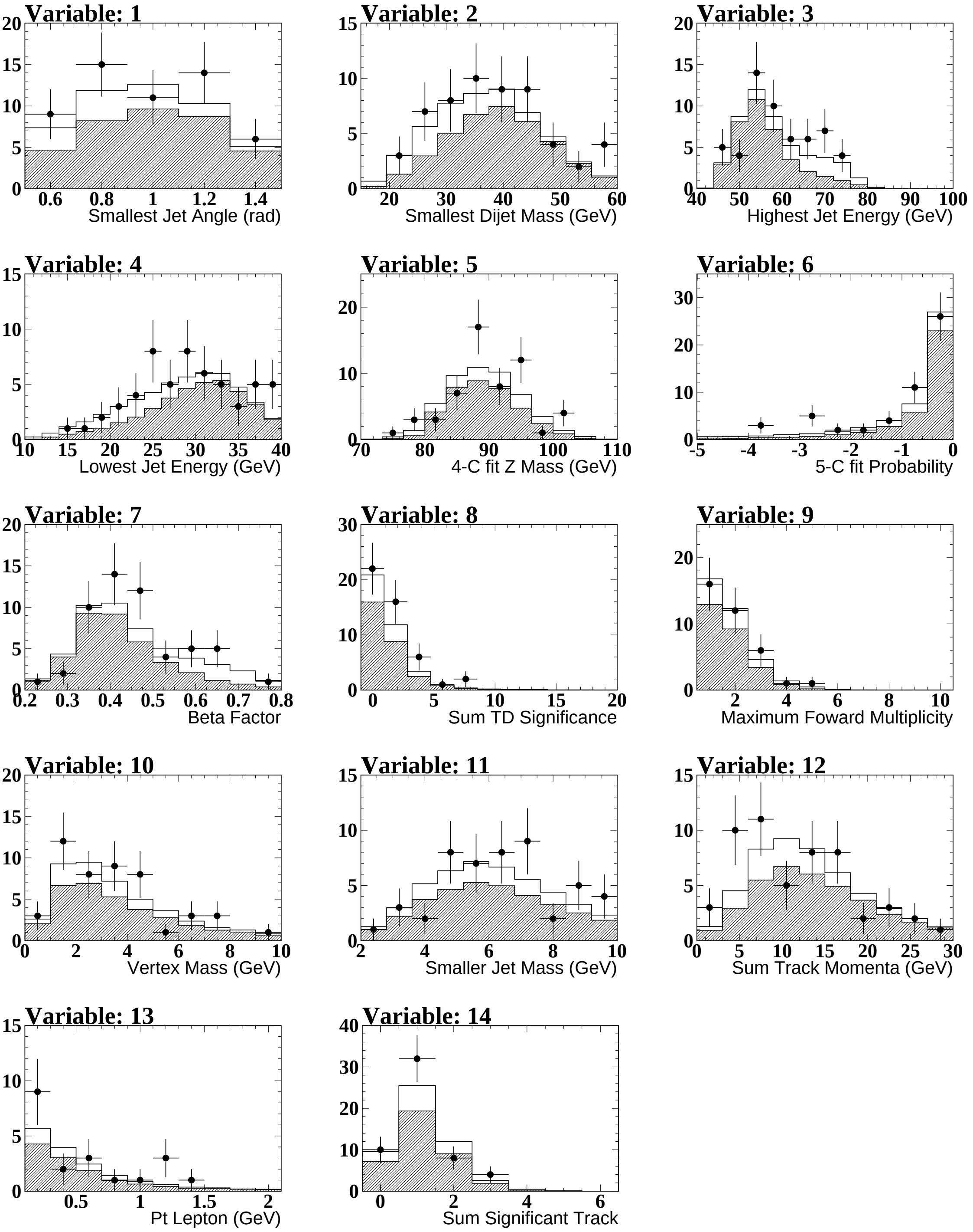

Figure 3.24: *Distributions of variables used in the 172 GeV likelihood selection for preselected data events (points with error bars). Open (hatched) histograms show the expected distributions for $q\bar{q}$ (four-fermion) events. All simulated distributions are normalized to the luminosity of the data.*

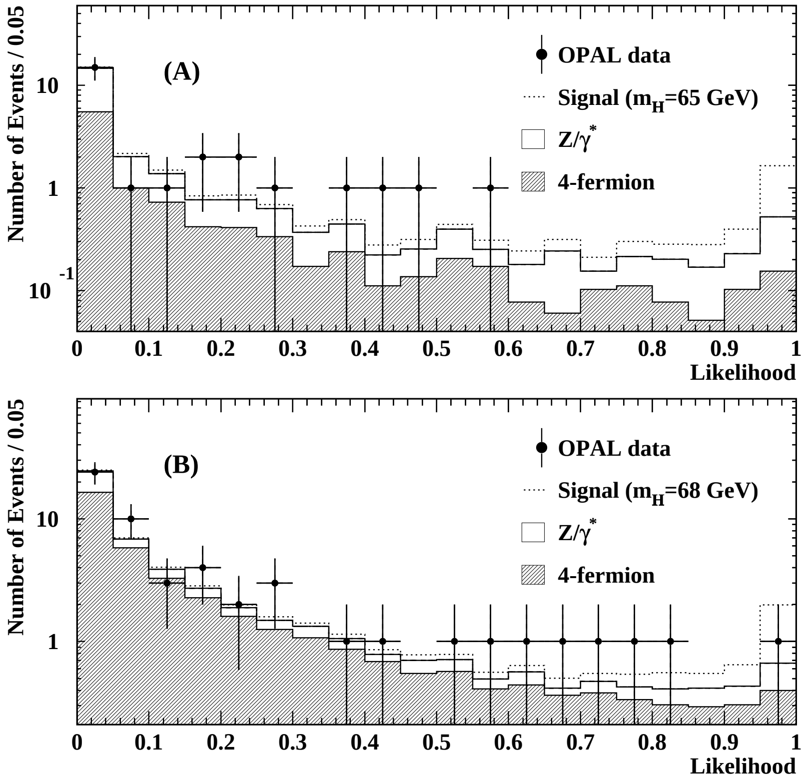

Figure 3.25: *Distributions of signal likelihood for (A) 161 GeV and (B) 172 GeV analysis. Points with error bars shows the preselected data events. Open (hatched) histograms show the predicted distributions for the $q\bar{q}$ (four-fermion) background events. Dotted Histograms are distribution for the expected Higgs boson events. All simulated distributions are normalized to the luminosity of the data.*

following formula;

$$\chi^2 = \sum_{i=1}^{N^{\text{vars}}} \frac{1}{N_i^{\text{bin}}} \sum_{j=1}^{N_i^{\text{bin}}} \chi_{ij}^2, \qquad \chi_{ij}^2 = \frac{(N_{ij}^{\text{data}} - N_{ij}^{\text{MC}})^2}{N_{ij}^{\text{MC}}} \tag{3.4}$$

where N^{vars} is the number of variables and N_i^{bin} is the number of bins in the ith distribution. The event weight, w is determined iteratively by the bin which gives the largest χ_{ij}^2 as the follows,

$$w_{\text{new}} = w_{\text{old}} \times \left\{ \left(\frac{N_{ij}^{\text{data}}}{N_{ij}^{\text{MC}}} - 1 \right) \alpha + 1 \right\},$$

where α is a factor between 0 and 1, stabilizing the iterative procedure and having small sensitivity to the final results. The distributions are re-generated using the new event weight. The re-genrated distributions are again compared and event weight is determined iteratively. The iteration is terminated when the χ^2 becomes smaller than a cut off value, ε. Using the event weight, the variation of the efficiencies is checked. Finally modeling of the variables used in the likelihood selection gives a systematic uncertainty of 10% (7%).

The binning of reference distributions yields a contribution to the systematic error of 1% (2%).

Taking these uncertainties as independent and adding them in quadrature result in a total relative systematic error on the signal efficiency of 12% (8%).

3.7 The Missing Energy Channel

The event topology of the missing energy channel is characterized by:

- a large missing momentum corresponding to a neutrino pair from the Z^0 decay,
- acoplaner two energetic hadronic jets, and
- presence of the b quark decay.

The background consists of badly measured $Z^0/\gamma^* \to q\bar{q}$ events, and four-fermion processes with a neutrino in the final state, such as $W^+W^- \to \ell^\pm \nu q\bar{q}$ and $W^\pm e^\mp \nu \to q\bar{q}\, e^\mp \nu$, and events in which particles go undetected down the beam pipe such as $e^+e^- \to Z^0\gamma$ and two-photon events.

(1) To reduce two-photon and beam-wall interactions, a preselection is applied.
  - There must be more than six tracks which pass the quality cuts described in 3.4.1.
  - The number of good tracks must exceed 20% of the total number of reconstructed tracks in the event.
  - The energy deposited in each side of the forward calorimeter, the gamma catcher and the silicon tungsten detector must be less than 2 GeV, 5 GeV, and 5 GeV, respectively.
  - The fraction of the energy deposited in the region $|\cos\theta| > 0.9$ must not exceed 30(50)% of the total visible energy in the event at 161 (172) GeV.
  - The total transverse momentum of the event, p_{vis}^t, must be greater than 1 GeV.
  - The visible mass must satisfy $m_{\text{vis}} > 4$ GeV.

(2) To remove background events in which particles go undetected down the beam pipe, the polar angle, θ_{miss}, of the missing momentum ($\vec{p}_{\mathrm{miss}} = -\vec{p}_{\mathrm{vis}}$) must satisfy $|\cos\theta_{\mathrm{miss}}| < 0.9$. The z component of the visible momentum, p^z_{vis}, is required to be less than 30 GeV.

(3) Many of the $\mathrm{e^+e^-}\rightarrow\mathrm{Z^0}\gamma$ events in which the photon is within the detector acceptance will survive the previous cuts. An electromagnetic cluster is identified as an isolated photon if no charged track except for the track tagged as conversion is found within a cone of 20° half angle around the cluster. If the event contains an isolated photon with an energy of more than 30 GeV, the event is rejected. This cut is only applied for 161 GeV data.

(4) The remaining two-photon background is eliminated by requiring $p^t_{\mathrm{vis}} > 8$ GeV. As a precaution against large fluctuations in the measured hadronic energy, p^t_{vis} is recalculated excluding hadronic calorimeter clusters and is also required to be larger than 5 (8) GeV.

(5) The event is reconstructed as a two-jet events using the Durham algorithm. Both jets are required to have a polar angle satisfying $|\cos\theta| < 0.9$, to ensure good containment. The jet resolution parameter, y_{23}, at which the event changes from the two-jet to the three-jet topology is required to be less than 0.05 at 161 GeV.

(6) The dominant remaining background comes from the $\mathrm{Z^0}/\gamma^*\rightarrow\mathrm{q\bar{q}}$ events in which the two jets tend to be back-to-back, in contrast to the signal events in which the jets are expected to be acoplaner. This background is suppressed by requiring that the jet-jet acoplanarity angle, ϕ_{acop}, be larger than 8°(5°). The acoplanarity angle is defined as $180° - \phi_{jj}$ where ϕ_{jj} is the angle between the two jets in the plane perpendicular to the beam direction.

Some of the distributions used in the missing energy channels are shown in Figure 3.26 and Figure 3.27 for the 161 and 172 GeV analyses, respectively.

After applying the above criteria, most of the remaining background events are $\mathrm{W^+W^-}\rightarrow\ell\nu\mathrm{q\bar{q}}$ events in which lepton is undetected or mixed in the jet activities or irreducible $\mathrm{Z^0Z^0}\rightarrow\nu\bar{\nu}\mathrm{q\bar{q}}$ events. According to the W-pair production cross-section, different selections are further applied for (A) 161 GeV and (B) 172 GeV.

(A) 161 GeV

(A7) To reduce four-fermion backgrounds which include an intermediate, on-shell, vector boson, the selected events are required to satisfy $m_{\mathrm{vis}} < 75$ GeV.

(B) 172 GeV

(B7) Since the Higgs boson recoils against the $\mathrm{Z^0}$ boson decaying into a pair of neutrinos, the signal has a missing mass close to $m_{\mathrm{Z^0}}$. The remaining backgrounds, predominantly from well contained multi-hadron and four-fermion events including the semi-leptonic $\mathrm{W^+W^-}$ decays, typically have small missing masses. These backgrounds are reduced by the missing mass requirement $76 < m_{\mathrm{miss}} < 120$ GeV.

(B8) The $\mathrm{W^+W^-}$events with one of the W bosons decaying leptonically and the other decaying into hadronic jets are reduced by requiring that the events have no isolated leptons. In this context, leptons are low-multiplicity jets with one (two or three) tracks associated to electromagnetic or hadronic energy clusters, confined to a cone of 5° (7°) half-angle, having an invariant mass less than 2.5 GeV and momentum in excess of 5 GeV. The lepton is considered isolated if the sum of the track momenta and the electromagnetic energies contained between the above lepton cone and an isolation cone of 25° half-angle does not exceed 10% (15%) of the lepton energy. If the lepton cone has only one track, the isolation cone is not allowed to contain another track.

(B9) The remaining background is mostly from semi-leptonic W^+W^- and $We\nu$ events where the charged lepton goes undetected down the beam pipe. These events are suppressed by requiring b hadrons in the hadronic jets for events with a visible mass close to the W boson mass. Each of the two hadronic jets is required to contain a secondary vertex with at least two tracks, each containing two hits in the r–ϕ strip of the silicon microvertex detector. The two vertices are reconstructed according to the tear down method described in section 3.4.6. The scatter plot of the sum of the decay length significances, Σ_S, and the visible mass of the event is shown in Figure 3.27 (D). The cut lines are also shown.

The numbers of observed and expected events after each stage of the selection are given in Table 3.8. The detection efficiencies for 65 GeV and 68 GeV Higgs bosons are also shown in Table 3.8. **The selection retains one event at 161 GeV. The expected background is 0.9±0.1 for 161 GeV and 0.55±0.05 for 172 GeV.** The candidate event has $p^t_{\mathrm{vis}} = 39.1$ GeV, $E_{\mathrm{vis}} = 53.1$ GeV, and $m_{\mathrm{vis}} = 37.0$ GeV. After corrections, the mass of the event is 39.3 ± 4.9 GeV, while the missing mass is 96.1 ± 10.0 GeV. These properties are compatible with those of the process $e^+e^- \rightarrow Z^0 + Z^0/\gamma^* \rightarrow \nu\bar{\nu}q\bar{q}$.

The detection efficiencies for different Higgs boson masses are listed in Table 3.9. These include a small correction due to accelerator-related backgrounds in the forward detectors which are not fully simulated.

Systematic Errors The detection efficiencies of the 161 (172) GeV selections are affected by the following uncertainties: Monte Carlo statistics, 2.0% (2.2%). Uncertainties from fragmentation, 1.5% (1.5%); from modeling of the cut variables, 3.0% (3.8%). In the 172 GeV analysis, uncertainties from the lepton and the b flavour tagging efficiencies give additional systematic errors of 5.6% and 2.6 %, respectively. Taking these uncertainties as independent and adding them in quadrature result in a total systematic uncertainty of 3.9% (7.7%).

3.8 The Tau Channels

The event topology of the tau channel is characterized by,

- presence of two tau leptons,
- two energetic hadronic jets, and
- either of the invariant masses of the taus or jets consistent with the Z^0mass.

The main backgrounds are $Z^0/\gamma^* \rightarrow q\bar{q}$ with two mis-identfied tau leptons and four-fermion processes with leptons in the final state.

The tau identification method in this analysis is developed to identify tau leptons in a high multiplicity environment. The identification method consists of three different algorithms, which address different decay channels of the tau lepton, namely (A) electron, (B) muon and (C) hadron(s). The basic idea of these methods is to find an isolated narrow jet or high momentum lepton.

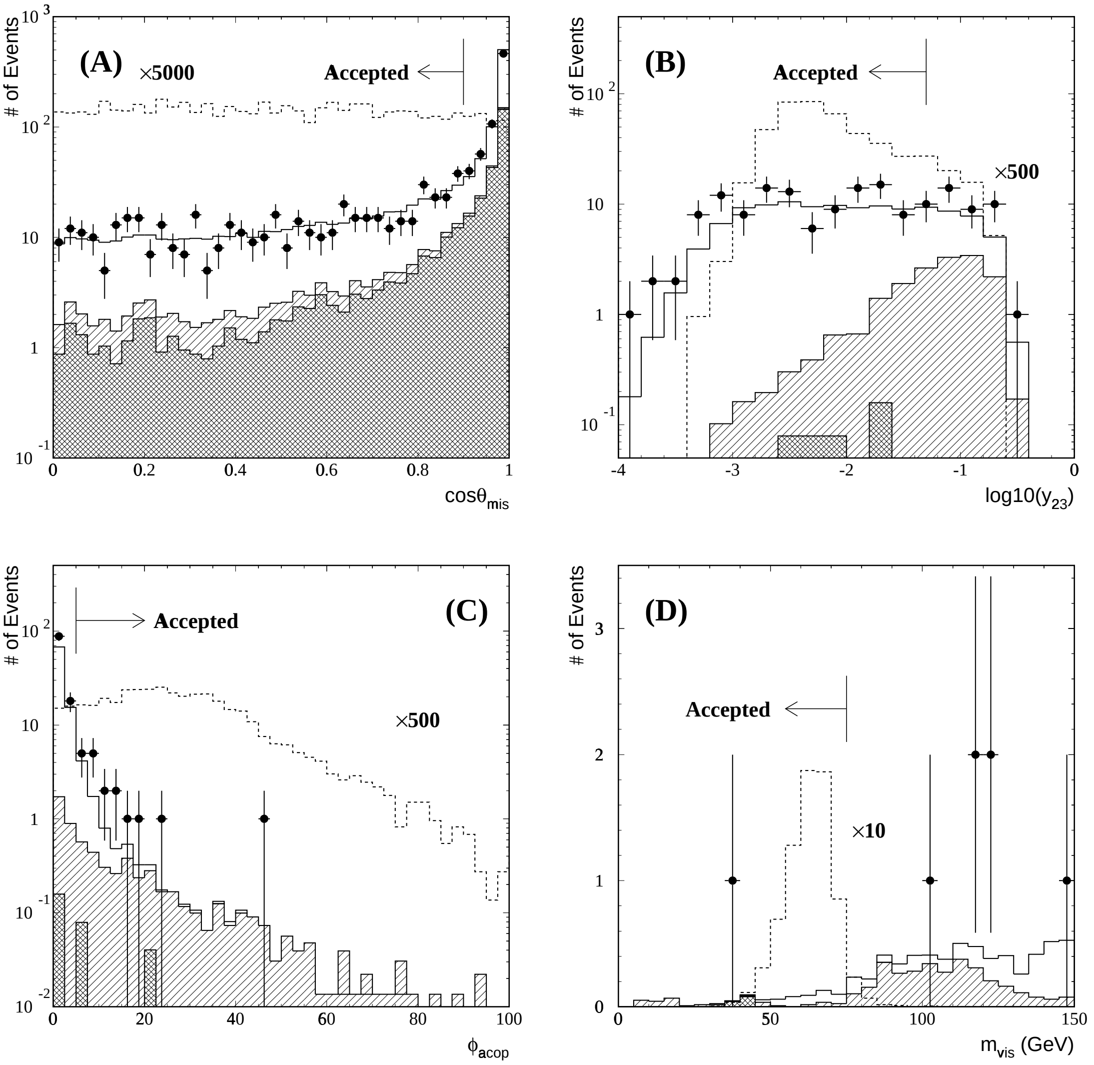

Figure 3.26: *Distributions of variables used in the missing energy channel at 161 GeV. (A): The direction of total missing momentum,* $|\cos\theta_{\rm mis}|$*, after cut (1). (B): Jet resolution paramter,* $\log_{10} y_{23}$*, after cut (4). (C): Acoplanarity angle,* $\phi_{\rm acop}$*, after cut (5). (D): Visible mass,* $m_{\rm vis}$*, after cut (6). Points with error bars show the distributions of the data events. Open, hatched, and double hatched histograms are Monte Carlo expectations from the* $q\bar{q}$*, four-fermion, and two-photon events. Dotted histograms shows the expected distributions of the 65 GeV Higgs boson. The signal histograms are scaled up for visibility. Vertical lines in the plots indicate the cut positions.*

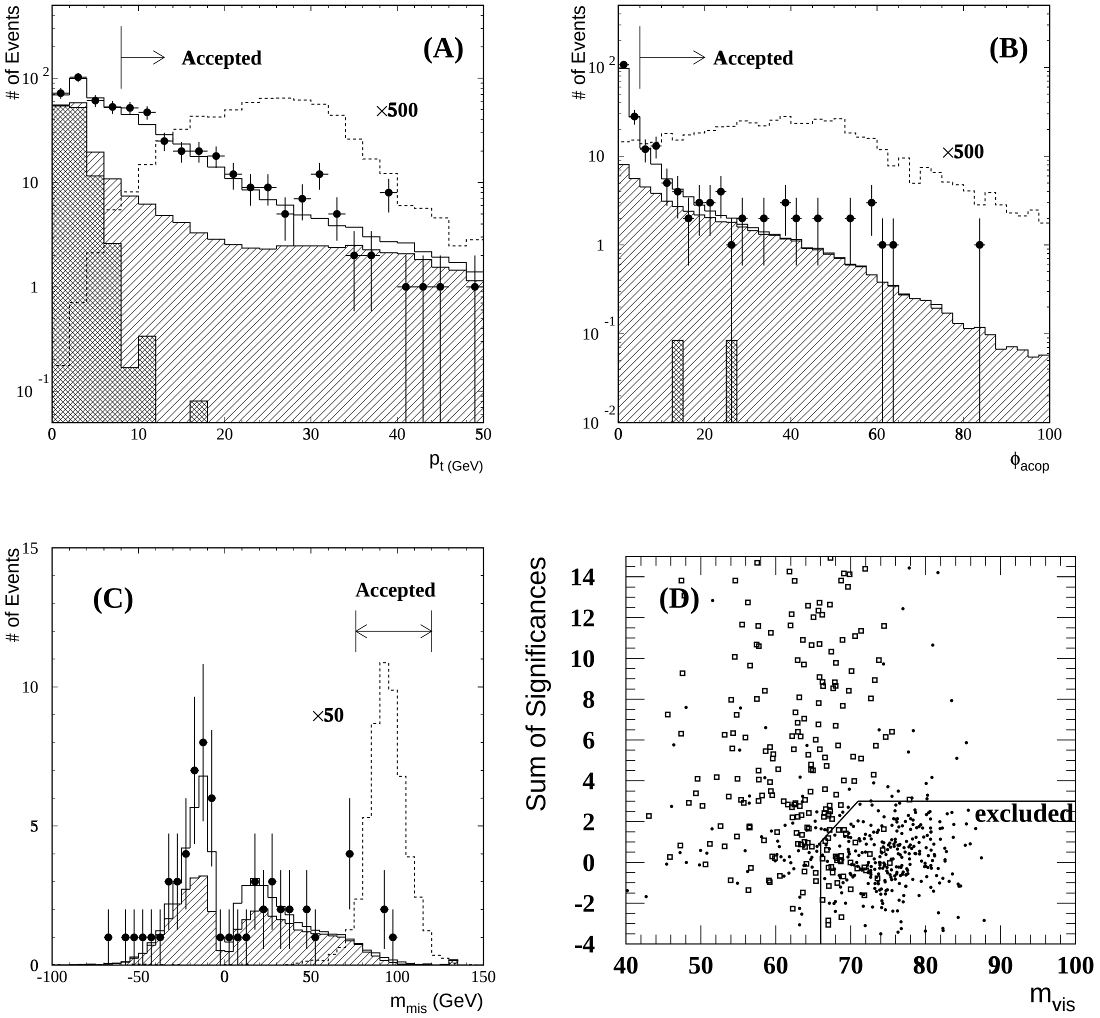

Figure 3.27: *Distributions of variables used in the missing energy channel at 172 GeV. (A): Total transverse momentum, p_t, before applying the p_t cut. (B): Acoplanarity angle, $\phi_{\rm acop}$, after cut (5). (C): Missing mass, $m_{\rm mis}$, after cut(6). The convention of the plots are the same as Figure 3.26. (D): Scatter plot of the sum of decay length significance and visible mass $m_{\rm vis}$ after cut (B8) together with the cut lines. Open squares (small dots) show the distribution for the signal (expected background) events.*

Cut	Data	Total bkg.	$q\bar{q}(\gamma)$	4-ferm.	$\gamma\gamma$	Efficiency (%)
161 GeV						m_{H^0} = 65 GeV
(1)	2055	1936.5	778.2	38.0	1120.1	80.5
(2)	1068	1047.7	332.1	28.5	687.0	71.6
(3)	1002	989.6	274.9	27.7	686.9	71.6
(4)	166	146.9	128.7	18.0	0.2	67.1
(5)	134	116.8	109.4	7.2	0.2	56.4
(6)	7	6.6	2.4	4.1	0.1	47.6
(A7)	1	0.9±0.1	0.2	0.7	0.1	46.0
172 GeV						m_{H^0} = 68 GeV
(1)	2984	2829	713	105	2011	83.3
(2)	1468	1486	302.1	86.7	1097	73.6
(4)	173	177.5	121.0	56.0	0.37	71.9
(5)	163	165.9	113.5	52.0	0.30	64.3
(6)	53	58.5	18.3	40.0	0.30	62.3
(B7)	2	2.2	0.6	1.5	0.1	55.2
(B8)	1	1.6	0.52	1.0	0.1	52.8
(B9)	0	0.55±0.05	0.275	0.275	0	42.7

Table 3.8: *The numbers of events after each cut for the data and the expected background for the missing energy channel. The background estimates are normalized to the data. The quoted error is statistical only. The last column shows the selection efficiencies for a 65 (68) GeV Higgs boson for the 161 (172) analysis.*

	50	55	60	65	68	70	75	80
161	59.5	56.7	52.0	45.7	41.3	38.1	29.6	20.4
172	42.0	46.6	46.9	44.4	42.7	41.3	34.3	19.2

Table 3.9: *Signal detection efficiencies for the missing energy channel as a function of the Higgs boson masses.*

(A) Electron An electron, identified by the method described in section 3.4.5, is classified as an electron tau candidate if the electron satisfies the following requirements.

- The momentum of the electron track exceeds 2 GeV.
- The number of electromagnetic clusters within a cone of 26° half-angle around the electron track, N^{26}_{em}, must be less than six.
- The ratio of the electromagnetic energy within an 11° cone to that within a 30° cone, $R^{11/30}_{\mathrm{em}}$, must be greater than 0.7.
- There must be no hadronic calorimeter cluster with energy greater than 0.6 GeV associated with the electron track.
- The electron should not be tagged as a photon conversion by the method described in reference [41].

(B) Muon A muon, identified by the method described in section 3.4.5, is classified as a muon tau candidate if the muon satisfies the following conditions.

- The momentum of the track exceeds 3 GeV.
- The N^{26}_{em} is less than 5.
- The ratio of the scalar sum of all track momenta within an 11° cone to that within a 30° cone, $R^{11/30}_{\mathrm{ct}}$ must be greater than 0.7.

(C) Hadron The remaining tau lepton decays are identified as narrow, isolated jets. Jets are reconstructed using a cone algorithm [42] with a half-angle of 23° and with an associated energy of at least 3 GeV. Within each resulting jet, a narrow sub-jet of 11° half-angle and having the highest energy is formed in an iterative procedure. The narrow sub-jets are accepted as tau candidates if they satisfy the following requirements.

- The jet axis is in the region $|\cos\theta| < 0.92$.
- The ratio $R^{11/30}_{\mathrm{em}}$ is grater than 0.6.

If there are two tau lepton candidates with momentum vectors separated by less than 23°, one being identified as a leptonic decay and one as a narrow jet, the candidate identified as a leptonic decay is selected.

The selection proceeds as follows:

(1) At least two tau lepton candidate are found by the method described above.

(2) The total track multiplicity of the event must exceed eight.

(3) Most of the two-photon and $\mathrm{e^+e^-}\to\mathrm{Z^0}\gamma$ background events are eliminated by applying the following set up cuts.

  - The energy in the forward calorimeter, gamma catcher, and silicon tungsten detector are required to be less than 4, 10, and 10 GeV, respectively.

  - The direction of the total missing momentum,θ_{miss} should satisfy $|\cos\theta_{\text{miss}}|$ <0.97.
  - The total transverse momentum, p^t_{vis}, is required to be larger than 3 GeV.
  - The scalar sum of all track and cluster transverse momenta is required to be larger than 40 GeV.

(4) The remaining $Z^0/\gamma^*\to q\bar{q}$ background, with and without radiation, is partially suppressed by requiring that events contain at least four jets, reconstructed using the cone algorithm with a 23° half-angle. The electrons and muons from tau lepton decays are recognized as low-multiplicity "jets". Further suppression is done by removing the events containing isolated photons with energies of more than 15 GeV. An isolated photon is defined in this channel as an electromagnetic cluster with no track within a cone of 30° half-angle.

(5) In the signal events, 2.3 tau candidates are identified per event on average. Fake candidate pairs are removed by requiring that the sum of charges be zero. At 172 GeV, fake tau candidates containing three charged tracks are removed, if a χ^2 probability of the tracks originating from a common vertex in three dimensions is larger than 1%. Then pairwise isolation parameter is required to satisfy, $|\cos\alpha_1 \cdot \cos\alpha_2| < 0.8$, where α_i is the angle between the direction of the ith tau candidate and that of the nearest track not associated with it. In the cases where more than one candidate pair pass the selection, the pair with the lowest track multiplicity is chosen and, in case of ambiguity, the one with the lowest value of $|\cos\alpha_1 \cdot \cos\alpha_2|$.

The hadronic part of the event, obtained by excluding the selected tau lepton pair, is then split into two jets using the Durham algorithm. The invariant masses of the tau lepton pair, $m_{\tau\tau}$, and of the hadron jets, m_{had}, are calculated using only the tau lepton and jet momentum directions and requiring the energy–momentum conservation. At this point the selection split into two flows, one (A) sensitive to the $Z^0H^0\to\tau^+\tau^-q\bar{q}$ final state and the other (B) sensitive to the $Z^0H^0\to q\bar{q}\tau^+\tau^-$ final state.

(6A) The selected events must satisfy the following set of cuts.

  - The event must satisfy 75 GeV$< m_{\tau\tau} <$ 105 GeV and m_{had} >30 GeV.
  - The visible energy, E_{vis}, is required to be less than 145 (155) GeV at 161 (172) GeV, since the neutrinos from the tau lepton decays give rise to a relatively large missing energy.
  - If the tau lepton candidates are both classified as electron decay or both as muon decay, their opening angle is required to be larger than 90°. This cut is implemented to suppress specific four-fermion backgrounds, from $e^+e^-\to Z^0/\gamma^*$ + Z^0/γ^* and $e^+e^-\to Z^0e^+e^-$.
  - If the tau lepton candidates are both classified as electron decay, neither of the electrons is allowed to lie within 36° of the beam axis.

(6B) The selected events must satisfy the following set of cuts. Since in this case the mass cuts are less effective against the background, the requirements on the properties of the tau lepton candidates are tightened.

  - The events must satisfy 75 GeV$< m_{\text{had}} <$ 105 GeV and $m_{\tau\tau} >$ 30 GeV.
  - The opening angle of the tau lepton pair must be larger than 110°.
  - If one of the tau candidates has a track multiplicity exceeding two, the pairwise isolation cut is tightened to $|\cos\alpha_1 \cdot \cos\alpha_2| < 0.55$.

- To suppress four-fermion backgrounds, a lepton pair of the same species is rejected.
- To suppress the process $\mathrm{W}^+\mathrm{W}^-\to\ell\nu\mathrm{q}\bar{\mathrm{q}}$, the events are rejected if they contain any track or cluster with an energy exceeding 40 GeV.

Some distributions of variables used in the tau channels are shown in Figure 3.28. The numbers of observed and expected events after each stage of the selection are given in Table 3.10. The detection efficiency for a 65 (68) GeV Higgs boson is also given. **No candidate events are observed while the background is estimated to be 0.16±0.04 (0.59±0.04) events.**

The detection efficiencies for different Higgs boson masses are given in Table 3.11. These include a small correction of 2.3 % coming from accelerator-related backgrounds in the forward detectors which are not fully simulated.

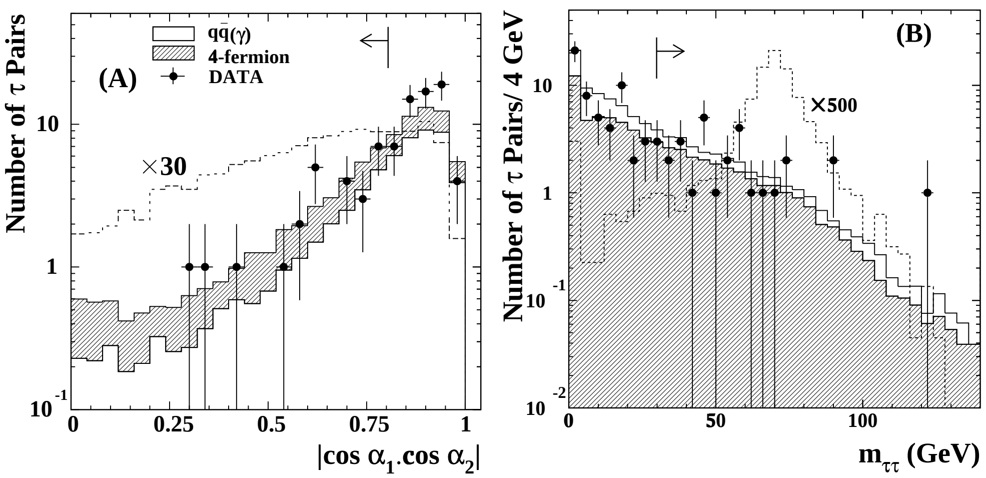

Figure 3.28: *(A): Distribution of the pair-wise isolation variable after cut (3) at 161 GeV. (B): Reconstructed tau-pair invariant mass distribution after cut (4) at 172 GeV. Points with error bars are the distributions for the data events. Open (Hatched) histograms show the Monte Carlo expectations from the* $q\bar{q}$ *(four-fermion) events. Dashed histograms show expected distributions for the signal. For visibility, the signal distributions are scaled.*

Systematic Errors The detection efficiencies of the 161 (172) GeV selections are affected by the following uncertainties: Monte Carlo statistics, 2.8 (2.8) %; uncertainty in the tau lepton identification efficiency, 2.0 (4.3)%; uncertainties in the modeling of cut variables excluding the tau lepton identification, 6.0 (9.1)% in case A and 4.0 (7.6)% in case B; uncertainties in the modeling of fragmentation and hadronization, 1.2 (1.2)%. Taking these uncertainties as independent and adding them in quadrature results in a total systematic uncertainty of 7.0 (10.4)% (case A) and 5.4 (9.2)% (case B) (relative errors).

Cut	Data	Total bkg.	$q\bar{q}(\gamma)$	4-ferm.	$\gamma\gamma$	$\ell^+\ell^-$	ε(%), case A	ε(%), case B
161 GeV							m_{H^0} =65 GeV	m_{H^0} =65 GeV
(1)	858	778.4	95.6	29.8	604.7	48.3	59.7	59.6
(2)	402	398.0	92.8	18.2	287.0	0	59.4	59.0
(3)	45	44.7	30.9	13.3	0.5	0	54.8	53.5
(4)	32	30.1	19.6	10.1	0.4	0	52.6	51.5
(5)	0	3.3	1.2	2.1	0	0	44.0	36.6
(6-A)	0	0.10±0.03	0.04	0.06	0	0	20.3	–
(6-B)	0	0.06±0.03	0.02	0.04	0	0	–	19.5
172 GeV							m_{H^0} =68 GeV	m_{H^0} = 68 GeV
(1)	857	611.5	77.8	79.9	421.6	32.2	58.5	59.3
(2)	358	306.9	75.2	36.8	194.9	0	58.3	58.6
(3)	50	55.1	23.6	31.2	0.3	0	54.0	52.9
(4)	37	40.1	15.2	24.7	0.2	0	51.7	50.8
(5)	15	20.1	6.9	13.2	< 0.07	0	41.8	40.8
(6-A)	0	0.41±0.03	<0.01	0.41	<0.07	0	22.9	–
(6-B)	0	0.18±0.02	0.02	0.16	<0.07	0	–	18.9

Table 3.10: *The numbers of events after each cut for the data and the expected background for the tau channels. The background estimate is normalized to data. The last two columns show the selection efficiencies, for cases A and B, for 65 (68) GeV Higgs boson for 161 (172) GeV.*

		50	55	60	65	68	70	75	80
161 GeV	$H^0 \rightarrow \tau^+\tau^-$	14.8	17.8	19.5	19.4	18.3	17.0	12.1	4.2
	$H^0 \rightarrow q\bar{q}$	26.2	25.6	23.9	21.1	18.9	17.3	12.8	8.0
172 GeV	$H^0 \rightarrow \tau^+\tau^-$	8.3	11.6	15.1	17.9	18.9	19.3	18.3	14.1
	$H^0 \rightarrow q\bar{q}$	28.7	28.0	26.6	24.5	22.9	21.7	18.2	14.0

Table 3.11: *Signal detection efficiencies for the tau channels for the different Higgs boson masses.*

Chapter 4

Results

4.1 Statistical Combination of the Channels

Each statistical procedure starts with the construction of a single test-statistic, X, from the number and the pattern of the selected events. In this case X is a function of the reconstructed Higgs boson mass. The test-statistic observed, X_{obs}, is compared to distributions of the same test-statistic, expected on the basis of "gedanken experiments" for particular Higgs boson mass hypotheses. These are obtained either analytically or using Monte Carlo simulation. A given mass hypothesis is excluded at the confidence level $1 - CL$, where CL is the probability for gedanken experiments to obtain $X_{\mathrm{s+b}} < X_{\mathrm{obs}}$, and $X_{\mathrm{s+b}}$ is the test-statistic expected for the *signal and background* hypothesis. This is the classical definition:

$$CL_{\mathrm{s+b}} = P(X_{\mathrm{s+b}} < X_{\mathrm{obs}}). \tag{4.1}$$

Instead of $CL_{\mathrm{s+b}}$, the normalized signal confidence level

$$CL_{\mathrm{s}} = \frac{P(X_{\mathrm{s+b}} < X_{\mathrm{obs}})}{P(X_{\mathrm{b}} < X_{\mathrm{obs}})} \tag{4.2}$$

is defined. Here X_{b} is the test-statistic expected assuming *background only* and X_{s} is that expected assuming *signal only*. The 95% c.l. lower limit for the Higgs boson mass is the value of the hypothetical mass which yields $CL_{\mathrm{s}} = 0.05$.

The statistical method used here is based on fractional event counting [43]. A weight is assigned to each selected candidate, i, according to a filter function $w_i = F(m_i)$. The argument m_i is the reconstructed Higgs boson mass in the event; however, any other discriminating observable can be used instead. The weights attributed to candidate events are added in all channels resulting in a total weight $w = \sum_i w_i$, which is the test-statistic X in equations (4.1) and (4.2). The filter function, $F(m_i)$, depends on the hypothetical Higgs boson mass, m_{H^0}; therefore, the total weight w, is also a function of m_{H^0}: it becomes large at values of m_{H^0} where candidate events cluster. The probability distribution of the total weight, $P(w)_{\mathrm{s+b}}$, including signal and background events, forms the basis for the evaluation of confidence levels.

In principle, the filter function $F(m)$ is arbitrary. The construction of the weight distribution function, $P_1(w)$, for the case of one signal event and no background event, is illustrated in Figure 4.1, assuming a specific form for $F(m)$. In the figure, the function $D(m)$ describes the actual mass distribution and the hatched areas indicate the probability $P_1(w)\Delta w$ for the Higgs particle to yield a weight inside an interval Δw. The $P(w)$ distributions for fixed numbers of signal events and no background event can be obtained from $P_1(w)$ by iterative integration, and the total probability density $P_{\mathrm{s}}(w)$ is obtained by adding the whole set of functions, weighted with the Poisson distribution

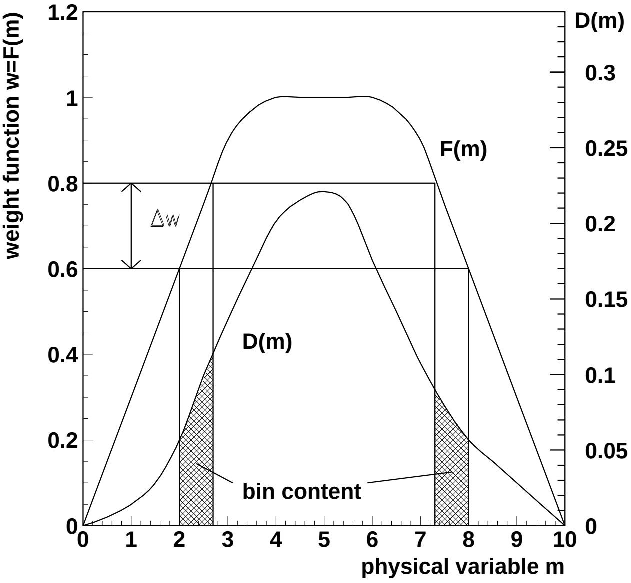

Figure 4.1: *Relation between the mass distribution* $D(m)$*, the filter function* $F(m)$*, and the probability* $P_1(w)\Delta w$ *(hatched area) for one candidate event to have a weight* $w \pm \Delta w/2$*. In the example the weight area is chosen as* $w \pm \Delta w/2 = 0.7 \pm 0.1$.

for the expected number of Higgs bosons. The distribution $P_\mathrm{s}(w)$ is thus sensitive to the Higgs boson production rate.

An analogous procedure leads to the w distribution, $P_b(w)$, of background events, which can be combined with the signal distribution, $P_\mathrm{s}(w)$, to evaluate the overall distribution, $P_\mathrm{s+b}(w)$. The function $P_\mathrm{s+b}(w)$ includes then the background predicted by the Standard Model and depends on the signal rate which is a function of m_{H^0}.

The confidence level is computed, in accordance with equation (4.2), as

$$CL_\mathrm{s} = \frac{\int_0^{w_\mathrm{obs}} P_\mathrm{s+b}(w)dw}{\int_0^{w_\mathrm{obs}} P_\mathrm{b}(w)dw}. \tag{4.3}$$

The denominator is introduced to avoid situations with excessively low limits arising when less candidates are observed than expected.

The filter function is chosen to provide good discrimination between signal and background events. For a single decay channel and a flat background distribution it is adequate to use the mass distribution itself: $F(m) = \frac{D(m)}{D_\mathrm{max}}$, where D_max is the maximum value of $D(m)$. When several channels with different efficiencies and backgrounds are to be combined, a channel-dependent filter function is introduced to account for the differing signal-to-background ratios:

$$F_k(m) = K \cdot \frac{1}{C + \frac{b_k(m)\cdot\sum_k S_k}{D_{k,\mathrm{max}}\cdot S_k}} \cdot \frac{D_k(m)}{D_{k,\mathrm{max}}}. \tag{4.4}$$

Here, S_k is the expected signal rate in channel k and b_k the differential background rate. The factor K is chosen such as to fix the largest value of $F_k(m)$ to unity. The constant C is a free parameter which can be optimized by minimizing the signal confidence level in *background only* gedanken experiments, as a function of the Higgs boson mass hypothesis.

The above filter function has the following properties:

- In the limit of very low background, $F_k(m)$ approaches a universal value K/C at the mass peak positions, independently of the channel number k;
- $F_k(m)$ is invariant under arbitrary splitting of any decay channel;
- If the background is large compared to the signal, $F_k(m)$ is proportional to the local signal to background ratio;
- For C equal to the total number of expected events, the maximum of $F_k(m)$ is proportional to the probability for a candidate in channel k to be a signal event.

4.2 Lower Mass Limit for the Standard Model Higgs Boson

The following uncertainties affecting the numbers of expected signal events are common to all search channels:

- the uncertainty in the integrated luminosity: 0.6%,
- the uncertainty in the Higgs boson production cross-section [44], which includes that from the collider energy: 1%, and
- the uncertainty of the Higgs decay branching ratios: 2% [44, 45].

Taking these uncertainties as independent and adding them in quadrature results in a systematic error, common to all search channels, of 3% (relative). In estimating the number of expected events for an assumed Higgs boson mass, these uncertainties are added in quadrature to those affecting the individual search channels.

The signal detection efficiencies as functions of the Higgs boson mass are summarized in Figure 4.2 (A) for 161 GeV and (B) for 172 GeV.

To derive a new limit on the Higgs boson mass, this search, with one candidate event in the four jets channel at 172 GeV (m_{H^0}=75.6 ± 3.0 GeV where the error is derived by a Gaussian fit to the peak of a 75 GeV Higgs Monte Carlo distribution), is combined with earlier OPAL searches at $\sqrt{s} \approx m_{\mathrm{Z}^0}$ with one candidate in the leptonic channel (m_{H^0}=61.2 ± 1.0 GeV). Two candidates from earlier searches with $m_{\mathrm{H}^0} < 25$ GeV are not considered further.

Figure 4.3 (A) shows the number of expected events for 161 GeV, 172 GeV and their sum, as a function of the Higgs boson mass. Also shown is the 95% confidence level upper limit on the number of observed candidate events. **A lower limit on the Higgs boson mass, 69.4 GeV, is extracted at the 95% Confidence Level.** In deriving this limit, the probability that a candidate event with a given observed mass actually originates from a Higgs boson of arbitrary mass is calculated as described in section 4.1. The expected background is reduced by the systematic error per channel and then subtracted. It is found that the errors on the background estimation have marginal effects on the results, reducing the derived limit only by 0.1 GeV. The systematic errors are incorporated into the limit according to the method prescribed in reference [46], reducing the derived limit by an additional 0.1 GeV. The effect of channel weighting and background subtraction is small. If all channels were assigned equal weights, irrespective of the expected rate and background, and no

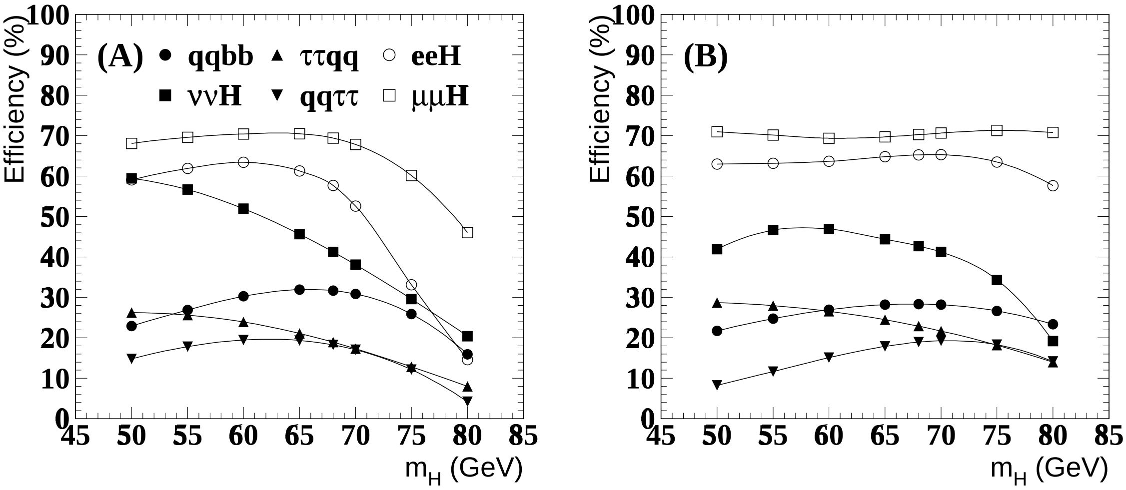

Figure 4.2: *Signal selection efficiencies as functions of the Higgs boson mass (A) for 161 GeV and (B) for 172 GeV analyses.*

background subtraction had performed, the limit would go down to only 69.0 GeV. If the results from the search at the Z^0 were not included, the limit would be 68.8 GeV.

Figure 4.3 (B) shows the measured confidence level and the expected one (averaged over a large number of hypothetical experiments with no signal and candidates spread according to the expected background distributions) as functions of the Higgs boson mass. From this Figure it can be seen that the expected limit is at 65.4 GeV and the expected confidence level for the experimental limit of 69.4 GeV is 82%. According to Monte Carlo trial experiments a reasonable value of 11.8% was found for the probability of inferring a mass limit greater than or equal to 69.4 GeV assuming no contribution from a Higgs boson signal.

4.3 Combined Lower Mass Limit from Four LEP Experiments

The results of the four LEP experiments at LEP2 energies are combined, where the different statistical procedures are adopted in each experiment [47]. Figure 4.4 shows expected and observed confidence levels obtained from combining the results of LEP experiments separately for four different statistical procedures. On combining the results, only the searches at LEP2 energies are considered. All four procedures give similar mass limits. The lowest obtained value of 77.5 GeV is chosen as the conservative combined limit. Table 4.1 summarizes the efficiencies, expected events, and observed events for each of the four experiments.

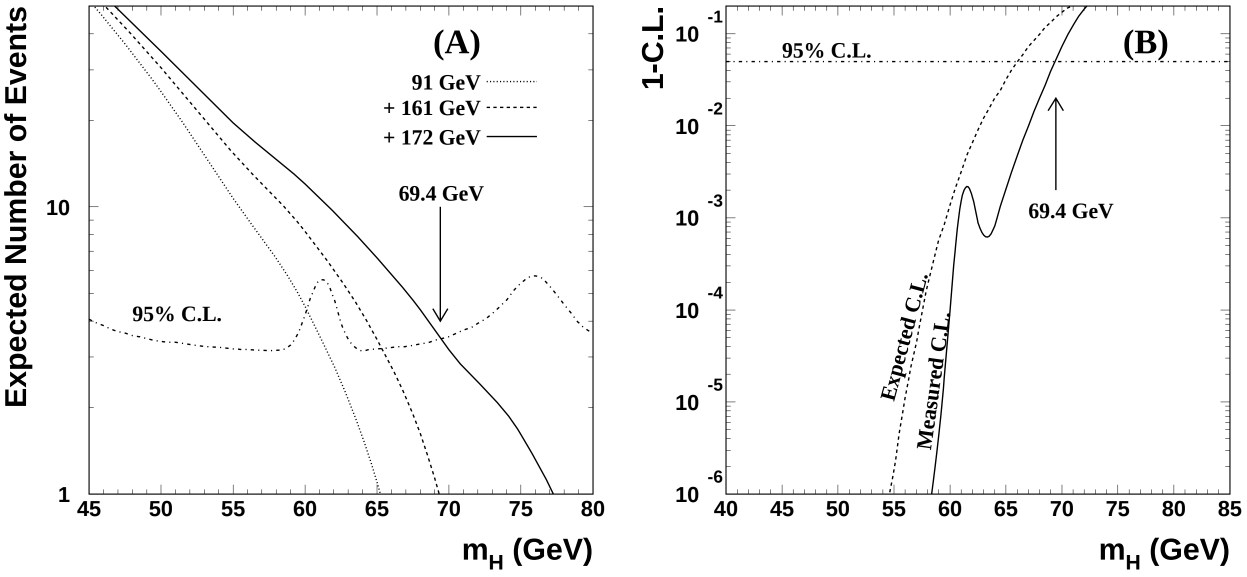

Figure 4.3: *(A): Expected number of events as a function of the Higgs boson mass for the searches at the* Z^0 *pole (dotted), including 161 GeV analysis (dashed) and the grand total (solid line). The dash-dotted horizontal line is the 95% confidence level upper limit for a possible Higgs boson signal in the presence of the observed high-mass candidate events. The intersection of the solid curve with the dash-dotted curve, indicated by the arrow, determines the 95% confidence level lower limit. (B) The expected (dashed) and measured (solid) confidence levels as functions of the Higgs boson mass.*

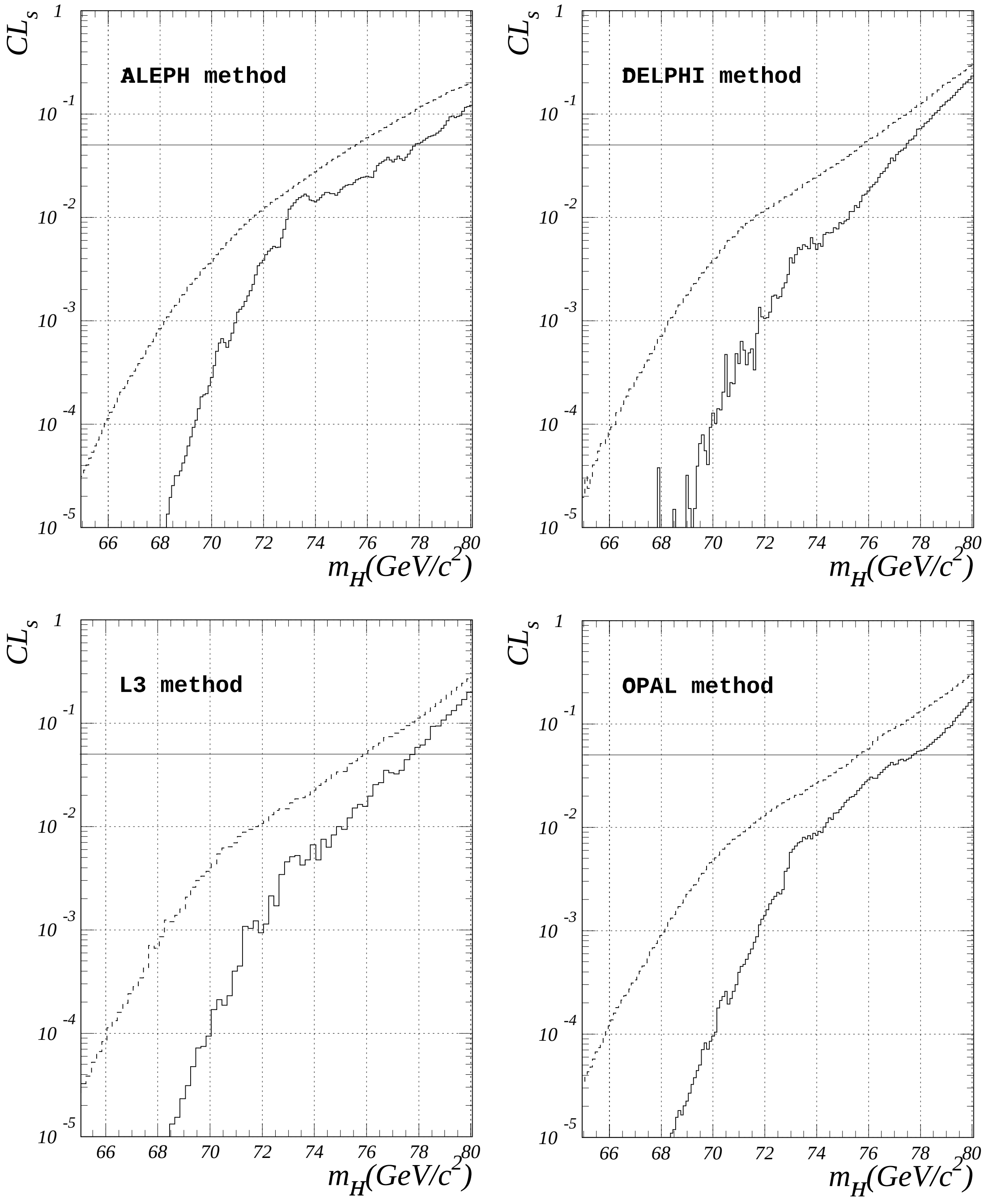

Figure 4.4: *Expected and observed confidence levels, CL_s, as functions of the hypothetical Higgs boson mass, obtained from combining the results of the LEP experiments using the four statistical methods. The intersections of the curves with the 5% horizontal line define the 95% confidence level. lower bounds, expected and observed, for the mass of the Standar Model Higgs boson.*

	OPAL		ALEPH		DELPHI		L3	
	ε	N_{bg}	ε	N_{bg}	ε	N_{bg}	ε	N_{bg}
161 GeV								
Four Jets	30.8 %	0.75	21.1 %	0.17	21.6 %	0.30	28.1 %	0.77
Missing Energy	38.1 %	0.90	26.3 %	0.06	36.3 %	0.65	46.0 %	0.40
Tau	17.2 %	0.16	18.0 %	0.07	22.4 %	0.63	5.4 %	0.01
Electron and Muon	60.2 %	0.10	64.2 %	0.06	55.4 %	0.17	40.0 %	0.07
172 GeV								
Four Jets	28.2 %	0.88	21.9 %	0.23	23.6 %	0.50	38.5 %	3.68
Missing Energy	41.3 %	0.55	42.9 %	0.09	42.8 %	0.61	69.4 %	1.46
Tau	20.7 %	0.59	18.6 %	0.05	24.4 %	1.13	24.6 %	0.48
Electron and Muon	68.0 %	0.14	74.8 %	0.11	53.5 %	0.33	57.1 %	0.33
Total Exp. Signal	3.05		2.85		2.72		3.86	
Total Exp. Background	4.07		0.84		4.24		7.21	
Total Observed Events	2		0		2		6	
Exp. Limit	65.4 GeV		68.5 GeV		65.1 GeV		65.8 GeV	
Obs. Limit	68.8 GeV		69.6 GeV		65.7 GeV		69.0 GeV	

Table 4.1: *The efficiencies and expected background events in each search channel of four LEP experiments for a Higgs boson mass of the 70 GeV. The total expected number of signal events, total expected background events, and total observed events are also shown. The last two rows shows the expected and observed mass limits using the data collected at the LEP2 energies.*

Chapter 5

Summary

A search for the Standard Model Higgs boson has been performed for the data collected in 1996 by the OPAL detector at center-of-mass energies of 161.3, 170.3 and 172.3 GeV. The data used in the alalysis corespond to 10.0 pb^{-1} at 161.3 GeV, 1.0 pb^{-1} at 170.3 GeV, and 9.4 pb^{-1} at 172.3 GeV. The search is sensitive to the main final states in which the Higgs boson is produced in association with a fermion anti-fermion pair; namely four jets, two jets with missing energy, and two jets with a pair of leptons. Two candidate events have been observed, one at 161.3 GeV and the other at 172.3 GeV, consistent with the Standard Model background expectations. Combined with earlier searches at center-of-mass energies in the vicinity of the Z^0 resonance, this search leads to a lower limit of 69.4 GeV for the mass of the Standard Model Higgs boson, at the 95% confidence level.

Appendix A

The OPAL Collaboration

The OPAL detector was built and is operated by the collaboration of the following people from 34 institutes:

K. Ackerstaff[8], G. Alexander[23], J. Allison[16], N. Altekamp[5], K.J. Anderson[9], S. Anderson[12], S. Arcelli[2], S. Asai[24], D. Axen[29], G. Azuelos[18,a], A.H. Ball[17], E. Barberio[8], R.J. Barlow[16], R. Bartoldus[3], J.R. Batley[5], S. Baumann[3], J. Bechtluft[14], C. Beeston[16], T. Behnke[8], A.N. Bell[1], K.W. Bell[20], G. Bella[23], S. Bentvelsen[8], S. Bethke[14], O. Biebel[14], A. Biguzzi[5], S.D. Bird[16], V. Blobel[27], I.J. Bloodworth[1], J.E. Bloomer[1], M. Bobinski[10], P. Bock[11], D. Bonacorsi[2], M. Boutemeur[34], B.T. Bouwens[12], S. Braibant[12], L. Brigliadori[2], R.M. Brown[20], H.J. Burckhart[8], C. Burgard[8], R. Bürgin[10], P. Capiluppi[2], R.K. Carnegie[6], A.A. Carter[13], J.R. Carter[5], C.Y. Chang[17], D.G. Charlton[1,b], D. Chrisman[4], P.E.L. Clarke[15], I. Cohen[23], J.E. Conboy[15], O.C. Cooke[8], M. Cuffiani[2], S. Dado[22], C. Dallapiccola[17], G.M. Dallavalle[2], R. Davis[30], S. De Jong[12], L.A. del Pozo[4], K. Desch[3], B. Dienes[33,d], M.S. Dixit[7], E. do Couto e Silva[12], M. Doucet[18], E. Duchovni[26], G. Duckeck[34], I.P. Duerdoth[16], D. Eatough[16], J.E.G. Edwards[16], P.G. Estabrooks[6], H.G. Evans[9], M. Evans[13], F. Fabbri[2], M. Fanti[2], A.A. Faust[30], F. Fiedler[27], M. Fierro[2], H.M. Fischer[3], I. Fleck[8], R. Folman[26], D.G. Fong[17], M. Foucher[17], A. Fürtjes[8], D.I. Futyan[16], P. Gagnon[7], J.W. Gary[4], J. Gascon[18], S.M. Gascon-Shotkin[17], N.I. Geddes[20], C. Geich-Gimbel[3], T. Geralis[20], G. Giacomelli[2], P. Giacomelli[4], R. Giacomelli[2], V. Gibson[5], W.R. Gibson[13], D.M. Gingrich[30,a], D. Glenzinski[9], J. Goldberg[22], M.J. Goodrick[5], W. Gorn[4], C. Grandi[2], E. Gross[26], J. Grunhaus[23], M. Gruwé[8], C. Hajdu[32], G.G. Hanson[12], M. Hansroul[8], M. Hapke[13], C.K. Hargrove[7], P.A. Hart[9], C. Hartmann[3], M. Hauschild[8], C.M. Hawkes[5], R. Hawkings[27], R.J. Hemingway[6], M. Herndon[17], G. Herten[10], R.D. Heuer[8], M.D. Hildreth[8], J.C. Hill[5], S.J. Hillier[1], P.R. Hobson[25], R.J. Homer[1], A.K. Honma[28,a], D. Horváth[32,c], K.R. Hossain[30], R. Howard[29], P. Hüntemeyer[27], D.E. Hutchcroft[5], P. Igo-Kemenes[11], D.C. Imrie[25], M.R. Ingram[16], K. Ishii[24], A. Jawahery[17], P.W. Jeffreys[20], H. Jeremie[18], M. Jimack[1], A. Joly[18], C.R. Jones[5], G. Jones[16], M. Jones[6], U. Jost[11], P. Jovanovic[1], T.R. Junk[8], D. Karlen[6], V. Kartvelishvili[16], K. Kawagoe[24], T. Kawamoto[24], P.I. Kayal[30], R.K. Keeler[28], R.G. Kellogg[17], B.W. Kennedy[20], J. Kirk[29], A. Klier[26], S. Kluth[8], T. Kobayashi[24], M. Kobel[10], D.S. Koetke[6], T.P. Kokott[3], M. Kolrep[10], S. Komamiya[24], T. Kress[11], P. Krieger[6], J. von Krogh[11], P. Kyberd[13], G.D. Lafferty[16], R. Lahmann[17], W.P. Lai[19], D. Lanske[14], J. Lauber[15], S.R. Lautenschlager[31], J.G. Layter[4], D. Lazic[22], A.M. Lee[31], E. Lefebvre[18], D. Lellouch[26], J. Letts[12], L. Levinson[26], S.L. Lloyd[13], F.K. Loebinger[16], G.D. Long[28], M.J. Losty[7], J. Ludwig[10], A. Macchiolo[2], A. Macpherson[30], M. Mannelli[8], S. Marcellini[2], C. Markus[3], A.J. Martin[13], J.P. Martin[18], G. Martinez[17], T. Mashimo[24], P. Mättig[3], W.J. McDonald[30], J. McKenna[29], E.A. Mckigney[15], T.J. McMahon[1], R.A. McPherson[8], F. Meijers[8], S. Menke[3], F.S. Merritt[9], H. Mes[7], J. Meyer[27], A. Michelini[2], G. Mikenberg[26], D.J. Miller[15], A. Mincer[22,e], R. Mir[26], W. Mohr[10], A. Montanari[2], T. Mori[24], M. Morii[24], U. Müller[3], S. Mihara[24], K. Nagai[26], I. Nakamura[24], H.A. Neal[8],

B. Nellen[3], R. Nisius[8], S.W. O'Neale[1], F.G. Oakham[7], F. Odorici[2], H.O. Ogren[12], A. Oh[27], N.J. Oldershaw[16], M.J. Oreglia[9], S. Orito[24], J. Pálinkás[33,d], G. Pásztor[32], J.R. Pater[16], G.N. Patrick[20], J. Patt[10], M.J. Pearce[1], R. Perez-Ochoa[8], S. Petzold[27], P. Pfeifenschneider[14], J.E. Pilcher[9], J. Pinfold[30], D.E. Plane[8], P. Poffenberger[28], B. Poli[2], A. Posthaus[3], D.L. Rees[1], D. Rigby[1], S. Robertson[28], S.A. Robins[22], N. Rodning[30], J.M. Roney[28], A. Rooke[15], E. Ros[8], A.M. Rossi[2], P. Routenburg[30], Y. Rozen[22], K. Runge[10], O. Runolfsson[8], U. Ruppel[14], D.R. Rust[12], R. Rylko[25], K. Sachs[10], T. Saeki[24], E.K.G. Sarkisyan[23], C. Sbarra[29], A.D. Schaile[34], O. Schaile[34], F. Scharf[3], P. Scharff-Hansen[8], P. Schenk[34], J. Schieck[11], P. Schleper[11], B. Schmitt[8], S. Schmitt[11], A. Schöning[8], M. Schröder[8], H.C. Schultz-Coulon[10], M. Schumacher[3], C. Schwick[8], W.G. Scott[20], T.G. Shears[16], B.C. Shen[4], C.H. Shepherd-Themistocleous[8], P. Sherwood[15], G.P. Siroli[2], A. Sittler[27], A. Skillman[15], A. Skuja[17], A.M. Smith[8], G.A. Snow[17], R. Sobie[28], S. Söldner-Rembold[10], R.W. Springer[30], M. Sproston[20], K. Stephens[16], J. Steuerer[27], B. Stockhausen[3], K. Stoll[10], D. Strom[19], P. Szymanski[20], R. Tafirout[18], S.D. Talbot[1], S. Tanaka[24], P. Taras[18], S. Tarem[22], R. Teuscher[8], M. Thiergen[10], M.A. Thomson[8], E. von Törne[3], S. Towers[6], I. Trigger[18], Z. Trócsányi[33], E. Tsur[23], A.S. Turcot[9], M.F. Turner-Watson[8], P. Utzat[11], R. Van Kooten[12], M. Verzocchi[10], P. Vikas[18], E.H. Vokurka[16], H. Voss[3], F. Wäckerle[10], A. Wagner[27], C.P. Ward[5], D.R. Ward[5], P.M. Watkins[1], A.T. Watson[1], N.K. Watson[1], P.S. Wells[8], N. Wermes[3], J.S. White[28], B. Wilkens[10], G.W. Wilson[27], J.A. Wilson[1], G. Wolf[26], T.R. Wyatt[16], S. Yamashita[24], G. Yekutieli[26], V. Zacek[18], D. Zer-Zion[8]

[1]School of Physics and Space Research, University of Birmingham, Birmingham B15 2TT, UK
[2]Dipartimento di Fisica dell' Università di Bologna and INFN, I-40126 Bologna, Italy
[3]Physikalisches Institut, Universität Bonn, D-53115 Bonn, Germany
[4]Department of Physics, University of California, Riverside CA 92521, USA
[5]Cavendish Laboratory, Cambridge CB3 0HE, UK
[6] Ottawa-Carleton Institute for Physics, Department of Physics, Carleton University, Ottawa, Ontario K1S 5B6, Canada
[7]Centre for Research in Particle Physics, Carleton University, Ottawa, Ontario K1S 5B6, Canada
[8]CERN, European Organisation for Particle Physics, CH-1211 Geneva 23, Switzerland
[9]Enrico Fermi Institute and Department of Physics, University of Chicago, Chicago IL 60637, USA
[10]Fakultät für Physik, Albert Ludwigs Universität, D-79104 Freiburg, Germany
[11]Physikalisches Institut, Universität Heidelberg, D-69120 Heidelberg, Germany
[12]Indiana University, Department of Physics, Swain Hall West 117, Bloomington IN 47405, USA
[13]Queen Mary and Westfield College, University of London, London E1 4NS, UK
[14]Technische Hochschule Aachen, III Physikalisches Institut, Sommerfeldstrasse 26-28, D-52056 Aachen, Germany
[15]University College London, London WC1E 6BT, UK
[16]Department of Physics, Schuster Laboratory, The University, Manchester M13 9PL, UK
[17]Department of Physics, University of Maryland, College Park, MD 20742, USA
[18]Laboratoire de Physique Nucléaire, Université de Montréal, Montréal, Quebec H3C 3J7, Canada
[19]University of Oregon, Department of Physics, Eugene OR 97403, USA
[20]Rutherford Appleton Laboratory, Chilton, Didcot, Oxfordshire OX11 0QX, UK
[22]Department of Physics, Technion-Israel Institute of Technology, Haifa 32000, Israel
[23]Department of Physics and Astronomy, Tel Aviv University, Tel Aviv 69978, Israel
[24]International Centre for Elementary Particle Physics and Department of Physics, University of Tokyo, Tokyo 113, and Kobe University, Kobe 657, Japan

[25]Brunel University, Uxbridge, Middlesex UB8 3PH, UK
[26]Particle Physics Department, Weizmann Institute of Science, Rehovot 76100, Israel
[27]Universität Hamburg/DESY, II Institut für Experimental Physik, Notkestrasse 85, D-22607 Hamburg, Germany
[28]University of Victoria, Department of Physics, P O Box 3055, Victoria BC V8W 3P6, Canada
[29]University of British Columbia, Department of Physics, Vancouver BC V6T 1Z1, Canada
[30]University of Alberta, Department of Physics, Edmonton AB T6G 2J1, Canada
[31]Duke University, Dept of Physics, Durham, NC 27708-0305, USA
[32]Research Institute for Particle and Nuclear Physics, H-1525 Budapest, P O Box 49, Hungary
[33]Institute of Nuclear Research, H-4001 Debrecen, P O Box 51, Hungary
[34]Ludwigs-Maximilians-Universität München, Sektion Physik, Am Coulombwall 1, D-85748 Garching, Germany

[a] and at TRIUMF, Vancouver, Canada V6T 2A3
[b] and Royal Society University Research Fellow
[c] and Institute of Nuclear Research, Debrecen, Hungary
[d] and Department of Experimental Physics, Lajos Kossuth University, Debrecen, Hungary
[e] and Department of Physics, New York University, NY 1003, USA

The collaboration is also supported by
Department of Energy, USA,
National Science Foundation, USA,
Particle Physics and Astronomy Research Council, UK,
Natural Sciences and Engineering Research Council, Canada,
Israel Science Foundation, administered by the Israel Academy of Science and Humanities,
Minerva Gesellschaft,
Japanese Ministry of Education, Science and Culture (the Monbusho) and a grant under the Monbusho International Science Research Program,
German Israeli Bi-national Science Foundation (GIF),
Bundesministerium für Bildung, Wissenschaft, Forschung und Technologie, Germany,
National Research Council of Canada,
Hungarian Foundation for Scientific Research, OTKA T-016660, and OTKA F-015089.

References

[1] S. L. Glashow, J. Iliopoulos and L. Maiani, Phys. Rev. **D2** (1970) 1285;
S. Weinberg, Phys. Rev. Lett. **19** (1967) 1264;
A. Salam, *Elementary Particle Theory*, ed. N. Svartholm (Almquist and Wiksells, Stockholm, 1968), 367.

[2] P. W. Higgs, Phys. Lett. **12** (1964) 132;
F. Englert and R. Brout, Phys. Rev. Lett. **13** (1964) 321;
G. S. Guralnik, C. R. Hagen, and T. W. B. Kibble, Phys. Rev. Lett. **13** (1964) 585.

[3] CDF Collaboration, F. Abe *et al.*Phys. Rev. Lett **74** (1995) 2626;
D0 Collaboration, S. Abachi *et al.*Phys. Rev. Lett **74** (1995) 2632.

[4] N. Cabibbo, L. Maiani, G. Parisi, and R. Petronzio, Nucl. Phys. **B158** (1979) 295;
M. Lindner, Z. Phys. **C31** (1986) 295;
M. Sher, Phys Rep. **179** (1989) 273;
M. Lindner, M. Sher, and H.W. Zaglauer, Phys. Lett. **228B** (1989) 139.

[5] M. Sher, Phys. Lett. **317B** (1993) 159; addendum *ibid.* **331B** (1994) 448;
C. Ford, D.R.T. Jones, P.W. Stephenson, and M.B. Einhorm, Nucl. Phys. **B395** (1993) 17;
B. Altarelli, and I. Isidori, Phys. Lett. **337B** (1994) 141;
J.A. Casas, J.R. Espinosa, and M. Quiròs, Phys. Lett. **342B** (1995) 171.

[6] *"A combination of Preliminary Electroweak Measurements and Constraints on the Standard Model"* presented in the 28th International Conference on High Energy Physics, Warsaw, Poland, 25-31 July 1996. The LEP Collaborations ALEPH, DELPHI, L3, OPAL, the LEP Electroweak Working Group and the SLD Heavy Flavour Group, CERN-PPE/96-183, Dec.6 1996.

[7] CDF Collaboration, J. Lys, talk presented at ICHEP96, Warsaw, 25-31 July 1996, to appear in the preceedings; D0 Collaboration, S. Protopopescu, talk presented at ICHEP96, Warsaw, 25-31 July 1996, to appear in the preceedings.

[8] ALEPH Collaboration, D. Buskulic *et al.*, Phys. Lett. **B384** (1996) 427;
DELPHI Collaboration, P. Abreu *et al.*, Nucl. Phys. **B421** (1994) 3;
L3 Collaboration, M. Acciarri *et al.*, Phys. Lett. **B385** (1996) 454;
OPAL Collaboration, G. Alexander *et al.*, Z. Phys. **C73** (1997) 189.

[9] A.Djouadi, D.Haidt, B.A. Kniehl, B. Mele, and P.M. Zerwas, Proceedings of *"e^+e^- collisions at 500 GeV: The Physics Potential"*, Munich-Annecy-Hamburg, ed. P.M. Zerwas, DESY-92-123A.

[10] F.A. Berends and R. Kleiss, Nucl. Phys **B260** (1985) 32.

[11] F.A. Berends, W.L. van Neerven, G.J.H. Burgers, Nucl. Phys. **B297**(1988)429, erratum *ibid.* **B304** (1988) 921.

[12] L. Resnick, M.K. Sundaresan, and P.J.S. Watson, Phys. Rev. **D8** (1973) 172:
J. Ellis M.K. Gaillard, and D.V. Nanopoulos, Nucl. Phys. **B106** (1976) 292;
B.L. Ioffe and V.A. Khoze, Sov. J. Part. Nucl. **9** (1978) 50;
B.W. Lee, C. Quigg, and H.B. Thacker, phys Rev. **D16** (1977) 1519;
J.D. Bjorken, Proc. Summer Institute on Perticle Physics, SLAC Report 198 (1976).

[13] E. Braaten and J.P. Leveille, Phys. Rev. **D22** (1980) 715;
N. Sakai, Phys. Rev. **D22** (1980) 2220;
T. Inami and T. Kubota, Nucl. Phys. **B179** (1981) 171;
M. Drees and K. Hikasa, Phys. Lett. **240B** (1990) 455;
S.G. Gorishny, A.L. Kataev, S.A. Larin, and L.R. Surguladze, Mod. Phys. Lett. **A5** (1990) 2703;
A.L. Kataev and V.T. Kim, Mod. Phys. Lett. **A9** (1994) 1309;
L.R. Surguladze, Phys. Lett. **341B** (1994) 61.

[14] H. Geofgi, S.L. Glashow, M.E. Machacek, and D.V. Nanopoulos, Phys. Rev. Lett. **40** (1978) 692.

[15] T. Inami, T. Kubota, and T. Okada, Z. Phys. **C18** (1983) 69;
A. Djouadi, M. Spira, and P.M. Zerwas, Phys. Lett. **264B** (1991) 440.

[16] OPAL Collaboration, K. Ahmet *et al.*, Nucl. Inst. and Meth. **A305** (1991) 275.

[17] "The extended OPAL Silicon Strip Microvertex Detector" S. Anderson *et al.*, CERN-PPE/97-092, submitted to Nucl. Inst. and Meth. A.

[18] M. Arignon *et al.*, Nucl. Inst. and Meth. **A313** (1992) 103.

[19] J. Allison *et al.*, Nucl. Inst. and Meth. **A317** (1992) 47.

[20] R. Brun et al., GEANT3 user's guide, CERN DD/EE/84-1, 1984.

[21] HZHA generator: P. Janot, in *Physics at LEP2*, edited by G. Altarelli, T. Sjöstrand and F. Zwirner, CERN 96-01, vol. 2 (1996), p. 309.

[22] PYTHIA 5.721 and JETSET 7.408 generators: T. Sjöstrand, Comp. Phys. Comm. **82** (1994) 74; T. Sjöstrand, LU TP 95-20.

[23] OPAL Collaboration, G. Alexander *et al.*, Z. Phys. **C69** (1996) 543.

[24] EXCALIBUR generator: F.A. Berends, R. Pittau, R. Kleiss, Comp. Phys. Comm. **85** (1995) 437.

[25] BHWIDE generator: S. Jadach, W. Płaczek, B.F.L. Ward, in *Physics at LEP2*, edited by G. Altarelli, T. Sjöstrand and F. Zwirner, CERN 96-01, vol. 2 (1996), p. 286; UTHEP-95-1001.

[26] KORALZ 4.0 generator: S. Jadach, B. F. L. Ward, Z. Wąs, Comp. Phys. Comm. **79** (1994) 503.

[27] PHOJET 1.05 generator: E. Budinov *et al.*, in *Physics at LEP2*, edited by G. Altarelli, T. Sjöstrand and F. Zwirner, CERN 96-01, vol. 2 (1996) p. 216;
R. Engel and J. Ranft, Phys. Rev. **D54** (1996) 4244.

[28] HERWIG generator: G. Marchesini *et al.*, Comp. Phys. Comm. **67** (1992) 465.

[29] J.A.M. Vermaseren, Nucl. Phys. **B229** (1983) 347.

[30] The grc4f 1.1 generator: J. Fujimoto *et al.*, Comput. Phys. Commun.**100** (1997) 128.

[31] N. Brown and W. J. Stirling, Phys. Lett. **B252** (1990) 657;
S. Bethke, Z. Kunszt, D. Soper and W. J. Stirling, Nucl. Phys. **B370** (1992) 310;
S. Catani *et al.*, Phys. Lett. **B269** (1991) 432;
N. Brown and W. J. Stirling, Z. Phys. **C53** (1992) 629.

[32] OPAL Collaboration, R. Akers *et al.*, Phys. Lett. **B327** (1994) 411.

[33] OPAL Collaboration, P. Acton *et al.*, Z. Phys. **C58** (1993) 523.

[34] MARK II Collaboration, R.G. Jacobsen et al., Phys. Rev. Lett. **67** (1991) 3347.

[35] ALEPH Collaboration, D. Buskulic et al., Phys. Lett. **B313** (1993) 535.

[36] ALEPH Collaboration, D. Buskulic et al., Phys. Lett. **B401**(1997)163.

[37] OPAL Collaboration, R. Akers *et al.*, Z. Phys. **C65** (1995) 17.

[38] OPAL Collaboration, R. Akers *et al.*, Z. Phys. **C66** (1995) 19.

[39] OPAL Collaboration, G. Alexander *et al.*, Z. Phys. **C52** (1991) 175.

[40] G. Parisi, Phys. Lett. **B74** (1978) 65;
J. F. Donoghue, F. E. Low and S. Y. Pi, Phys. Rev. **D20** (1979) 2759.

[41] OPAL Collaboration, G. Alexander *et al.*, Z. Phys. **C70** (1996) 357.

[42] OPAL Collaboration, R. Akers *et al.*, Z. Phys **C63** (1994) 197.

[43] P. Bock, *"Determination of exclusion limits for particle production using different decay channels with different efficiencies, mass resolutions and backgrounds"*, Heidelberg University preprint HD-PY-96/05 (1996).

[44] E. Gross, B. A. Kniehl, and G. Wolf, Z. Phys. **C63** (1994) 417; erratum *ibid.* **C66** (1995) 32.

[45] A. Djouadi, M. Spira, and P. M. Zerwas, Z. Phys. **C70** (1996) 425.

[46] R. D. Cousins, V. L. Highland, Nucl. Inst. and Meth. **A320** (1992) 331.

[47] *"Search for the S.M. Higgs boson at LEP"* presented at the International Europhysics Conference on High Energy Physics, 19-26 Aug. 1997, Jerusalem, Israel.